LUMINESCENCE DARKENING OF STRAIN-TRAPPED EXCITONS IN COUPLED QUANTUM WELLS

by

Nicholas W. Sinclair

B.S. Physics, University of Texas, 2005

Submitted to the Graduate Faculty of

the Kenneth P. Dietrich School of Arts and Sciences in partial fulfillment

of the requirements for the degree of

Doctor of Philosophy

University of Pittsburgh

2014

UNIVERSITY OF PITTSBURGH

DIETRICH SCHOOL OF ARTS AND SCIENCES

This dissertation was presented

by

Nicholas W. Sinclair

It was defended on

April 16, 2014

and approved by

Dr. David Snoke, Dept. of Physics and Astronomy

Dr. Kevin Chen, Dept. of Electrical and Computer Engineering

Dr. Robert Coalson, Dept. of Chemisty and Dept. of Physics and Astronomy

Dr. Robert P. Devaty, Dept. of Physics and Astronomy

Dr. Jeremy Levy, Dept. of Physics and Astronomy

Dissertation Director: Dr. David Snoke, Dept. of Physics and Astronomy

LUMINESCENCE DARKENING OF STRAIN-TRAPPED EXCITONS IN COUPLED QUANTUM WELLS

Nicholas W. Sinclair, PhD

University of Pittsburgh, 2014

Interwell excitons in coupled quantum wells are a promising systems for achieving an excitonic Bose-Einstein condensate, as the extremely long lifetime of these excitations allow large populations to accumulate and thermal equilibration of the gas. Such a condensate would be notable for the constituent particles having strong, long-range, repulsive interactions, a property that also makes the condensate formation more difficult by suppressing wavefunction overlap. It is believed, however, that with suitable traps the bosonic nature of this excitation will prevail and a condensate will form. Within GaAs/AlGaAs coupled quantum wells, large-scale strain traps have been employed to confine excitons, and a transition is observed in the spatial structure of the exciton photoluminescence under conditions of high strain, low temperature, and high density. Under these conditions, the luminescence at the center of the trap, where the density remains largest, becomes dim compared to the rest of the trap region. This document presents evidence of this transition and explores the nature of the darkening by examining the exciton luminescence, resolved spatially, spectroscopically, and temporally. Several possible mechanisms for this behavior are discussed, in particular that of Bose-Einstein condensation, formation of an electron-hole liquid, and strain-induced valence-band mixing. However, none of these mechanisms adequately account for all of the behavior associated with the darkening. The valence-band mixing argument receives particular attention, as it presents the most testable predictions, in addition to offering an explanation for the darkening relying solely on the single-particle spectrum.

TABLE OF CONTENTS

LIST OF FIGURES

1.0 INTRODUCTION: INDIRECT EXCITONS AND BOSE-EINSTEIN CONDENSATION

The research environment giving rise to this dissertation is one pursuing Bose-Einstein Condensation (BEC) of excitons in semiconductors, and the work herein is a continuation of the work of others aimed at achieving BEC in pairs of GaAs quantum wells (coupled quantum wells). This work picks up at a particularly promising point in experimentation, where the system has been shown to have extremely long-lived states, and thermal and spatial equilibration at low temperature with a particular trapping mechanism has been experimentally verified. With previous work showing no obvious signs of BEC, the situation at the start of my tenure seemed to simply require ratcheting up the experimental parameters and confirming the existence or lack of appearance of an exciton BEC. The result of this process, perhaps predictably, was not so clear cut. Instead of the typical BEC signals that one might expect, a vastly different phenomenon was observed, the sudden darkening of the photoluminescence from the high-density population of trapped particles. The aim of this document is to explore the nature of this darkening procedure, particularly in the light of whether or not BEC is playing any role.

The expectation of BEC from this experimental system is not without reason. This transition is expected to occur in the "indirect exciton"[1], or IX, state that straddles the high-bandgap barrier between two quantum wells. IX states are composed of an electron and a hole in opposing wells that remain bound together at low temperature, and, as such, they have a very long lifetime for recombination. With a suitable trapping mechanism to confine these particles, relatively high exciton densities may be reached, and the criteria for BEC are

[1]One might call this state "spatially-indirect", in contrast to more commonly discussed momentum-indirect electronic transtions, or "interwell".

potentially within reach of relatively simple experiments at temperatures in the vicinity of a few degrees Kelvin, in contrast to the complexity and expense of atomic BEC experiments. Further simplifying the experimental design, the exciton BEC system has a built-in probe in the exciton's ability to directly annihilate, by electron-hole recombination, to create a single photon. Because this annihilation is direct, requiring no phonons, for example, the photoluminescence (PL) from these recombination events represent not only the density of the excitons but also exciton energy and complex phase. The experiments detailed in this document universally exploit this convenient probe by measuring the intensity, energy spectrum, polarization, and coherence of exciton recombination PL.

In the last decade, there has been substantial evidence for BEC of microcavity exciton-polaritons [9, 77, 37], that can claim even more favorable critical onset parameters due to the extraordinarily small mass of the polaritons. Despite not winning the prize for the first (non-Cooper pair) condensate of excitations in a solid, the IX BEC still has many desirable features that cannot be claimed by polariton condensates. Specifically, IXs live much longer than the time required to exchange energy with the lattice via phonons, allowing the population to reach a well-defined, thermal quasi-equilibrium (with the lowest state being the lowest-lying exciton state, rather than an empty conduction-band), and they possess a strong, long-range interparticle repulsion that far surpasses the interactions among polaritons. This repulsion has the added benefit of supressing the formation of indirect exciton molecules (e.g. biexcitons) or an indirect electron-hole liquid (EHL) state, which are significant barriers to creating BECs in high density systems [41]. Polariton systems are inching closer to a resolution of the equilibration problem by pushing the limits of cavity Q-factors, but the strength and long-range nature of the interactions in the IX system are not achievable with polaritons[2].

The typical conception of BEC is that of a non-interacting gas, and adding interactions between the particles naively seems to upset the picture. However, from the theory of weakly interacting, dilute gas BEC, in which one can treat the interparticle interactions as a small

[2]Although, because of the possibility of bound biexciton states in the polariton system, it is feasible to exploit a Feshbach resonance, similar to work in atomic BEC, to tune the exciton-exciton interaction strength, which is the dominant polariton-polariton scattering mechanism. [25]. To date, this has not been demonstrated experimentally.

perturbation, as outlined in Section 1.6.1, the interactions actually stabilize the BEC against fragmentation, in addition to allowing for a non-zero superfluid velocity. From the case of liquid Helium, LHe, a strongly interacting system for which the perturbation technique is not appropriate [22], we learn that many of the qualitative concepts associated with the weakly-interacting case carry over to the case of strong interactions, i.e. the condensate is strongly depleted but still remains with a finite ground-state occupation and a superfluid state remains. However, many details are vastly different. For example, the superfluid transition temperature actually decreases with density due to the strong repulsion, the opposite trend to the weakly-interacting case. The well-studied LHe case does not necessarily map out our expectations for a BEC of indirect excitons, though. One important difference is that IXs lack the weakly attractive part of the LHe interaction responsible for the low-temperature collapse into a liquid state[3]. Thus, the precise form of the IX BEC remains somewhat of a mystery.

While the interaction strength is perhaps the most unique feature of the IX system, it also presents the largest hurdle to achieving a BEC. The repulsion causes a blue shift of the energy of the trapped population with increasing density, creating an effective limit on the achievable density in a finite depth energetic trap. At some density, the excitons are blue-shifted out of the trapping potential, and one must increase the trap depth in order to further increase the density. Previous research in our group has looked for BEC signals from populations in relatively shallow traps (and, therefore, at low density), using a technique of creating a localized strain to trap excitons. Having demonstrated no evident transitions in the trapped population, this dissertation picks up at the point of increasing the applied stress to create much deeper traps, whereupon a pronounced darkening of the total photoluminescence from the center of the trap is observed. This pattern is displayed in Figure 1, showing intensity images of the IX luminescence with increasing force applied to the sample.

Due to the lack of any similar phenomena among studies with different trapping mech-

[3]An attractive interaction is possible between IXs in the case of very thin well separations, where the Van der Waals in-plane polarization of the exciton is able to make a significant contribution to the potential energy. However, in the present systems, the well separations are always above that required to forbid an attractive interaction at any distance. See Section 1.4.2

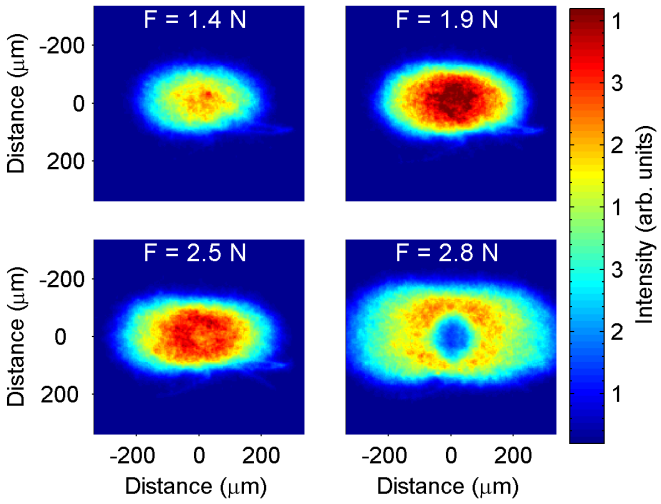

Figure 1: Images with increasing force applied to the sample, showing darkening of indirect exciton luminescence at trap center. A localized force is applied to the sample to create a strain-based trap for indirect excitons. With increasing trap depth, the trap-center luminescence dims, rather than becoming brighter with increasing exciton density.

anisms, in attempting to explain this behavior, the most suspicion falls naturally on the strain trapping technique as the root cause, and a convincing case is made for the existence of a darkening mechanism resulting from strain-induced mixing of valence-band states. However, in theoretical discussions of excitonic BEC, much attention has been paid to the role of "dark" (total angular momentum $J = 2$) excitons [17] (which should be the true ground state of the system, due to exchange interactions), and some recent theoretical works [45, 36] have discounted our valence-band mixing explanation and explained the results of our darkening phenomena (and linear polarization profiles) by invoking condensates that are a mixture of bright and dark excitons. Admittedly, the mixing argument on its own is far from explaining all of the behavior in this system. For this reason and also simply due to the context of this work, a good deal of discussion is devoted to the possible role of condensation in causing all or parts of this phenomenon.

In addition, we will briefly consider the possibility of an interwell EHL causing the darkening in this system. It may be the case that, despite the IXs having an overall repulsion,

an ionized interwell plasma might have an overall attractive interaction, making an interwell EHL possible in the ionized case. This could explain the dimming of the luminescence, since an ionized state has reduced electron-hole correlation. In addition, it offers another explanation for the disappearance of the effect at elevated temperature, as the liquid transitions back to an excitonic gas.

This dissertation will present the darkening effect, explore possible explanations, and attempt to glean any useful information from these explanations, including, perhaps most importantly, the best direction to move forward with the strain-trapping technique for IXs. This introductory chapter will cover the essential characteristics of excitons in coupled quantum wells as well as the predicted role of Bose-Einstein condensation in this system. Chapter 2 will briefly review the interaction of IXs with strain and magnetic field and discuss the processes of excitation and luminescence. Experimental apparatus and procedures are detailed in Chapter 3, and Chapter 4 relates the results of specific experiments. Chapter 5 concludes the document with a discussion of these experimental results in the light of a few possible mechanisms for the darkening and the context of other recent experimental works by others.

1.1 BULK EXCITONS

Semiconductor crystals are characterized by the existence of an energetic gap between the highest filled electronic energy band (valence-band, VB) and lowest unoccupied band (conduction-band, CB). Excitation of an electron from the valence-band to the higher energy conduction-band not only puts an electron in this unfilled band where it may move in response to external forces, it also leaves behind an empty state in the valence-band, referred to as a hole. The electrons remaining in the valence-band collectively act in the presence of the single empty state as if there were only a single, positively charged particle moving in the valence-band. By this substitution, we see that electronic excitation creates two quasiparticles in a semiconductor, the electron and hole, that will feel an attractive interaction to each other. Just as in atomic hydrogen or positronium, there is a characteristic binding energy corresponding to the Coulomb interaction, and, at correspondingly low temperatures, the

electron-hole, e-h, pairs will remain bound together as an electrically neutral particle called an exciton.

The energy of a free exciton is given simply by [31]:

$$E_x = E_g + E_k - E_b,$$

where E_g is the band gap energy, E_k is the kinetic energy of the center of mass of the bound e-h pair, and E_b is the Coulombic binding energy. One can write the kinetic term as

$$E_k = \frac{\hbar^2 k^2}{2(m_e + m_h)}, \tag{1.1}$$

in the effective-mass approximation, where m_e and m_h are the effective masses of the electron and hole[4]. The binding energy, as stated above, is exactly analogous to hydrogen,

$$E_B = \frac{\mu_{ex} e^4}{8h^2 \epsilon_{GaAs}^2},$$

where μ_{ex} is the reduced mass of the pair and ϵ_{GaAs} is the permittivity in GaAs. Just as in hydrogen, we may also characterize the size of the exciton with the Bohr radius,

$$a_B = \frac{4\pi\hbar^2 \epsilon_{GaAs}}{\mu_{ex} e^2}.$$

In GaAs, the static dielectric constant is 12.7 [64] near 0 Kelvin and the exciton reduced mass is $0.059\mathrm{m}_0$[5], where m_0 is the electron mass in vacuum, yielding an approximate binding energy of 5.0 meV and a Bohr radius of 11.4 nm. This binding energy corresponds to temperature of 58 Kelvin, suggesting that in experiments with samples immersed in liquid helium (LHe), the excitons will easily remain bound. The large size of this exciton in comparison with the GaAs lattice spacing of 0.56 nm puts these excitons in the category of the Wannier-Mott type and justifies our use of the effective mass approximation. The very small m_e responsible for this

[4]In general, these effective masses are not isotropic, and, outside of sketched outlines such as this, one must account for this tensorial nature. For our purposes later, we will treat the effective mass tensor as diagonal in the basis of one direction along the growth direction and two degenerate directions along the quantum well plane, such that one may make simple, separate computations as in Eq (1.1) for momentum components along each direction.

[5]Here $0.067m_0$ is used for for m_e and a directionally-averaged valence-band mass, $0.5\mathrm{m}_0$ [15], is used for m_{hh}.

large exciton wavefunction is due to the relatively large coupling between the $|S\rangle$ conduction-band states and $|P,m=0\rangle$ states at non-zero crystal momentum, k. This interaction causes level repulsion between the conduction-band and the light-hole band (which will be discussed in the next section), lowering the mass of quasiparticles in each of these bands. The heavy-hole band consists of the VB states, $|P,m=\pm1\rangle$, and does not mix with the CB through this mechanism, thus remaining "heavy".

None of these excitons will exist in perfect equilibrium in our experiments. The GaAs bandgap is roughly 1.5 eV at 2 K, so that thermal fluctuations are many orders of magnitude from spontaneously generating conduction-band electrons. Therefore, we must artificially create exciton populations either by injecting carriers electronically or by direct optical excitation. This experiment exclusively employs optical excitation (in undoped wells), illuminating the sample with light at sufficient energy to excite a VB electron into the CB or, in the case of resonant exciton creation, with an energy below the bandgap by the excitonic Rydberg energy.

1.1.1 Valence Band Structure

In order to introduce the exciton concept, the discussion has proceeded as if there were only a single possible valence and conduction-band. Doing so neglects the complicated VB structure of GaAs which forms the basis of much of the discussion in this dissertation. An approximate calculation of the bulk dispersion relations for the band edge states in bulk is displayed in Figure 2, calculated with the Luttinger-Kohn Hamiltonian as explained below. As shown, the CB remains simple. Composed of s-like orbital electron states, electrons in this band carry only spin angular momentum, and the band is correspondingly 2-fold degenerate. The VB, though, is composed of extended p-orbital states with orbital angular momentum quantum number $\ell = 1$, in addition to the electrons spin angular momentum. The addition of these components yields hole states with total angular momentum quantum number $j = \frac{3}{2}$ or $\frac{1}{2}$, which would be degenerate in a bulk crystal without spin-orbit coupling.

The spin-orbit coupling in bulk GaAs is substantial and splits these states according to

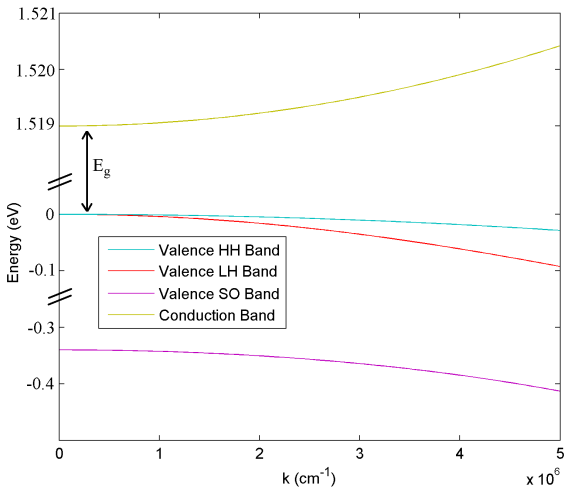

Figure 2: Estimated bulk dispersion relations of GaAs band edges. The structure of the band edges are displayed for bulk GaAs, for momenta along [100], calculated using the Luttinger-Kohn Hamiltonian. The SO (split-off) band is split from the band edge by the spin-orbit interaction, by 0.34 eV [15]. The differing masses of the band edge states, HH = $|j, j_z\rangle$, $|\frac{3}{2}, \pm\frac{3}{2}\rangle$ and LH = $|\frac{3}{2}, \pm\frac{1}{2}\rangle$, are apparent.

j. This splitting is easy to explain qualitatively. With the perturbation Hamiltonian of the form $+\vec{L}\cdot\vec{S}$, this shift produces higher energy states to the extent that the spin and orbital angular momentum are aligned. Thus, the larger total angular momentum states are shifted to higher energy. The lower energy state, $j = \frac{1}{2}$, is referred to as the split-off band, as it is often neglected due to its energetic separation from the VB edge, now composed of $j = \frac{3}{2}$ holes. This separation is approximately 0.34 eV in bulk GaAs [15]. These states are 4-fold degenerate at the Γ-point and consist of the states, labeled by $|j, j_z\rangle$, $|\frac{3}{2}, \pm\frac{3}{2}\rangle$ and $|\frac{3}{2}, \pm\frac{1}{2}\rangle$.

As mentioned previously, the effective masses are different for these VB states, with the label heavy-hole (HH) given to the $|\frac{3}{2}, \pm\frac{3}{2}\rangle$ states and Light-Hole (LH) given to $|\frac{3}{2}, \pm\frac{1}{2}\rangle$. The difference of these effective mass values from the bare electron mass derives from interband mixing. The effect of this mixing is taken into account by the Luttinger-Kohn Hamiltonian,

which we will express in matrix form, following Chuang [15],

$$H_{L-K} = -\begin{pmatrix} P+Q & -S & R & 0 \\ -S^\dagger & P-Q & 0 & R \\ R^\dagger & 0 & P-Q & S \\ 0 & R^\dagger & S^\dagger & P+Q \end{pmatrix}. \tag{1.2}$$

This is in the basis of $|\frac{3}{2},\frac{3}{2}\rangle$, $|\frac{3}{2},\frac{1}{2}\rangle$, $|\frac{3}{2},-\frac{1}{2}\rangle$, $|\frac{3}{2},-\frac{3}{2}\rangle$, where these states are defined in terms of the p-state wavefunctions that compose the topmost filled shell of the Ga and As atoms[6] [15],

$$|\frac{3}{2},\frac{3}{2}\rangle \equiv \frac{1}{\sqrt{2}}|(X-iY)\downarrow\rangle, \tag{1.3a}$$

$$|\frac{3}{2},-\frac{3}{2}\rangle \equiv -\frac{1}{\sqrt{2}}|(X+iY)\uparrow\rangle, \tag{1.3b}$$

$$|\frac{3}{2},\frac{1}{2}\rangle \equiv \frac{1}{\sqrt{6}}|(X-iY)\uparrow\rangle + \sqrt{\frac{2}{3}}|Z\downarrow\rangle, \tag{1.3c}$$

$$|\frac{3}{2},-\frac{1}{2}\rangle \equiv -\frac{1}{\sqrt{6}}|(X+iY)\downarrow\rangle + \sqrt{\frac{2}{3}}|Z\uparrow\rangle. \tag{1.3d}$$

For completeness, the split-off states are:

$$|\frac{1}{2},\frac{1}{2}\rangle \equiv \frac{1}{\sqrt{3}}|(X-iY)\uparrow\rangle - \frac{1}{\sqrt{3}}|Z\downarrow\rangle,$$
$$|\frac{1}{2},-\frac{1}{2}\rangle \equiv \frac{1}{\sqrt{3}}|(X+iY)\downarrow\rangle + \frac{1}{\sqrt{3}}|Z\uparrow\rangle.$$

The definitions take this particular form because the effect of the spin-orbin interaction between the conduction-band and valence-band has already been taken into account. These are the eigenvectors resulting from that interaction. In leaving out the $j{=}\frac{1}{2}$ states from the basis of the Luttinger-Kohn Hamiltonian, we have neglected the effect of the split-off band

[6]The apparent contradiction between the angular momenta of the states on the LHS and RHS of these equations is due to the labeling scheme I have chosen. I have chosen to label the hole states by the angular momentum they carry rather than the angular momentum of the vacant electrons. This is explained further on in this section. If the alternate scheme is preferred, flipping the signs on the LHS will accomplish this.

on these band edge states. The parameters in the matrix 1.2 are momentum dependent, given by,

$$P = \frac{\hbar^2\gamma_1}{2m_0}(k_x^2 + k_y^2 + k_z^2), \tag{1.4a}$$

$$Q = \frac{\hbar^2\gamma_2}{2m_0}(k_x^2 + k_y^2 - 2k_z^2), \tag{1.4b}$$

$$R = \frac{\hbar^2}{2m_0}(-\sqrt{3}\gamma_2(k_x^2 - k_y^2) + 2i\sqrt{3}\gamma_3 k_x k_y), \tag{1.4c}$$

$$S = \frac{\sqrt{3}\hbar^2\gamma_3}{m_0}k_z(k_x - ik_y). \tag{1.4d}$$

The γ_n are given by off-diagonal matrix elements coupling the bands and are established by experiment.

The eigenvalues for Eq (1.2) are given by:

$$E(k) = -P \pm \sqrt{|Q|^2 + |R|^2 + |S|^2},$$

with the negative (positive) sign corresponding to the HH (LH) energy. From this, we can see a direction dependence of the effective mass. If we take k along the $\hat{z}$, [001], direction, we have

$$E(k{=}k_z) = -\frac{\hbar^2}{2m_0}(\gamma_1 \pm 2\gamma_2)k_z^2 \tag{1.5}$$

where, again, positive corresponds to the LH. In any direction perpendicular to this plane,

$$E(|k|{=}\sqrt{k_x^2 + k_y^2}) = \frac{\hbar^2}{2m_0}(\gamma_1 \mp \gamma_2)(k_x^2 + k_y^2), \tag{1.6}$$

with the same sign convention. Thus, the effective masses may be read off and values for gamma inserted,

$$m_{HHz} = -\frac{m_0}{(\gamma_1 - 2\gamma_2)} = -0.33m_0 \tag{1.7a}$$

$$m_{LHz} = -\frac{m_0}{(\gamma_1 + 2\gamma_2)} = -0.094m_0 \tag{1.7b}$$

$$m_{HH\perp} = -\frac{m_0}{(\gamma_1 + \gamma_2)} = -0.12m_0 \tag{1.7c}$$

$$m_{LH\perp} = -\frac{m_0}{(\gamma_1 - \gamma_2)} = -0.20m_0. \tag{1.7d}$$

We see immediately the the labels attached to these states are somewhat misleading. While the LH state is indeed lighter in the [001] direction (this is the growth direction in our case), it is heavier than the HH state for motion in the plane perpendicular to [001]. It should be noted that both of these masses are negative, as demonstrated in Figure 2, so that an electron at the center of the Brillouin zone has the highest energy, and, consequently, it represents the lowest energy for holes. The main importance of the LH and HH masses for this work is their role in determining the size of exciton states and tunneling probability. Excitons composed of lower mass particles will tend to be spread over a larger area, due to the higher energy cost of high momentum components, and, for the same reason, lower mass particles have a larger tunneling probability due to the slower decay of their wavefunction[7].

The conduction-band effective mass may be calculated in a similar way by considering the spin-orbit interaction between the valence-band and conduction-band. As mentioned above, the solution to this calculation was already incorporated into the choice of valence-band basis for the Luttinger-Kohn Hamiltonian, and the calculation will not be reproduced here. The result is an effective conduction-band mass of $0.067m_0$.

Thus, the lowest energy electronic excitation from a bulk crystal of GaAs is that of a single exciton, composed of a hole with $j_h = \frac{3}{2}$ (LH and HH are degenerate at zone center) and a conduction-band electron with $j_e = \frac{1}{2}$. The total angular momentum of these excitons is determined by the relative alignment of their electron and hole spins.

However, in order to compare electron and hole spin alignment, we must establish what is meant by a positive angular momentum of a hole. We may either label the hole angular momentum as that of the vacant electron state or as that carried by the VB due to the vacancy. The latter case represents the angular momentum actually existing in the system. Specifically, if we describe a full VB and an empty conduction-band as $|0\rangle$, a fictional excitation that would create a vacancy in an electron state with $j_z = +\frac{3}{2}$ would look like, $\hat{a}_{j_z=3/2}|0\rangle$, where $\hat{a}(\hat{a}^\dagger)$ will be our electron destruction(creation) operators, and we will neglect where the electron actually goes. We might label this state by $j_z = \frac{3}{2}$, representing the missing electron state, or $j_z = -\frac{3}{2}$ representing the collective angular momentum of

[7]Again, note that the lower mass, more delocalized, particle in-plane will be the heavy hole exciton, and, in the growth direction, it is the LH exciton.

the VB. This document will take the latter convention, as it has the advantage that when creating an exciton by destroying a photon, the addition of the constituent electron and hole angular momenta will directly add up to that of the photon, e.g. a photon with left circular polarization, $j_z = -1$, might create a $j_z = -\frac{3}{2}$ hole and a $j_z = +\frac{1}{2}$ electron.

Because the Coulomb interaction does not change the spin of the electron, the electron states with differing spin are not mixed by the electron-hole attraction. The exciton above, with a $j_z = -\frac{3}{2}$ hole and a $j_z = +\frac{1}{2}$ electron, is optically allowed by this interaction, because the hole represents a vacancy with spin up, and no electron spin-flip is required. However, that same hole paired with a spin down electron would be forbidden to recombine. Excitons, of that type, with $j = 2$, $j_z = \pm 2$ are referred to here as "dark" excitons. While there are many other types of excitons which are optically forbidden, we will reserve dark exciton to refer to this specific case, and we will refer to the $j = 1$, $j_z = \pm 1$ excitons as "bright" in contrast.

Bright and dark excitons are not degenerate; they are split in energy by electron-hole exchange. The sign of this term and thus the energetic ordering of the states is easily explained. This exchange interaction is the correction to the e-h Coulomb interaction, accounting for the anticorrelation of spin-aligned electrons. This spatial anticorrelation reduces the magnitude of the attractive e-h interaction, yielding a blue-shift in the spin-aligned case[8], the bright exciton. This interaction is of the form [10]:

$$\Delta E^{ex}_{e-h} = \iint V(|\vec{r}_1 - \vec{r}_2|)\Psi^*_c(\vec{r}_1)\Psi^*_v(\vec{r}_2)\Psi_v(\vec{r}_1)\Psi_c(\vec{r}_2)d^3r_1 d^3r_2, \tag{1.8}$$

so it is very sensitive to the overlap of the electron-hole wavefunction.

For clarity, the exciton's total angular momentum expressed here comes exclusively from the angular momentum of the constituent electron and hole with respect to the lattice nuclei and to the intrinsic electron spins. That is to say, we have only considered the angular

[8]This refers to alignment of the electron state in the CB and vacant electron state in the VB. If one finds the 'hole' abstraction to muddle this discussion, the sign of this interaction can be explained completely in terms of electrons. If one first imagines the interaction energy of a conduction electron with a full VB, the exchange correction causes the repulsive Coulomb interaction between spin-aligned electrons to be lower than that between opposite spins. Removing an electron (creating a hole) will reduce this repulsion and blue shift. The spin correction means that removing a spin-aligned electron from the VB yields a smaller decrease in potential energy, and the spin-aligned pair (i.e. ↑ CB electron and vacant ↑ VB electron) must, therefore, have a higher energy.

momentum from the very small spatial scale (contained within the periodic unit-cell functions of each of the electron bands), and have neglected the relative orbital angular momentum of the electron and hole in an exciton, occurring on the larger scale of the Bohr radius. In order to limit the complexity of the forthcoming discussion, we will limit the exciton states to be s-like in terms of the electron-hole relative motion.

1.2 EXCITONS IN A SINGLE QUANTUM WELL

In a planar quantum well structure, composed of a thin layer of low bandgap material surrounded by regions of larger band gap, such as GaAs layers surrounded by AlAs or AlGaAs, an exciton will have lower energy in the interior region, with an energetic barrier of roughly the bandgap difference between the interior and exterior regions. Confining the carriers into a single plane will fundamentally alter the spectrum of exciton states. The forced shift to a very large k_z is responsible for a large blue shift which splits the LH/HH degeneracy due to their differing masses in the growth direction. If the growth direction is [001], as in our wells, the LH will have a lighter mass in the confinement direction, causing the HH state to be the lowest energy state.

We can make some rough calculations in order to predict the spectral characteristics of the photoluminescence. The quantum wells in these experiments have varying widths, but are typically around 12 nm. They are composed of GaAs/$Ga_{1-x}Al_xAs$, with x from 0.447 to 0.458, varying only slightly between samples[9]. At T = 2 K, we can calculate the bandgap of the GaAs and GaAlAs to be 1.521 eV and 1.842 eV [55], respectively, giving a barrier height of 321 meV. Making a rough estimate of the valence-band offset to be $\frac{1}{3}$ of the bandgap [46] yields a conduction-band barrier of 214 meV and 107 meV for the valence-band. We may

[9]This Al fraction should make the barrier transition indirect (Al X_c to Al Γ_v). The direct to indirect transition occurs at x=0.43 [42]. In some studies, the energy of the Al X-valley actually becomes lower than the Ga Γ-point energy, so conduction electrons prefer to reside in the "barrier", creating Type-II excitons. This is not the case in this experiment. Though we will be dealing with what some may refer to as Type-II excitons in these coupled wells, these will exist with carriers exclusively within the wells (one carrier in each). In our case, the Ga Γ_c point remains lower in energy than any state in the Al barrier. This would not be the case, however, if we applied extremely large stresses [40] or had very narrow GaAs wells (1-2 ML for our Al fraction) [20].

consider the confinement energies of each of the excitonic constituents individually, ΔE^{e}_{conf} and $\Delta \mathrm{E}^{HH}_{conf}(\Delta \mathrm{E}^{LH_{conf}})$, so that we may account for the individual masses. For a finite barrier, with well width w = 12 nm, we can numerically calculate (including the differing mass in barrier/well), $\Delta \mathrm{E}^{e}_{conf}$ = 22 meV, $\Delta \mathrm{E}^{HH}_{conf}$ = 5 meV, $\Delta \mathrm{E}^{LH}_{conf}$ = 15 meV. The binding energy of a quantum well exciton is increased from that of bulk due to the confinement. These have been calculated numerically in GaAs/$\mathrm{Ga}_{1-x}\mathrm{Al}_x\mathrm{As}$ wells with x = 0.4 by Andreani et al. [6] to be E^{HH}_{b} = 9.3 meV and E^{LH}_{b} = 11.5 meV.

With these shifts accounted for, we predict the energy of the excitons in a single well to be, roughly: E^{HH} =1.539 eV and E^{LH}= 1.5465 eV, giving a splitting of about 7.5 meV. These energies are rather sensitive to the valence-band offset, with a LH/HH exciton splitting of 8.1 meV for offset $\Delta \mathrm{E}_v = 0.2\mathrm{E}_g$ and 5.9 eV for Δ $\mathrm{E}_v = 0.4\mathrm{E}_g$. With an energy splitting in this range, it is clear that at 2 K, almost no LH excitons will be thermally excited. Also, we will undoubtedly only be looking at n = 1 excitations of the quantum well. In some experiments, parity-forbidden transitions (such as the transition between an electron in the lowest (symmetric) quantum well state and the first excited (antisymmetric) HH state) are referred to as "dark". We need not worry about these transitions due to the energy scale, and so we continue to reserve dark for J = 2 excitons[10].

The bright/dark exciton splitting for direct excitons will be tiny compared to these energy scales and will have no bearing on our energy measurements. This splitting has been theoretically predicted to be tens of μeV for well-widths similar to our experiments [44], and it has been experimentally measured to be 40 μeV in 15 nm wide wells [73].

1.3 INDIRECT EXCITONS AND THE QUANTUM-CONFINED STARK EFFECT

With two quantum wells, separated by a thin barrier, we expect the states in these wells to be coupled. Let us first consider the case of flat bands. In the absence of an electric

[10]In addition, these transitions will no longer be strictly forbidden due to the symmetry-breaking offered by the growth-direction electric field [14, 43].

field across this structure, we know that the single-particle solutions to this potential will be symmetric and antisymmetric combinations of the individual well states, with the symmetric combination slightly lower in energy. Now, additionally considering the Coulomb interaction between electrons and holes, there will be a binding energy advantage to have an intrawell exciton rather than a combination of purely symmetric states, but this comes at a cost of mixing the symmetric and antisymmetric single-particle states. Therefore, we can consider two regimes, distinguished by the relative strength of the symmetric–antisymmetric (SA) splitting and the binding energy advantage for an intrawell exciton [11]. When the SA splitting is relatively small, as with wide-barrier CQWs, the interaction causes the ground state configuration to consist of electrons and holes in the same quantum well with a relatively large binding energy. If we temporarily adopt the notation that $\Phi_1^e(\Phi_2^h)$ represents a state with an electron (hole) in well '1'('2'), the ground state of the wide-barrier coupled quantum well would be well described by strongly-correlated electron and hole well-occupancy: $\Phi_1^e\Phi_1^h+\Phi_2^e\Phi_2^h$. This is the case when the intrawell exciton description makes sense. In the case of a narrow barrier, when the SA splitting is large, the electron and hole positions should be very close to those predicted by the single-particle Hamiltonian. Specifically, it would be very nearly a product state of the individual symmetric states, $(\Phi_1^e + \Phi_2^e)(\Phi_1^h + \Phi_2^h)$. In this case, there are still excitonic effects, corresponding to the electron-hole motion in the QW plane, but the growth direction positions are not very affected by the Coulomb interaction and the intrawell label should not apply.

In our system with a 4 nm GaAs/$Ga_{1-x}Al_xAs$ barrier and 14 nm wells, we are in the regime where the binding energy dominates. The SA splitting decreases with barrier height and barrier thickness. Bayer et al. [11] showed that with a pure AlAs barrier, only about 8 monolayers were required for the SA splitting of the HH transition to be less than 1 meV. While the barrier height in this case is about twice that of our barriers, the roughly 16 ML thick barriers in the present case puts it well into the regime of dominating binding energy. Thus, we conclude that the flat-band ground state excitons are not composed of symmetric single-particle wavefunctions but composed of intrawell excitons.

Introducing an electric field will polarize the excitons and cause a red shift to the extent that the electron and hole may be separated in this structure. This is called the quantum-

confined stark effect (QCSE) due to the limited degree to which the carriers may move due to confinement. At near zero electric field, the intrawell excitons remain the ground state. The binding energy advantage (or SA splitting in the case of a very narrow barrier) of an intrawell exciton are competing with the small polarizability of the intrawell state. At higher field, the ground state will transition to consist of an electron in the well nearest the positive electric potential and a hole in the opposite well. If we consider the dipole moment of this polarized, IX, state as fixed due to the well separation, there should be a nearly linear shift of:

$$\Delta E_{QCSE} = -eE_z d, \tag{1.9}$$

where the distance d is roughly the well width plus the barrier thickness, representing the mean electron-hole separation. At increasing field, in this regime, the wavefunctions within each well move slowly to the exterior, slightly increasing the electron-hole separation, despite the increased kinetic energy cost to do this, making the shift very slightly superlinear. While this shift may be increased indefinitely, it has a practical limit due to our desire to retain the exciton states in the wells. As the bands become increasingly tilted, tunneling into the exterior barrier becomes more likely, especially in the lower mass conduction-band.

The shift of the LH and HH IX states should be very similar, though there should be some small difference due to their differing masses. The lighter mass of the LH in the confinement direction allows more penetration of the LH into the barrier regions. This allows the LH to be slightly closer to its paired electron, reducing the dipole moment and Stark shift. The DX case is similar, but excludes the shift to a large, nearly constant dipole moment. Due to this, the DX red shift will remain approximately quadratic in E_z and will be much smaller than that of the IX.

Figure 3 shows a numerical simulation of the IX Stark shift for 14 nm wide wells and a 4 nm barrier (replicating our system), including the electron-hole Coulomb interaction. This simulation was performed by M. Szymanska[11], while working in collaboration with our group in order to explain our PL Darkening. It treats the single-particle potential and Coulomb interaction on an equal footing, and exactly diagonalizes the two-particle problem within a finite basis set of one-particle wave functions. This simulation allows a prediction of the

[11]Marzena Szymanska, Department of Physics, University of Warwick

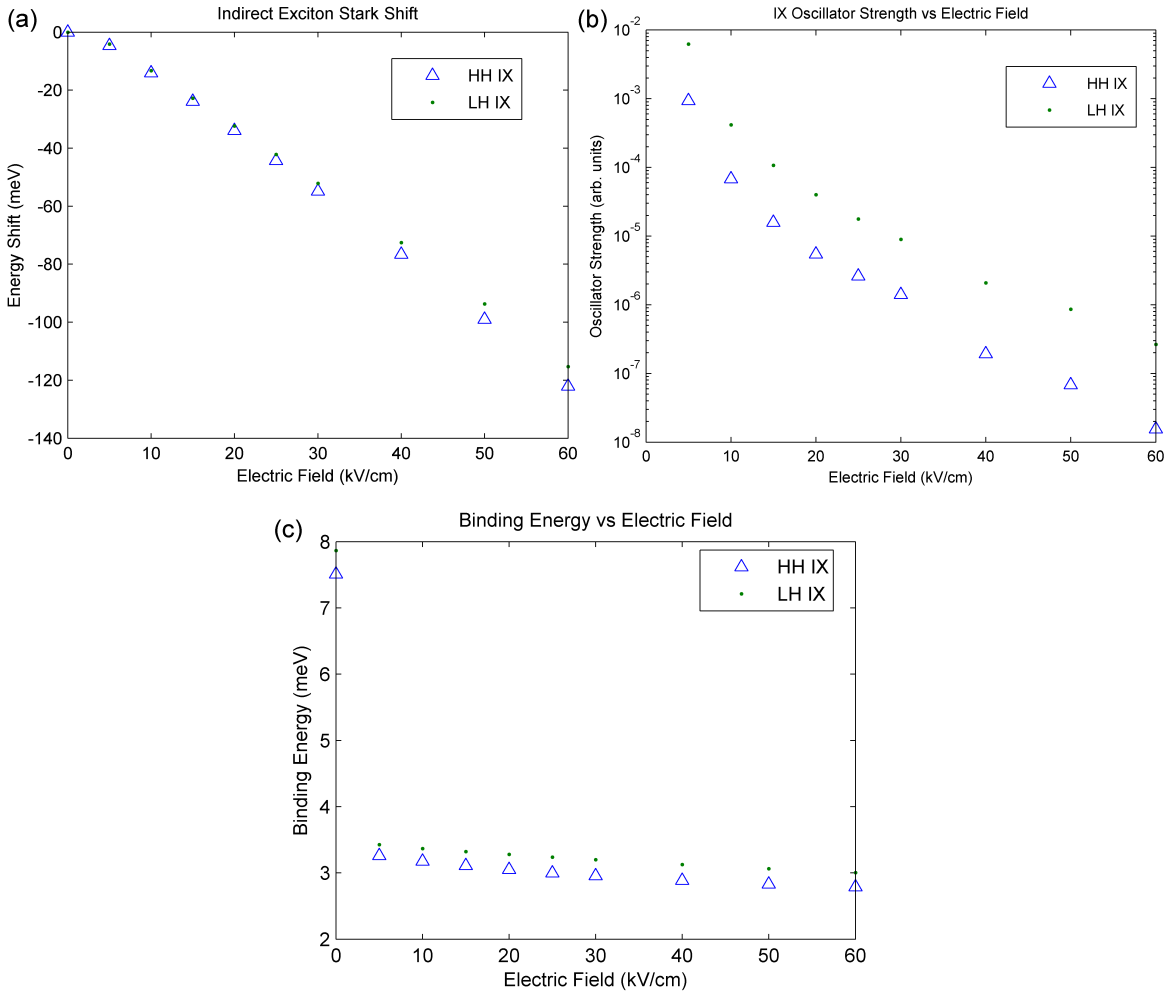

Figure 3: Simulated (a) IX Stark shift, (b) oscillator strength, and (c) binding energy vs electric field, calculated from the numerical solution of the electron-hole two-particle problem. The zero energy position for the Stark shift corresponds to the energy of the DX state. This Stark shift is the change in energy of the IX state directly due to the field, and it does not include the change in binding energy, which is plotted separately in (c). The simulation was entirely the work of Marzena Szymanska, collaborating on this project.

IX oscillator strength, binding energy, and the Stark shift as a function of the electric field. Figure 3(a) plots the Stark shift of the IX states as a function of electric field across the wells. As expected, the shift is slightly lower for the LH IX state than the HH IX state, since the LH can more easily penetrate into the barrier, slightly decreasing the dipole moment.

Figure 3(b) plots this electron-hole overlap matrix element as a function of electric field, where it has been normalized to that of the LH at zero field. The probability of electron-hole recombination is proportional to this quantity. Two very important effects of the electrical biasing are displayed here. First, the increasing polarization of the wavefunction is exponentially suppressing the recombination probability by decreasing the electron-hole overlap. This feature accounts for the long IX recombination lifetime, which in the absence of likely non-radiative decay channels leads to a long IX population lifetime.

The second important feature of Figure 3(b) is that the LH oscillator strength for the IX is about 10 times larger than that of the HH IX. This will feature prominently in one explanation of the darkening phenomenon. To my knowledge, the oscillator strength of the LH IX has not been previously reported upon, leaving this simulation our sole justification for this feature. However, it may be explained qualitatively from the spatial character of these excitons. The LH IX penetrates more into the barrier separating the wells due to its lighter mass. Since the electron is located in the opposing well in the IX case, the LH IX has an increased overlap with its paired electron than a corresponding HH IX.

Because Figure 3(b) is essentially tracking the electron-hole overlap integral, we can also see that the exchange interaction responsible for the bright/dark splitting in the direct exciton case will be orders of magnitude smaller in the IX case. Thus, it is clear that in the absence of BEC, this energy difference will be essentially unimportant.

Figure 3(c) plots the binding energy as calculated in the numerical solution. The binding energy of both HH and LH excitons fall off rapidly with increasing field to about 3 meV, as the electron-hole separation settles to be nearly constant.

1.4 INTERACTIONS

1.4.1 IX-IX Repulsion

Indirect excitons are essentially electric dipoles with fixed orientation, and we can account for the overall repulsion of two excitons by writing down the Coulomb energy of each pair among the four particles. The repulsive pairs (e-e and h-h) are separated by r, the interexciton distance. The attractive pairs (e-h) are separated by $\sqrt{r^2+d^2}$, giving the simple expression for the Coulomb energy

$$E_{int} = \frac{e^2}{4\pi\epsilon_{\mathrm{GaAs}}}\left(\frac{2}{r} - \frac{2}{\sqrt{r^2+d^2}}\right). \tag{1.10}$$

At large exciton separation, this expression can be expanded, in small (d/r), to obtain the dipole-like behavior,

$$E_{int} = \frac{e^2 d^2}{4\pi\epsilon_{\mathrm{GaAs}} r^3}. \tag{1.11}$$

A mean-field treatment of this interaction yields the energy of a pair of charges on a parallel-plate capacitor. Specifically, the electric field due to an exciton density n, $\vec{\mathrm{E}}$=(en/ϵ_{GaAs}), gives an overall blue shift of a dipole equal to

$$E_{int} = (ed)\frac{en}{\epsilon_{\mathrm{GaAs}}}. \tag{1.12}$$

This equation for the blue shift is sensibly called the capacitor formula. If we adopt the notation for this shift

$$E_{int} = \gamma n, \tag{1.13}$$

and estimate d = 18 nm, the capacitor formula predicts $\gamma = 2.6\times10^{-10}$ meV cm^2. It has been pointed out that the mean field treatment will vastly overestimate the blue shift by neglecting the spatial anti-correlation of the excitons at low temperature [87, 66, 38]. If we treat the interaction classically, then excitons will not approach closer than their kinetic energy allows, creating a depleted region around each exciton. If we allow an exciton to have kinetic energy k_BT, the classical turning point, at which the kinetic energy equals the potential energy, occurs at 50 nm for d = 18 nm at 2 K. This situation is demonstrated in Figure 4. This classical argument is sufficient to motivate the depletion, but is quantitatively incorrect for this temperature range because the interaction is decidedly in the quantum

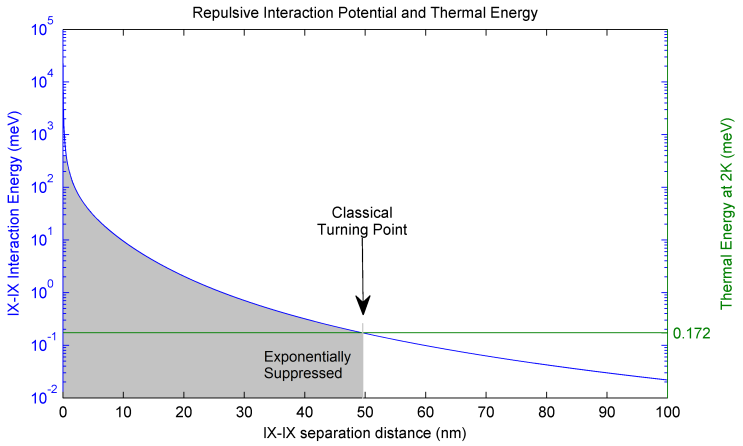

Figure 4: Classical turning point. Treating two IXs as point particles with an interaction given by Eq. (1.10), at 2 K, the particles have enough thermal energy to close to a distance of about 50 nm.

regime. Specifically, the thermal wavelength of a HH exciton (using the in-plane mass) at 2 K is 120 nm, much larger than both d (the length scale of the uncorrelated interaction) and the classical turning point distance, so there will be appreciable penetration into the classically forbidden region. Thus, calculation of the shift requires numerical simulation. This has been performed by Zimmermann for our general structure, taking into account both the two-particle anticorrelation as well as allowing Van der Waals polarization (in-plane) to reduce the repulsive interaction. Defining a temperature-dependent correction factor to the capacitor formula,

$$E_{int} = f(T)\frac{nde^2}{\epsilon_{\mathrm{GaAs}}}, \tag{1.14}$$

the simulation arrived at f(2 K) = 0.08, nearly independent of well-width. This correction, of course, approaches 1 at higher temperature as the mean kinetic energy is sufficient to nullify this anticorrelation. At densities where we may consider only pairwise interactions, when it is unlikely to find three particles within the range of the interaction, this is roughly the blue shift that we should expect, corresponding to $\gamma = 2.0\times10^{-11}$ meV cm^2. However, Voros et al.[81] have measured, very approximately, a value of $\gamma = 0.9 \times 10^{-10}$ meV cm^2, which is closer to the mean field solution than the prediction that includes correlations.

Laikhtman and Rapaport [38] point out that in the quantum scattering limit, the condition for quantum degeneracy $n^{1/2} \ll k_{therm}$ is very nearly the same as the condition for multiexciton (more than pairwise) interactions to become important,

$$n \ll k_{therm}^2 \ln \frac{d^2 k_{\rm therm} e^2 m_X}{4\pi\hbar^2 \epsilon_{\rm GaAs}},$$

where the logarithmic factor is only 1.6 at 2 K in our system. Thus, in seeking a Bose condensed state, one must deal with multiparticle correlations. With the onset of these multiexciton correlations, Laikhtman and Rapaport label the state as a liquid, rather than a gas. This label is somewhat misleading as the correlated state lacks the characteristic interparticle attraction that allows traditional liquids to behave as we expect, i.e. forming droplets of nearly fixed density. Due to the existence of a more traditional electron-hole liquid state that does have this behavior in bulk, a "strongly-correlated" label is probably less likely to confuse the issue. In any case, from his argument, we might expect that the degenerate bosonic state, characterized by positive spatial correlation, will probably occur in a range of density/temperature where it will compete with the anticorrelation caused by the repulsive interaction.

It is often the case that when analyzing the problem of an interacting BEC, the interparticle repulsion is treated with an effective hard-core interaction and using only s-wave scattering. This is often appropriate, as the length scale of the interaction is in many problems much smaller than the typical wavelength. In this limit, the scattering amplitude is roughly constant. S-wave scattering also makes sense in this limit, as the internal structure of the interaction will not matter when only very long wavelengths are involved. This, however, is not the case for the IX problem; the range of the interaction and thermal wavelengths are similar. Zimmermann [87] showed through numerical simulation of the two-body problem that $m \neq 0$ components make a large contribution to the total scattering amplitude even at $T = 6K$ (down to momenta about one-tenth of the thermal average) and that the scattering amplitude is far from flat. From this we see that the interactions in this system will be very different from those of the canonical interacting BEC treatments.

The difficulty of accurately estimating these interactions is a large burden to experiments. One would often like to make an estimate of the local exciton density, and, without an

accurate calibration for absorption efficiency and decay dynamics, the logical approach is to use the interaction blue shift to determine the density. However, the mean field estimate and the estimate taking account of correlations predict interaction strengths differing by about a factor of ten, and these figures have not been tightly restricted by experimental work. Therefore, this approach can only give a ballpark estimate for the density.

1.4.2 Biexcitons and Trions

In the direct exciton case, due to Van der Waals polarization of the wavefunctions, there is an attractive interaction at small interexciton separation. This allows the formation of a biexciton molecule, BiDX=(DX+DX), at low temperature. The binding energy of this molecule in GaAs wells has been measured in various works, summarized in [2], and with a well-width of about 15 nm, we expect from these scattered results to find a binding energy somewhere between 0.9 and 1.8 meV. In experiments on GaAs quantum wells, there is typically a spectral line at about 1 meV below that of the DX state, in accord with the binding energy predictions. However, there has been some contention around the identification of this spectral line, as trion (DX^-=DX+e or DX^+=DX+h) states are predicted to have roughly the same binding energy. For example, Osborne et al. [54] demonstrated that, in samples that were designed to sweep photoexcited holes from the AlGaAs barrier into the quantum wells, forming trions, many of the expected biexciton spectral characteristics were observed, i.e. a similar binding energy, a low-energy tail in the spectrum, superlinear density dependence, and a well-width dependence that follows the same trend as that predicted by Kleinmann [30]. The argument was then made by Osborne et al. that it was unlikely that other researchers had observed biexcitons with the same signatures and that they had simply mislabeled the spectral line. In response, Adachi [2] showed that, in resonantly-excited undoped samples, the polarization dependence of pump-probe signals was consistent only with biexciton formation[12]. We are left to conclude from these two rather convincing studies that there are indeed two phenomena with very similar spectral characteristics, and that differ-

[12]Specifically, they showed a dependence of the differential transmission signal from co-polarized and cross-polarized pump and probe consistent with the fact that the ground state biexciton is composed of excitons with opposite spin

entiation between the two cases requires a good deal of careful experimentation. The typical practice in the literature is that the label of trion or biexciton is attributed based on whether one expects a large amount of free carriers in the quantum wells, e.g. it is a trion if using modulation doped wells or when excited above the barrier energy. Further complicating the issue, Phillips et al. have reported measuring trions (identified by comparison of magnetic energy shifts to those of trions in doped cases) even in undoped quantum wells with resonant excitation [58]. In the case of biased coupled quantum wells, it is unclear whether trions or biexcitons will be the most stable. It is certainly true that due to the biasing, there is a net charge imbalance in each well, but it is unknown to what extent the carriers responsible for the charge imbalance will be bound in IXs during the time in which DXs are still remaining in the system. Since the IX state is the lowest energy state and transitions to this state are rapid, this is more a question of the cascade dynamics than the equilibrium occupation statistics. This identification could be tested by the application of an in-plane electric field, as it has been shown [65] that trions will drift while neutral excitons will not. However, these fields would be difficult to implement in our experiments. Since there are no particular issues in this experimental pursuit that rely on strict identification of this line, beyond knowing that it will behave in a similar way to the DX states under stress, for the remainder of this work this state will be referred to as the BiDX state, in accord with previous work in the area.[13].

Consideration of IX biexcitons is of more direct interest to the experiment at hand. The very small degree to which the Van der Waals effect may polarize the wavefunction in the IX case essentially becomes a negligible perturbation to the repulsion caused by the large electron-hole growth-direction separation, removing the possibility of IX biexcitons in our system. It is not wholly impossible to achieve interwell biexcitons in a coupled quantum well system, when the well separation is small compared to the 3D bohr radius and particularly when the hole mass is much larger than that of the electron [66, 39]. However, the IX mass ratio, $\mu = m_c/m_{hh}$, using in-plane masses from Eqns.(1.7a)–(1.7d) is 0.56. The well

[13]There is also another spectral line with similar spectral characteristics. Charbonneau [13] has shown that spectra from excitons bound to impurities have very nearly the same binding energy as that of biexcitons, distinguished only by the density dependence (where the impurity-bound states quench rather than increase with density). We disregard this possibility since we observe no quenching.

separation at which there should be a bound biexciton state for this case is $0.31a_b$ [39] or $0.43a_b$ [66]. In the studies cited, it was further showed that for a well separation $> 0.9a_b$, there is no interparticle separation at which the interaction is attractive[14].

1.5 BOSE-EINSTEIN CONDENSATION OF NON-INTERACTING EXCITONS

1.5.1 Excitons as Bosons

We have shown that at low temperature, nearly all of the carriers in coupled quantum wells with an applied electric field will be in the form of bound interwell molecules. Seen as a composite particle, these excitons must have integer spin and obey bosonic statistics, so a BEC phase is expected to exist, if not prevented by some other mechanism. For composite particles, this means that, in the range of densities where there is considerable overlap of exciton wavefunctions but below the density where the nature of the fermionic constituents is important, the population is expected to show an accumulation of particles in the lowest energy quantum state.

The determination of whether the excitons are acting as bosons can be seen in the commutation relations of the exciton creation/destruction operators. If these operators have the commutation relation,

$$[a, a^\dagger] = \delta_{k,k'}, \tag{1.15}$$

the particles should behave as ideal bosons. The anticommuting electron and hole operators cause a deviation from this on the order of the electron-electron and hole-hole overlap which is characterized by the density and the size of the exciton, a_{ex} [47],

$$[\hat{a}, \hat{a}^\dagger] = \delta_{k,k} + \mathcal{O}(na_{ex}^2). \tag{1.16}$$

Clearly, at densities where na_{ex}^2 is small, we may treat the composite particle as a boson. This condition also exists for atomic species, and we can see that in atomic BEC experiments,

[14] Zimmermann et al. [66] furthermore showed that this is true even in the case of opposite spin IXs, where in the DX case this is a predominantly attractive interaction.

this condition is exceedingly easy to fulfill. In the original Rb-87 BEC, the number density was roughly 10^{12} cm^{-3} [4]. The relevant 3D quantity $\mathrm{na}^3_{\mathrm{atomic}} \approx 10^{-11}$.

An order-of-magnitude estimate for the onset of BEC is when the boson wavefunctions overlap. With a thermal wavelength defined by:

$$\lambda_T = \frac{h}{\sqrt{2\pi m k_B T}}, \tag{1.17}$$

this requires $\mathrm{n}\lambda_T^2 \sim 1$. If this can be achieved without violating $\mathrm{na}^2_{\mathrm{ex}} \ll 1$, then BEC of the composite boson system should be achievable.

1.5.2 Ideal Gas in 3D - Flat Potential

The case of BEC in an ideal Bose gas has many problems, but provides a foundation for discussion of more realistic scenarios. Following the development of the theory of bosonic statistics, the prediction of the BEC state arose from Einstein's observation that at any temperature there are a finite number of bosons allowed to be in excited states. Putting any particles into the system after this limit requires that they go into the ground state.

The Bose distribution tells us that the number of particles in each state is given by

$$N_i = \frac{1}{e^{\beta(E_i-\mu)} - 1}, \tag{1.18}$$

so the constraint on the total number of particles, N, is that

$$N = \sum_i \frac{1}{e^{\beta(E_i-\mu)} - 1}. \tag{1.19}$$

In order to work with this, one takes the thermodynamic limit $\left(N\to\infty, V\to\infty, \frac{\mathrm{N}}{\mathrm{V}}=\mathrm{n}\right)$ to yield a continuous spectrum of states and turns the sum into an integral using the density of states. In the 3D case with no trapping, the density of states goes as $E^{1/2}$ and the integral reads:

$$N_{ex} = \frac{2\pi V}{h^3}(2m)^{\frac{3}{2}} \int_0^\infty \frac{E^{\frac{1}{2}}}{e^{\beta(E-\mu)} - 1} dE. \tag{1.20}$$

The integral conversion assigns zero weight to the ground state, which is problematic if the occupation of this state becomes appreciable. Therefore, we must label this integral as the number of excited states and count the ground state occupation separately as:

$$N_0 = \frac{1}{e^{-\beta\mu} - 1}. \tag{1.21}$$

Introducing the fugacity, $z{=}e^{\beta\mu}$, and changing to the variable x=βE, we can turn Eq. (1.20) into the Bose integral [56],

$$g_n(z) = \frac{1}{\Gamma(n)} \int_0^\infty \frac{x^{n-1}}{z^{-1}e^x - 1} dx. \tag{1.22}$$

The integral converges to a finite value, and it has a maximum value when $z{=}1$, corresponding to $\mu{=}0$. For $z{=}1$, the Bose integral is simply the Riemann Zeta function, ζ(n), and the maximum density, $\frac{\mathrm{N}}{\mathrm{V}}$, explicitly achievable from this distribution is

$$n_{ex} = \zeta(\tfrac{3}{2}) \left(\frac{m k_B T}{2\pi\hbar^2} \right)^{\frac{3}{2}}. \tag{1.23}$$

Thus, all particles beyond this limit must be in the ground state. We can see from Eq. (1.21) that, when μ approaches 0, the ground state population will become very large.

It is also easy to work backward from the result and see that $\mu{=}0$ corresponds to the case of a condensate. Because of the requirement that additional particles will go into the ground state, there is no additional entropy caused by gaining a particle. Using the definition of the chemical potential as

$$\mu = \left. \frac{\delta F}{\delta N} \right|_{T,V} \tag{1.24}$$

where F is the Helmholtz free energy, $F = U{-}TS$, the chemical potential must, therefore, simply be equal to the change in internal energy upon addition of excitons. Since there are no interactions in the ideal case and the particle goes into the $E{=}0$ state, there is no energy cost and $\mu{=}0$. Similarly, when weak interparticle interactions exist, μ will simply be the per-particle energy cost to change the density; i.e. $\mu{=}\gamma n$, in the mean field approximation[15].

[15]This definition is simply to elucidate the nature of μ in this context. It allows $\mu{>}0$, so care must be taken to avoid the Bose distribution becoming negative for low energy states. This is accomplished by keeping $E{=}0$ as the unshifted single-particle ground state and including the per-particle interaction energy in the Hamiltonian used in the distribution function.

We can define the critical density at some temperature by Eq. (1.23). If we increase the density beyond this, we must have a macroscopic ground state occupation. Similarly, we may hold the density fixed and define a critical temperature,

$$T_C = \left(\frac{n}{\zeta(\frac{3}{2})}\right)^{\frac{2}{3}} \frac{1}{2\pi m k_B}. \tag{1.25}$$

It is clear from this that a low mass particle makes BEC much easier to achieve. It should be noted that the BEC criterion in Eq. (1.23) only offers the correction factor of $\zeta(\frac{3}{2})$=2.6 to the order-of-magnitude estimate, $n\lambda_T^3 \sim 1$.

1.5.3 Ideal Gas in 2D - Flat Potential

In the two-dimensional, untrapped case, the density of states is $\frac{mL^2}{\pi\hbar^2}$, independent of energy. Thus the Bose integral corresponds to n=1, where the integral takes the analytic form [1]:

$$g_1(z) = -\ln(1-z), \tag{1.26}$$

which clearly diverges for z = 1, allowing an infinite number of excited states. Thus, there is no sharp transition to a BEC state in a 2D system with a flat potential. The problem in this case is that the low-energy density of states is too large. The low-energy excited states are able to include all of the particles rather than forcing the system to form a single macroscopically occupied state. It was demonstrated by Hohenberg [24] that, at T $\neq$ 0, long-range order may not persist over infinite length in d $\leq$ 2, and this is a corollary of the more general argument that there cannot be any spontaneously broken symmetries at T $\neq$ 0 for d $\leq$ 2.

However, this argument does not preclude long range coherence altogether. At low temperature, the appearance of a 'quasi-condensate' in 2D is characterized by regions of spatial coherence larger than the thermal de Broglie wavelength but smaller than the size of the system [61]. This state is typically described by the presence of free vortices. At increased temperature, the system smoothly transitions to coherence on the length scale of the thermal wavelength. With decreasing temperature, there is a sharp transition to a superfluid state, the Berezinski-Kosterlitz-Thouless transition, corresponding to the binding of vortex/anti-vortex pairs, which significantly slows the decay of spatial coherence.

1.5.4 Ideal Gas in 2D - Harmonic Trap

The argument above is, however, not an objection to all 2D BEC studies, as it does not constrain the trapped 2D case or even the more general finite 2D case. We can look at the case of a 2D harmonic oscillator potential to demonstrate this, as it is the relevant potential for this study. The treatment here is simple and consistent with the traditional state-counting derivation of a BEC. It has been shown by more thorough analysis (also considering weak interactions) that a true condensate may be formed in 2D by employing traps [57, 21]. In this case, one counts the states by the indices i_x, i_y, where the energy of a state is given by,

$$E = \hbar\omega(i_x + i_y + 1). \tag{1.27}$$

If we define $i_x + i_y = j$, each energy level has degeneracy (j-1). When we turn this into an integral, though, we approximate that we can drop the constant from this degeneracy as it misrepresents the low-energy spectrum (the integral allows $0<j<1$, making unphysical degeneracy factors). In fact, if we included this constant in the degeneracy, we would again see a diverging excited state occupation from the constant term alone (highlighting the importance of the low-energy spectrum), but in this case it is unphysical. So we approximate (j-1)$\sim$j, and write

$$N_{ex} = \int_0^\infty \frac{j}{z^{-1}e^{\beta\hbar\omega j} - 1} dj. \tag{1.28}$$

Clearly, we can again turn this into a Bose integral, where this time the integral will converge at μ=0. Defining $x = \beta\hbar\omega j$,

$$\begin{aligned} N_{ex} = N_C &= \left(\frac{1}{\beta\hbar\omega}\right)^2 \int_0^\infty \frac{x}{z^{-1}e^x - 1} dx \\ &= \zeta(2)\left(\frac{k_B T}{\hbar\omega}\right)^2 = 1.64\left(\frac{k_B T}{\hbar\omega}\right)^2 \end{aligned} \tag{1.29}$$

The critical temperature then, is defined as,

$$T_C = \left(\frac{N\hbar\omega}{k_B}\right)^{\frac{1}{2}}. \tag{1.30}$$

As a numerical reference, if we have a relatively weak harmonic potential (for the strain-based mechanism that will be explained in the following section), $V = \frac{1}{2}\alpha r^2$, with $\alpha = 50$ eV cm^{-2}, at 2 K, this corresponds to BEC when the trap contains 3×10^5 particles.

1.6 THE ROLE OF INTERACTIONS

The ideal BEC is unphysical in a few important ways. Most obviously, it requires a population in equilibrium without accounting for the mechanism that provides it. A system with no direct interactions between the particles of interest, but with those particles interacting with a reservoir, will still contain an effective interparticle interaction. The recent photon BEC experiment [29] are an example of this, where cavity photons interact via excitations of an intracavity dye. So, first of all, the purely non-interacting, thermalized case is fictitious.

The second problem with the ideal case is that the BEC is not stable against fragmentation into multiple BECs in degenerate states or in states with negligibly small ΔE. The situation is different when we allow a weak repulsive interaction between particles because the condensate can now benefit from the difference in exchange energy between a single BEC and a fragmented state. Nozieres [53] showed that due to the requirement to symmetrize the bosonic wavefunction, a BEC split among two states will have a higher energy by an amount proportional to the interaction strength and extensive with the size of the system. Thus, the interacting BEC is stabilized by a macroscopic energy scale, while in the ideal case, there is no barrier to fragmentation into many nearby states. Combescot and Snoke have additionally shown that this exchange energy argument remains valid for composite bosons, as in the case of excitons [16]. So the standard picture of BEC in a single ground state is actually unphysical in the non-interacting case.

It is clear that interactions are vital to the existence of a BEC in the traditional sense. The problem of dealing with these interactions quantitatively and determining how they influence the final many-body BEC state is not so simple. However, the problem of a weakly-interacting dilute Bose gas (WIDBG) can be treated analytically, and thus provides a useful reference. While the WIDBG solution is probably not valid in the case of indirect excitons, the general role of interactions in a more strongly interacting system may be gleaned from this case.

1.6.1 Weakly-Interacting, Dilute Bose Gas

Historically, Bogoliubov first provided an analytical solution to the behavior of the WIDBG by emphasizing the importance of the spontaneously broken gauge symmetry and explicitly building it into the formulation of the problem. Specifically, the exciton destruction operator is transformed to include a c-number component representing the ground state [47]:

$$\hat{a}_{\vec{k}} = \sqrt{N_0} e^{i\theta} \delta(\vec{k}) + \hat{\alpha}_{\vec{k}}, \tag{1.31}$$

where $\alpha_{\vec{k}}$ is the normal boson destruction operator and we have assumed the particles to be condensing in the zero-momentum state[16]. By this construction, one is essentially demanding that there be a coherent state of particles in the ground state, with definite phase θ. This is sensible, remembering that a coherent state is an eigenstate of the destruction operator (where $\hat{a}_k$ is a measure of the complex amplitude). With $\hat{\alpha}_{\vec{k}}$ as a small perturbation on $\hat{a}_0$, the large c-number component of $\hat{a}_0$ will cause the k=0 state to be an eigenstate of $\hat{a}_0$. This treatment requires that N is large, so that one may state without contradiction that $\hat{a}_0^\dagger \hat{a}_0$ yields on average N_0 (what one would expect from a Fock state) while simultaneously claiming coherence in the ground state. The salvation of this apparent contradiction of number-phase uncertainty is that, at large N, the variance in $\hat{N}$ becomes negligible[17].

The general two-particle Hamiltonian for free interacting bosons,

$$H = \sum_k \frac{\hbar^2 k^2}{2m} + \frac{1}{2V} \sum_{\vec{p},\vec{q},\vec{k}} U_{\vec{k}} \hat{a}_{\vec{p}}^\dagger \hat{a}_{\vec{q}}^\dagger \hat{a}_{\vec{q}+\vec{k}} \hat{a}_{\vec{p}-\vec{k}}, \tag{1.32}$$

can be expanded using the Bogoliubov approximation, Eq. 1.31, and rewritten so that it is diagonal in terms of new operators [70][18],

$$\hat{\alpha}_{\hat{k}} = \frac{\hat{\xi}_{\vec{k}} - A_{\vec{k}} \hat{\xi}_{-\vec{k}}^\dagger}{\sqrt{1 - A_{\vec{k}}^2}} e^{-i\theta}, \qquad \hat{\alpha}_{\hat{k}}^\dagger = \frac{\hat{\xi}_{\vec{k}}^\dagger - A_{\vec{k}} \hat{\xi}_{-\vec{k}}}{\sqrt{1 - A_{\vec{k}}^2}} e^{i\theta}, \tag{1.33}$$

[16] This is not necessary for this construction, only a simplification for the current discussion.

[17] See, for example, Snoke, Sections 4.4 and 11.1 [70]

[18] This requires discarding terms which are more than quadratic in the excited state amplitude operators $\hat{\alpha}_{k\neq 0}$.

with the definitions,

$$A_{\vec{k}} = \frac{V}{N_0 U_{\vec{k}}}\left(\frac{\hbar^2 k^2}{2m} + \frac{N_0 U_{\vec{k}}}{V} - E(\vec{k})\right), \qquad E(\vec{k}) = \sqrt{\left(\frac{\hbar^2 k^2}{2m}\right)^2 + \frac{N_0 U_{\vec{k}} \hbar^2 k^2}{mV}}. \tag{1.34}$$

In terms of $\hat{\xi}$ and $\hat{\xi}^\dagger$, the Hamiltonian is now

$$H = \frac{U_0 N_0^2}{2V} + \frac{1}{2}\sum_{\vec{k}}\left(E(\vec{k}) - \frac{\hbar^2 k^2}{2m} - \frac{U_{\vec{k}} N_0}{V}\right) + \sum_{\vec{k}} E(\vec{k}) \hat{\xi}^\dagger_{\vec{k}} \hat{\xi}_{\vec{k}}, \tag{1.35}$$

and the spectrum of excitations can be read off from $E(\vec{k})$. In addition, one can easily show that the operators $\hat{\xi}$ and $\hat{\xi}^\dagger$ obey bosonic commutation rules by inverting Eq. (1.33):

$$\hat{\xi}^\dagger_{\vec{k}} = \hat{\alpha}_{-\vec{k}} \frac{A_{\vec{k}} e^{i\theta}}{\sqrt{1 - A_{\vec{k}}^2}} + \hat{\alpha}^\dagger_{\vec{k}} \frac{e^{-i\theta}}{\sqrt{1 - A_{\vec{k}}^2}}, \qquad \hat{\xi}_{\vec{k}} = \hat{\alpha}^\dagger_{-\vec{k}} \frac{A_{\vec{k}} e^{-i\theta}}{\sqrt{1 - A_{\vec{k}}^2}} + \hat{\alpha}_{\vec{k}} \frac{e^{i\theta}}{\sqrt{1 - A_{\vec{k}}^2}}, \tag{1.36}$$

and directly working out that the commutator $[\hat{\xi}, \hat{\xi}^\dagger] = 1$, using $[\hat{\alpha}, \hat{\alpha}^\dagger] = 1$.

At this point, we are again presented the opportunity to highlight the importance of interparticle interactions. At low momentum, the dispersion relation for excitations is linear[19], and the slope of this dispersion yields the superfluid critical velocity from the Landau criteria,

$$v_{crit} = \sqrt{\frac{N_0 U_0}{mV}}. \tag{1.37}$$

Here it is clear that the interparticle interactions make superfluidity possible. Without this interaction, the critical velocity would vanish. This linear branch of the dispersion has been very clearly observed experimentally in polariton BECs [77, 27, 7].

It is of interest to determine the degree to which the condensate is depleted by the interactions, and this can be analytically calculated in the Bogoliubov model. We can write the number of particles in the condensate as:

$$N_0 = N - \sum_{\vec{k} \neq 0} \hat{\alpha}^\dagger_{\vec{k}} \hat{\alpha}_{\vec{k}}. \tag{1.38}$$

Using the Bogoliubov transformation, Eq. (1.33), we can additionally expand $\hat{\alpha}^\dagger_{\vec{k}} \hat{\alpha}_{\vec{k}}$,

$$\hat{\alpha}^\dagger_{\vec{k}} \hat{\alpha}_{\vec{k}} = \frac{\hat{\xi}^\dagger_{\vec{k}} \hat{\xi}_{\vec{k}} + \hat{\xi}^\dagger_{-\vec{k}} \hat{\xi}_{-\vec{k}} + A_{\vec{k}}^2}{1 - A_{\vec{k}}^2}, \tag{1.39}$$

[19] This excitation represents the massless Goldstone boson arising from breaking the gauge symmetry.

with the last term provided by putting the operators into normal order. Now, the thermal statistics of the $\langle\hat{\xi}^{\dagger}_{\vec{k}}\hat{\xi}_{\vec{k}}\rangle$ determine the occupation of real particles. Since these bosonic excitations are non-interacting and their number is not conserved, their occupation statistics are determined by the Bose distribution with $\mu = 0$. The average number of particles in the condensate is then:

$$N_0 = N - \sum_{\vec{k}\neq 0}\left(\frac{1+A^2_{\vec{k}}}{(1-A^2_{\vec{k}})(e^{\beta E(k)}-1)} + \frac{A^2_{\vec{k}}}{1-A^2_{\vec{k}}}\right). \tag{1.40}$$

The latter term represents the zero-temperature depletion of the condensate, and the thermal depletion is described by the first term. This can be further simplified with further approximations, but the important point is that it can be shown analytically, by building coherence into the ground state via the Bogoluibov approximation, that the condensate fraction is reduced by interactions. The quantum depletion with weak interactions is a rather small perturbation[20]. However, in the strongly interacting case of liquid helium, the condensate fraction reaches a maximum of only about 10% [72], as $T\rightarrow 0$.

If one performs an interference experiment, overlapping an image signal[21] with another displaced by $\Delta\vec{r}$, there will be a characteristic length scale for $\Delta\vec{r}$ over which the interference fringes will die away. This is characterized by the matrix element:

$$\langle\Psi^{\dagger}(\vec{r})\Psi(\vec{r}+\Delta\vec{r})\rangle = \frac{1}{N}\sum_{\vec{k}}\langle\hat{a}^{\dagger}_{\vec{k}}\hat{a}_{\vec{k}}\rangle e^{i\vec{k}\cdot|\Delta\vec{r}|}. \tag{1.41}$$

Due to the large occupation of the ground state in the condensed phase, this matrix element is significant over rather large distances. This is referred to as the onset of off-diagonal, long-range order (ODLRO). In the weakly intereacting case, we begin by separating the condensate portion out:

$$\langle\Psi^{\dagger}(\vec{r})\Psi(\vec{r}+\Delta\vec{r})\rangle = \frac{N_0}{N} + \sum_{\vec{k}\neq 0}\hat{\alpha}^{\dagger}_{\vec{k}}\hat{\alpha}_{\vec{k}}e^{i\vec{k}\cdot|\Delta\vec{r}|}. \tag{1.42}$$

[20]For example, the quantum depletion of ^{23}Na, in 3D, at n = 10^{14} cm^{-2} is predicted to be 0.2% by Bogoluibov theory. The validity of these predictions has been experimentally verified, surpisingly, even up to a depletion of about 50%[84].

[21]This may by the particles themselves, as in atomic experiments, or photoluminescence in the exciton case.

Eq. (1.40) and Eq. (1.39) can be used to write this in terms of the occupation of quasiparticles.

$$\langle \Psi^\dagger(\vec{r})\Psi(\vec{r}+\Delta\vec{r})\rangle = 1 - \frac{1}{N}\sum_{\vec{k}}\left(\frac{1+A_{\vec{k}}^2}{(1-A_{\vec{k}}^2)(e^{\beta E(k)}-1)} + \frac{A_{\vec{k}}^2}{1-A_{\vec{k}}^2}\right)\left(1-e^{i\vec{k}\cdot|\Delta\vec{r}|}\right). \quad (1.43)$$

This expression could be used to numerically estimate this quantity. However, the simplified statement, Eq. (1.42), is more instructive. For the Bogoliubov approximation to be valid, the first term, $\frac{N_0}{N}$, must dominate. This means that over any length scale, the coherence is maintained.

In contrast, in a non-degenerate ensemble, we expect this matrix element to fall-off very quickly with the separation distance. It is not so difficult to show that the appropriate length scale is the thermal wavelength. We are interested in the ensemble average of the operator in Eq. (1.40). For the Maxwell-Boltzmann distribution, this average is defined, for some operator $\hat{C}$, as

$$\langle \hat{C}\rangle_{ens} = \sum_j \frac{\langle j|\hat{C}e^{-\beta\hat{H}}|j\rangle}{\langle j|e^{-\beta\hat{H}}|j\rangle}. \quad (1.44)$$

For the off-diagonal matrix element, it makes sense to expand in the momentum basis, where we will work in 2D, due to the geometry of our experimental system. In the non-degenerate case, the expression above is then:

$$\begin{aligned}\langle \Psi^\dagger(\vec{r})\Psi(\vec{r}+\Delta\vec{r})\rangle &= \frac{\int_0^\infty\int_0^{2\pi} k e^{-\frac{\beta\hbar^2k^2}{2m}} e^{ik|\Delta|\cos\theta}dkd\theta}{\int_0^\infty\int_0^{2\pi} k e^{-\frac{\beta\hbar^2k^2}{2m}}dkd\theta} \\ &= \frac{\hbar^2}{mk_BT}\int_0^\infty k e^{-\frac{\beta\hbar^2k^2}{2m}} J_0(k|\Delta|)dk \\ &= e^{-\frac{mk_BT|\Delta|^2}{2\hbar^2}} \quad = e^{-\frac{|\Delta|^2}{2\pi\lambda_T^2}}\end{aligned} \quad (1.45)$$

The off-diagonal matrix element decreases exponentially with distance, with a characteristic length scale given by the thermal wavelength, λ_T, as intuition would suggest.

The predictions in this section are applicable to the "weakly"-interacting case. We originally assumed that only a very small fraction of particles were not in the condensate, and Eq. (1.40) demonstrates that stronger interactions reduce the validity of this statement. It is clear from Eq. (1.40) that the zero-temperature depletion of the condensate (the second

term) will become significant to the degree that $\frac{N_0 U_{\vec{k}}}{V}$ compares with the typical kinetic energy, $\frac{\hbar k^2}{2m}$. We know from the measured blue shifts in the IX system, on the scale of meV, and the dispersion relation of these excitons that the interaction energy will dominate and that there would be significant depletion for even the lowest range of densities in our experiments. Therefore, we cannot expect the quantitative predictions of the Bogoluibov theory to hold for the case at hand. One of the most interesting aspects of the search for IX BEC is that so much is unknown about the behavior of this system, so that its realization will yield a wealth of characteristics that may be used to hone our current understanding of strongly-interacting, degenerate systems.

1.6.2 Dark or Bright BEC

BEC always occurs in the lowest energy state available to the particles. In our case, we exclude the actual ground state of the system, consisting of zero excitons, from the available states because the excitons are able to establish a thermal quasi-equilibrium well before recombination occurs, so that the number of excitons is nearly conserved. The relevant ground state is then the lowest energy state of N excitons. However, experiments on this system have always proceeded with expectations of "seeing" the condensate through its luminescence. This may not be the case. From the simple discussion in Section 1.1, the exchange interaction between electron and hole should cause the lowest exciton state to be dark. This is supported by more rigorous theoretical works by Combescot[17, 18], predicting that BEC should indeed occur in the dark exciton state.

A dark BEC is an interesting prospect, but it is unclear to what extent this prediction is valid for IXs. On one hand, the bright/dark splitting presents an advantage for BEC creation, as increased degeneracy of low-lying energy states tends to suppress BEC. However, the bright/dark splitting in the IX states should be extremely small, as it relies on the electron-hole overlap that is suppressed for these states[22]. This tiny splitting may be overwhelmed by other, normally neglected, effects. Obviously, the prediction of a dark BEC has added

[22]It is suppressed compared to the already small 10 μeV splitting for the DX states. With a roughly one-thousand fold difference in the recombination probability of the DX and IX states, one might naively say this energy splitting is in the nanoeV range.

fuel to the debate over whether or not the darkening in our system has some origin in a dark BEC, and just because this splitting is small does not mean that the lowest state is not dark, for this reason or another. Hence, it is left as an open possibility.

1.6.3 IX BEC: Signs from Luminescence

The typical behaviors signaling the onset of BEC are also presumed to occur in the CQW system. The onset of BEC is usually accompanied by spatial and spectral narrowing, and there is necessarily some enhancement of the spatial coherence compared to the thermal length scale of the thermal de Broglie wavelength. All of these effects will be modified by the strong interparticle repulsion in this system. Of course, if the lowest energy state of the excitonic system is a dark state, none of these effects will be directly observable.

In a trapped population, condensation generally causes a spatial narrowing of the density profile, associated with high occupation of the lowest energy trap state. This is particularly dramatic in trapped atomic gases – in the condensed state, upon removing the trapping potential, the atoms have a momentum distribution that is the Fourier transform of the trap's ground state. In these cases of particles with very weak interactions, the densities above and below the transition can be well described by the occupation of the single-particle energy states that are largely unchanged by the presence of other particles. In the IX case, the trap potential is significantly flattened by the presence of other IXs. Accordingly, a BEC will certainly not occur in the single-particle ground state of the applied harmonic potential. The fact that our typical experimental density profiles reflect a length scale 100 times larger than the intrinsic trap ground state (≈ 1 μm in a trap with harmonic constant $\alpha = 50$ eV/cm) reflects that the appropriate length scale is not defined solely by the trap potential and particle mass. Instead, at low temperature the appropriate length scale is $\sqrt{\frac{2\gamma n(0)}{\alpha}}$, which is the radius of the density profile, n(r), that makes the local energy (γn(r) + $\frac{1}{2}\alpha r^2$) constant, the Thomas-Fermi profile. The density profile above the transition can be described in a similar way, with the profile determined by the interparticle interaction strength and the trap shape, and the primary difference will be thermal excitation of states that extend to a larger radius. Naively, then, we might say that the change in the density

profile will be small, accompanied only by a sharpening of the periphery of the density profile. However, there should be a more dramatic spatial narrowing since the average interparticle interaction strength will be reduced with BEC onset – as noted in Section 1.6 in regard to BEC fragmentation, there is an exchange energy savings from having a large number of repulsive bosons in a single state. This will decrease the radius of the Thomas-Fermi profile, causing a significant spatial narrowing accompanying BEC.

In addition, if the population may luminescence, as in the excitonic case or the related exciton-polariton case, the spectral linewidth is expected to narrow with the onset of phase coherence. The CQW linewidth is determined by the inhomogeneous broadening from the QW disorder potential as well as homogeneous broadening, primarily from the IX-IX scattering. Zimmermann [86] has treated both of these effects with increasing IX density using a dynamical T-matrix to account for multiple XX scattering events in the IX self energy. He has determine the linewidth and angular emission profile of the emission (essentially determining the in-plane momentum occupation) up to densities just below the transition. That analysis showed that the inhomogeneous linewidth decreases with increasing density, as the disorder potential becomes screened by the presence of many IXs. The homogeneous linewidth begins to decrease as the condensation transition is approached and the population becomes increasingly coherent. Additionally, the occupation of in-plane momentum states was shown to become narrower, with more excitons occupying k_{cm} states within the light-cone for radiation. This should lead to an increase in the overall radiative rate, if the transition occurs at a temperature where there is typically a large population with too much in-plane momentum to allow recombination.

The precise density and temperature at which to expect these signs is not well established, due to the strong interactions. In order to begin experiments, it is desirable to have a rough guideline for when the BEC transition should occur. This can be found in the most qualitative criterion for BEC, that there should be significant wavefunction overlap. If we simply ask what density is required for $n\lambda^2 \sim 1$, we might get an idea of the lower limit on the density required for degeneracy. This criteria may seem misguided in light of the fact that there is not necessarily a monotonic dependence of the critical density on temperature. For example, over the accessible condensate range in LHe, the critical density actually drops

with increasing temperature. However, we still expect this to be a very rough lower bound on the density, as the transition in LHe always occurs with a density larger than $n_{3D}\lambda^3$. The range of possible density and temperature for LHe BEC is rather small, and is centered around a mass density ≈ 0.16 g/cc at 2 K [22], making $n_{3D}\lambda^3 \approx 6$ (about double the ideal gas prediction of 2.6). It must always be larger than this ideal gas prediction because the repulsive interactions have the effect of decreasing the wavefunction overlap, suppressing condensation. For indirect excitons at 2 Kelvin, the criteria $n\lambda^2 > 1$, tells us that below a density of 7×10^9 cm^{-2}, no BEC transition can occur[23]. While we cannot say at what density we might see condensation, we can certainly say it will not be below this density. In terms of the best temperature to seek the transition, lower temperature is not necessarily always best if one is seeking a large-scale BEC. At very low temperatures, the excitons can become localized in disorder minima from well-width fluctuations. As stated above, this disorder potential can be screened by high density, but in general it will hinder spatial equilibration in a large trapping potential if the temperature is far lower than the scale of the disorder potential. The inhomogeneous linewidth of the exciton states in our system is roughly 0.5 meV, suggesting that temperatures in the range of a few Kelvin are the lower limit. It was observed by Voros et al. in this system that the spatial density profile, which should be determined by the trap potential and the temperature in equilibrium, never reached a size consistent with temperatures lower than 5 K. While this could have been due to some additional heating source, it is likely that diffusion slows down considerably after the high density excitation phase due to localization in disorder minima. Our experiments include sample temperatures below 5 K, and we simply allow for the possibility that at low temperature the population may not be quite as dense as predicted by the temperature.

[23]This corresponds to a just perceptible blue-shift of 140 μeV using the modified capacitor formula of Eq. 1.14

2.0 INTERACTION OF INDIRECT EXCITONS WITH APPLIED FIELDS

The role of a DC electric field in the IX system has already been considered, since its presence is fundamental to the formation of IXs. Now, the interactions of the IX system with additional fields relevant to the presented experiments are considered. First, the effect of a localized strain on the IX states is examined in Section 2.1, where it is shown that large-scale traps may be created. In addition, it is demonstrated that this applied force will mix valence-band states that are typically well-separated in energy. Next, it is shown in Section 2.2 that an in-plane magnetic field has the effect of mixing dark and bright exciton states.

All measurements in this study are intensity measurements of the exciton recombination luminescence resulting from optical excitation. This process of excitation and luminescence is reviewed in Section 2.3. The linear polarization created by valence-band mixing is described in Section 2.3.1.

2.1 STRAIN TRAPS AND STRAIN-INDUCED MIXING

Strain traps can be used to create roughly harmonic trap potentials. Past work has shown that these strain-based traps avoid the trap-driven ionization and spatially-varying oscillator strength that exists in electrostatic traps. An electrostatic trap is created by creating a spatially-varying growth-direction electric field, with the largest magnitude field at trap-center. By the Stark effect, the IX energy is lowest in the region of highest field at the center of the trap. This has the interesting feature of creating a deep trap for IXs and a negligible shallow trap for DXs. However, if the growth-direction field is varied over a very short

length scale, the in-plane electric field may be able to ionize the excitons. In addition, since the electron-hole overlap is varying strongly over the trap, the recombination probability is varying over the trap, with the lowest recombination probability at trap center. Prior to this study, it was believed that the strain-trapping technique was free from the complication of spatially-varying oscillator strength. So, for this reason, along with the ability to easily create harmonic trap potentials, strain-trapping was used in this study.

For the purposes of this project, the two important effects of applying strain to the crystal are that an expansion of the crystal (increasing the volume of the unit cell) lowers the exciton energy and that shear strains will cause mixing of valence-band states. In this work, we exploit the former to create regions of localized expansion in order to create exciton traps. This is achieved by simply pressing a sharpened pin against the wafer, creating a region of expansion underneath the pin, if the opposite side is free to flex under the applied force. The non-uniform stress creates not only this region of expansion, but also shear strains in the regions around the pin. Heretofore, the valence-band mixing due to this shear strain has been neglected in studies employing this technique in GaAs quantum wells, due to the large zero-strain energy separation of the HH and LH states caused by the QW confinement. Under larger hydrostatic expansion, however, this LH-HH energy separation shrinks, and even small shear strain terms may cause valence-band mixing, affecting the polarization and, potentially, the brightness profiles of the photoluminescence from exciton annihilation.

If we keep only the terms linear in the strain, the effect of strain on the conduction-band is due completely to the change in the volume of the unit cell, and the strain is simply responsible for an energy shift,

$$\Delta E_c(\epsilon) = a_c \left(\epsilon_{xx} + \epsilon_{yy} + \epsilon_{zz}\right), \tag{2.1}$$

where a_c is the deformation potential for hydrostatic strain on the conduction-band. The effect of strain on the valence-band states is more complex, and it is accounted for in the Pikus-Bir Hamiltonian. This has an identical form to the Luttinger-Kohn Hamiltonian of

Eq. (1.2), replacing momenta with strain terms [15]:

$$H_{P-B} = \begin{pmatrix} P_\epsilon + Q_\epsilon & -S_\epsilon & R_\epsilon & 0 \\ -S_\epsilon^\dagger & P_\epsilon - Q_\epsilon & 0 & R_\epsilon \\ R_\epsilon^\dagger & 0 & P_\epsilon - Q_\epsilon & S_\epsilon \\ 0 & R_\epsilon^\dagger & S_\epsilon^\dagger & P_\epsilon + Q_\epsilon \end{pmatrix}, \tag{2.2}$$

$$P_\epsilon = -a_v \left(\epsilon_{xx} + \epsilon_{yy} + \epsilon_{zz}\right), \quad Q_\epsilon = -\frac{b}{2}\left(\epsilon_{xx} + \epsilon_{yy} - 2\epsilon_{zz}\right), \tag{2.3a}$$

$$R_\epsilon = \frac{\sqrt{3}b}{2}(\epsilon_{xx} - \epsilon_{yy}) - id\epsilon_{xy}, \quad S_\epsilon = -d(\epsilon_{xz} - i\epsilon_{yz}), \tag{2.3b}$$

where a_v, b, d are the deformation potentials for GaAs. The strain ϵ_{ij} is defined as the displacement of the $\hat{x}_i$ unit vector in the $\hat{x}_j$ direction,

$$\vec{x}_i = \sum_j (\epsilon_{ij} + \delta_{ij})\hat{x}_j. \tag{2.4}$$

In separating the strain dependence of these matrix elements from the momentum of a given state, the assumption has already been made that the strain is varying slowly with respect to the unit cell size. Thus, it is legitimate to determine the strain at a single point in the crystal and find the eigenvectors of the Pikus-Bir Hamiltonian to determine the local eigenstates.

For the purposes of predicting the local eigenvectors, we have used the results of an ANSYS finite-element analysis of the strain. These strain simulations are primarily the work of collaborators within this laboratory, specifically Bryan Nelsen, Ryan Balili, and Jeff Wuenschell. A simple representation of the strain geometry is displayed in Figure 5. In these calculations, a 125 μm-thick GaAs wafer is positioned over a 2 mm diameter hole, allowing it to flex when force is applied from above. This situation mirrors the stressor mechanism in our experimental work. In our structures, the quantum wells reside within 1 μm from the freely-flexing side of the wafer. Maps of the strain (ϵ_{xx}, ϵ_{yy}, ϵ_{zz}, ϵ_{xy}) in this region near the free surface, predicted by applying 1 N over a 50 μm diameter region, are shown in Figure 6. The maps of the diagonal strain components show that the expansion is localized under the applied force at (0,0). The off-diagonal strain due to the applied force, ϵ_{xy}, is zero exactly

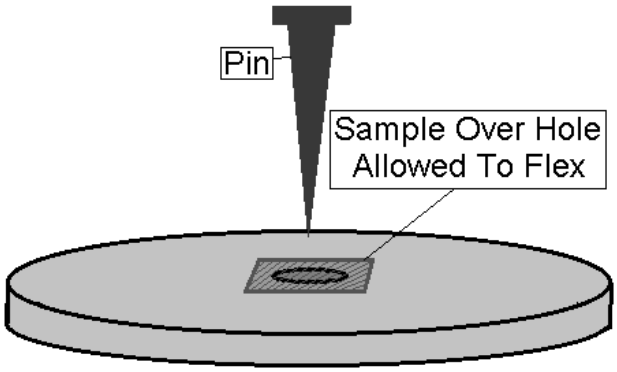

Figure 5: Sample-straining geometry. The sample sits over a hole in the mounting plate, and a sharpened pin applies a localized force on the substrate from above. The hole allows the sample to flex downward under the force, causing expansion of the crystal on the lower side, where the wells reside.

under the pin, increases to 2.5×10^{-4} at a radius of about 125 μm[1], after which it remains roughly constant. The ϵ_{xz} and ϵ_{yz} strain are not shown because, due to the proximity of the quantum wells to the lower surface, the boundary condition requiring zero stress in the z direction at this surface causes all of these terms to vanish. These same ANSYS results have been used to predict the linear polarization splitting of trapped microcavity polaritons in a similar structure [10] and were very successful in that endeavor.

Figure 7 plots the energy eigenvalues predicted for the HH and LH DX states resulting from the calculated strain. The deformation potentials were taken from Chuang [15] as a_c = -7.17, a_v = 1.16, b = -1.7, and d = -4.55. First, focusing on the spatial profiles of the individual states' energies, the strain creates large-scale traps that are energetically deep with respect to k_B at LHe temperatures. Comparing the two valence-band states, the LH exciton energy shifts much more quickly with strain than the HH state. This is primarily due to the large value of the shear term, Q_ϵ, which is much larger than the hydrostatic strain,

[1]It is not a coincidence that this distance is roughly the thickness of the sample. While the size of the strain profile is determined by the stressor apparatus on the side of the wafer where the force is applied, the quantum wells reside on the opposite side of the sample. The strain profile is relaxed over the thickness of the sample, and as long as the thickness is larger than the radius of the stressor, the thickness is the length scale determining the trap shape. Thus, sharpening the pin much finer than the wafer thickness is fruitless.

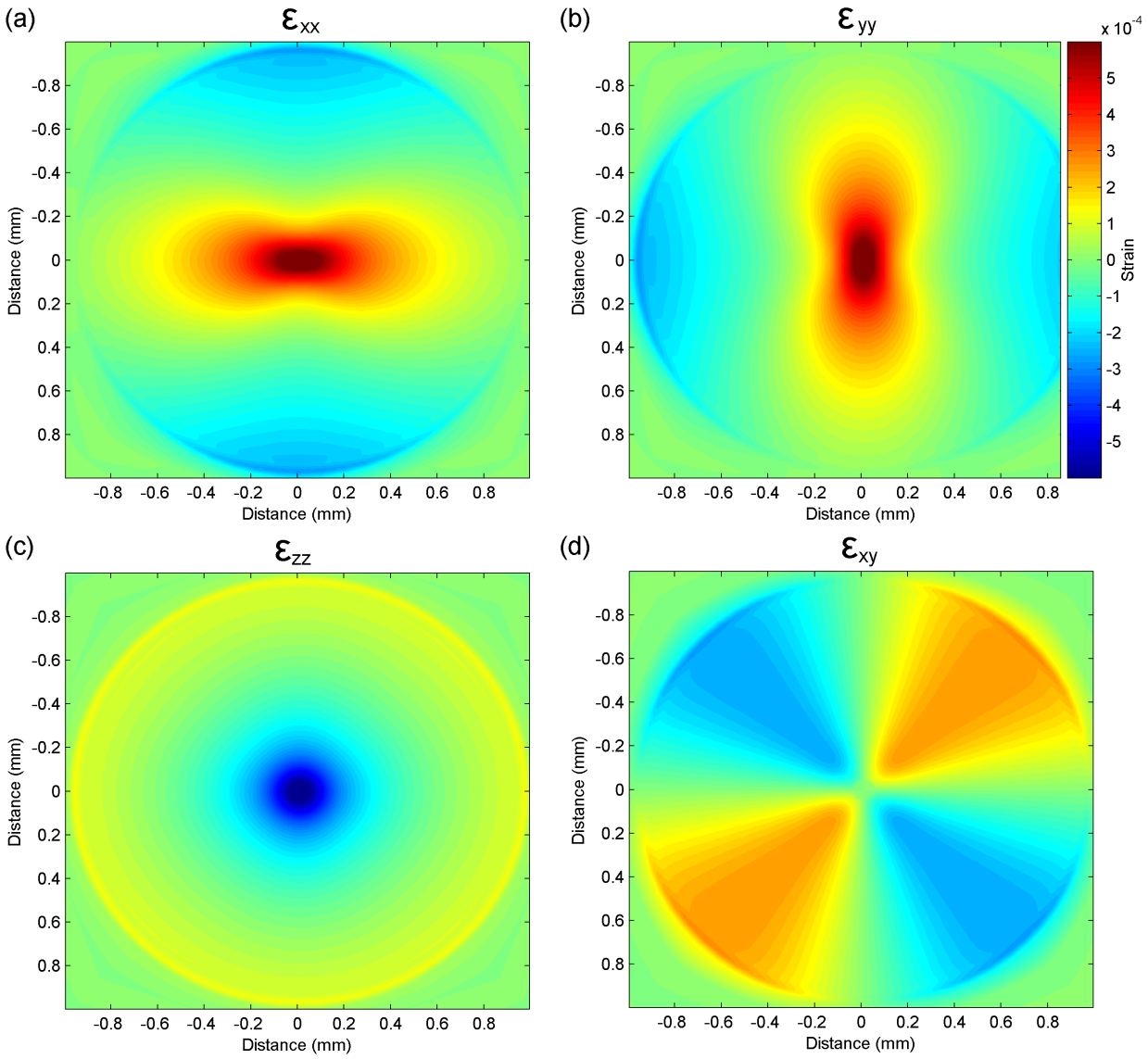

Figure 6: Numerical strain calculation from an applied force of 1 N. The $\hat{x}$ and $\hat{y}$ directions (horizontal and vertical in these plots) correspond to [100] and [010], and $\hat{z}$ is the growth direction [001].

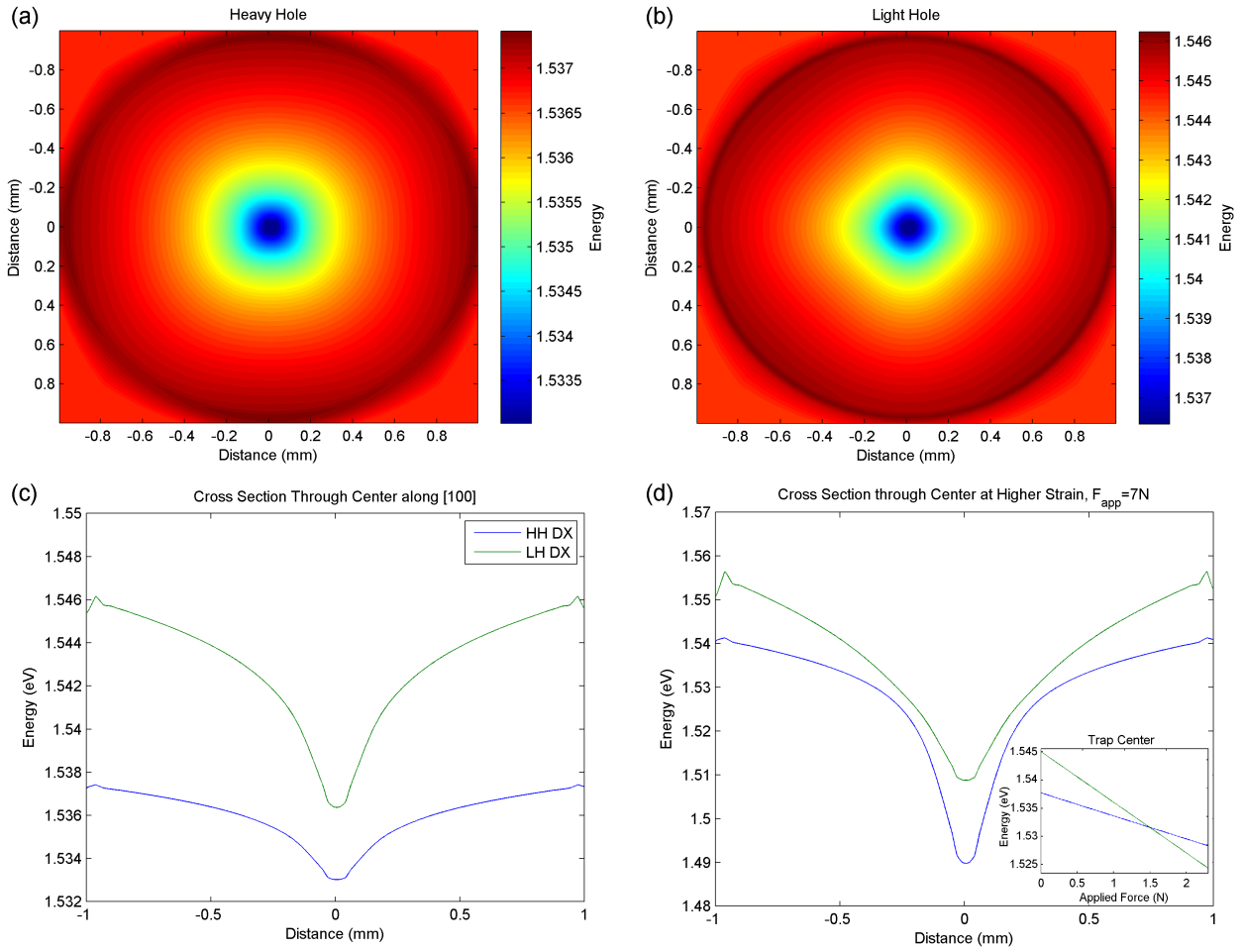

Figure 7: Spatial maps of the DX energy due to the strain from Figure 6, for F_{app}=1 N, for the lowest energy state that is mostly HH-like, (a), and the next highest state that is mostly LH-like, (b). Plot (c) shows a cross-section of this energy profile through the center of the trap for each of these levels, demonstrating that they approach each other in energy with increasing strain. Plot (d) shows the effect of higher strain, for F_{app}=7 N, where the HH and LH DX lines have crossed; the lower energy line is HH-like at the edge and LH-like at the center. The inset plots the LH and HH energies at trap center for increasing force, with no LH/HH mixing terms, in order to demonstrate the crossing.

P_ϵ, because the lattice is being compressed in the z-direction while expanding in x,y. Due to the opposite signs of a_v and b, the LH state, having diagonal element $P_\epsilon - Q_\epsilon$ will be shifted by a much larger degree. From the strains plotted in Figure 6, at the center of the trap, the Q_ϵ term is roughly a factor of 5 larger than P_ϵ. Thus, with increasing applied force to the sample, the LH and HH DX states will cross.

This can be seen in Figure 7(d), plotting a cross-section of the eigenvector energies when a much larger force of 7 N is applied to the wafer. This applied strain is far beyond that required to cause the crossing of LH and HH states, and, at the center of the trap, the LH and HH states have switched places. Now, the lowest energy state at trap center is the LH DX state. The anti-crossing away from the center is caused by the mixing from off-diagonal strain components[2], and since there is no LH/HH mixing terms in this Hamiltonian at the exact trap center, the states will simply cross at this point. This is shown in the inset to Figure 7(d), where the energy at trap center is plotted, and the LH/HH crossing is demonstrated clearly. The strain at which this crossing occurs is determined by, apart from the deformation potential values, the initial separation of the LH and HH DX states due to quantum confinement. Therefore, more force should be required to cause a crossing in the case of narrower wells, where the confinement splitting is larger.

While these simulations are actually predicting the DX energies, the energies of the interwell states should be modified in the same way. The deformation potentials will be the same for DX and IX states as well, and the IX states will also cross with increasing force. However, the strain to cause this crossing may differ between the two cases. In particular, the confinement energy splitting between the LH IX and HH IX states may be different. In addition, we might expect that the crossing strain is slightly variable with applied voltage, since the LH and HH IX states have marginally different growth-direction dipole moments, as shown in Figure 3(a).

Since the LH state shifts more strongly with strain, the LH traps are steeper than those of the HH state. This can be seen in the energy profiles in Figures 7(c-d), but it can also be demonstrated quantitatively. Figure 8 fits the ground state trap to a quadratic potential,

[2]The mixing between these valence-band states will cause a linear polarization of the luminescence. For a calculation of this effect, see Section 2.3.1.

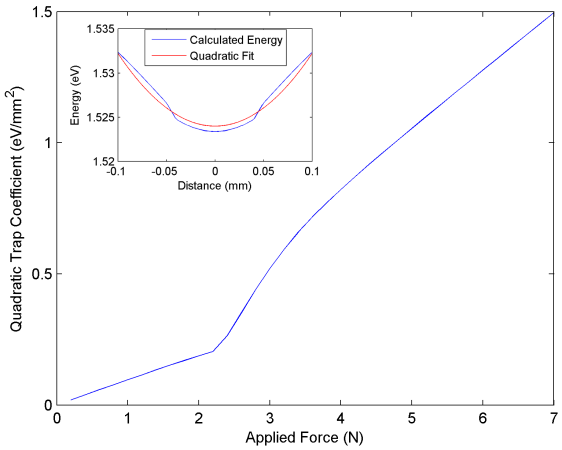

Figure 8: Quadratic trap coefficient vs force applied to sample. With increasing force, the in-plane confinement becomes sharper. The transition in the slope of this curve displays the transition of the ground state from HH to LH at the center of the trap. The inset displays an example fit at F = 4 N, where it is clear that the quadratic fit is only approximate. Within 50 μm of the trap, a remnant of the stressor exists, and at distances greater than about 100 μm from the center, the trap begins to flatten, as can be seen in Figure 7.

within a region 50 μm from trap center, as a function of force applied to the sample. At the lowest forces, the range of forces for most of these experiments, the confinement potential sharpens gradually with increasing force. At the force where the states cross, the confinement potential quickly becomes sharper. Continuing to increase the force causes the harmonic trap coefficient to grow at a rate about 2.5 times faster than the low stress, HH case.

While this section is emphasizing the valence-band mixing caused by strain, it should be mentioned that a strong growth-direction field is actually sufficient to cause mixing of the valence-band states in our structure, even without any strain. This effect has been previously studied [33, 35] and referred to as the Quantum-Confined Pockels effect, due to the resulting polarization anisotropy of the absorption. The necessary condition for mixing $j_z = \pm\frac{3}{2}$ states with $j_z = \pm\frac{1}{2}$ states is to break the symmetry between the [110] and [1$\bar{1}$0] directions (two orthogonal directions in the quantum well plane)[3]. In the D_{2d} symmetry

[3]This mixing has similarly been demonstrated in asymmetric quantum wells (high barrier/ well / low barrier) with no applied electric field [32].

group[4], these directions are related only under the improper rotation, $\bar{3}$, about the growth-direction[5]. If a growth-direction field is added, there are no longer any symmetry operations of the Hamiltonian which relate these two states, and mixing of $j_z = \pm\frac{3}{2}$ and $j_z = \pm\frac{1}{2}$ becomes allowed. In a single 10 nm, GaAs-$Al_{0.3}Ga_{0.7}As$ well, in a 50 kV/cm field, Krebs et al. [33] predict a polarization anisotropy of 1.4%, taking into account the initial LH-HH energy splitting, the matrix element between LH and HH due to the interface, and the magnitude of the valence-band envelope function at the interface. In relation to our experiments, while the system is similar, all of these quantities will be very different: 1) the LH-HH splitting may be much smaller due to strain, 2) the matrix element will likely be larger due to the larger Al concentration, and 3) the envelope function dependence is far more complicated but will likely contribute a similar weight overall[6]. The first of these changes will cause the largest contribution. If the LH-HH splitting goes to zero, any amount of splitting may cause a very large linear polarization of the ground state. Therefore, we expect that at high strain, there may be a large degree of LH-HH mixing that is electric-field dependent. Furthermore, this interplay of strain and electric field to cause much larger polarization anisotropy suggests directions for future work, e.g. the application of a static hydrostatic expansion to quantum wells to enhance this field-tunable absorption anisotropy (and the corresponding birefringence).

2.2 EFFECTS IN A WEAK IN-PLANE MAGNETIC FIELD

Since dark exciton states are prevented by symmetry from creating luminescence, there is no direct indication of the density of the dark exciton population in the luminescence signal. It is typically assumed, due to the extremely small exchange splitting between the dark and

[4]The symmetry group for bulk GaAs is the tetrahedral group T_d. A single interface of GaAs with AlAs, or AlGaAs, has the orthorhombic C_{2v} symmetry, but a symmetric pair of these interfaces can have the higher tetragonal D_{2d} symmetry. [43, 83]

[5]This denotes the operation of rotation by 120 degrees, in this case around the growth direction, and reflection through the symmetry point. This rotation generates the symmetry group S_3.

[6]The outermost interfaces of our double quantum well structure will have a smaller contribution due to the higher Al concentration in our barriers and the presence of opposite charges in the opposing well. On the interior interfaces, the higher Al concentration will similarly suppress the envelope function, but the interwell excitonic effect will augment it.

bright states and the relatively fast spin equilibration, as measured in DX states, that the dark state density will be always equal to that of the bright states. However, in order to explain the darkening at trap center observed in these experiments, one might consider a spatial separation of the dark and bright populations, where exclusively dark excitons are present at trap center. If the symmetry that preserves the dark nature of these excitons is broken, dark excitons might be made slightly bright, and the density profile of these excitons might be observed rather than simply inferred. To this end, a magnetic field in the plane of the quantum well is used in experiments here attempting to clarify the role of dark excitons in the intensity patterning phenomenon.

Adding a magnetic field to the system modifies the energy landscape and character of the exciton states in several ways. First, ignoring the multiplet nature of the bands and considering only the effect on free carriers with an isotropic effective mass[7], an in-plane magnetic field will shift the band dispersion parabola in momentum, moving the minimum away from the Γ-point, and, separately, it provides a weak diamagnetic shift. Introducing a vector potential $\vec{A} = zB_x\hat{y}$ into the canonical momentum, $\hat{p} = -i\hbar\vec{\nabla} + \frac{e}{c}\vec{A}$, the Hamiltonian [83, 74], to second order in the field, is given by:

$$H = \frac{\hbar^2 k_x^2}{2m_{eff}} + \frac{\hbar^2(k_y + \frac{e}{\hbar}B_x\langle z\rangle)^2}{2m_{eff}} + \frac{e^2B_x^2}{2m_{eff}}(\langle z^2\rangle - \langle z\rangle^2) + \frac{e^2\hbar^2k_y^2B_x^2}{m_{eff}}\sum_i \frac{|\langle i|z|j\rangle|^2}{E_j - E_i}, \qquad (2.5)$$

where a $\langle z\rangle^2$ term has been substituted into the second term rather than the natural $\langle z^2\rangle$ term, in order to properly complete the square. Choosing this form for the Hamiltonian (and this particular gauge) allows the previous treatment of the problem, i.e. the separation of the wavefunction into an envelope function and in-plane component, to remain valid and highlights the modifications due to the new field. The second term shows that there is a dispersion minimum (or maximum in the valence-band case) for nonzero momentum when $\langle z\rangle$ does not vanish, e.g. in asymmetrically-doped wells, biased wells, or in the CQW case. The third term exists due to the substitution into the second term and yields a diamagnetic

[7] Of course, this is the scenario when in bulk one would find the onset of Landau levels. Here, the carriers are prohibited from moving in the growth direction due to the confinement potential, so the typical Landau orbits will not be available. However, the shift of the dispersion minima away from the Γ-point and the increasing effective mass in the direction perpendicular to the field are both features reminiscent of the Landau orbit case [83].

shift of the carrier energies. The final term causes an increase in the effective mass in the $\hat{x}$ direction.

These effects transfer to the IX states as well. For IXs with a distance d between the QW centers in the growth direction, the band edges of the conduction-band and valence-band are both shifted in momentum by $\frac{eB_x d}{2\hbar}$. So, the band gap is still vertical but now occurs at finite in-plane momentum. Excitons in thermal equilibrium will preferentially occupy finite momentum states that, if the field is large enough, may be outside of the light cone for recombination. At low temperature, the light cone becomes depleted of carriers and the radiative lifetime should lengthen considerably. This effect has been demonstrated by Butov et al [12], where the lifetime has been shown to increase dramatically with increasing magnetic field. At a bath temperature of 1.5 K, the recombination rate is halved by the application of about 4 Tesla in the QW plane[8]. The diamagnetic shift of the carriers translates into a blue-shift of the excitons due to the inverse mass dependence of this term. The lighter conduction-band states are blue-shifted more than the valence-band states, so that the band gap grows quadratically with the applied magnetic field. However, while the diamagnetic shift of the exciton states does exist, it is rather small. Since PL experiments are concerned with the energy of excitons that are allowed to recombine, the shift of the dispersion minimum away from the center of the radiative zone actually contributes a much larger energy to the observed energy than does the diamagnetic shift of the bands. This shift is also quadratic in B, and this should be the dominant observed shift of the exciton PL energy for this field orientation[9].

On the other hand, the detailed interactions caused by this in-plane field between the

[8]This is also not a negligible effect in biased, single wells. Winkler [83] has calculated numerically, using the extended Kane model rather than this simplified band picture, the effect of a 1 T in-plane magnetic field on the conduction-band in the presence of a 20 kV/cm electric field. The minimum of the conduction-bands in the calculated dispersions occurs at just under 10^5 cm^{-1}, though varying slightly for different in-plane directions ([110] vs [1$\bar{1}$0]) and spin orientations. This is roughly one-third of the maximum in-plane momentum within the radiative zone.

[9]If the field were oriented in the growth-direction, the dominant shift of the IX states would actually be due to a magnetoresistive effect. This shift was observed experimentally for IX states by Negoita et al [51] and Krivolapchuk et al [82], and, due to the large magnitude of this effect, it has been proposed as a measurement technique for optical detection of magnetic fields [19]. It is a specific case of a general phenomenon seen when transporting carriers through layered material when the tunneling is dominated by interface defects. The growth-direction field causes an in-plane magnetoresistance and making motion between laterally-spaced interface defects more difficult.

angular momentum states at the band edge are of more fundamental importance to this work. Winkler [83] has compiled the effects of an arbitrarily-oriented magnetic field on the valence and conduction-band structure into an extended Kane model Hamiltonian. The extended Kane model considers a 14×14 Hamiltonian that includes the 4 Γ_{8v} (in T_d) HH/LH states, the 2 Γ_{7v} split-off states, the 2 Γ_{6c} conduction-band edge states, and 6 Γ_{8c} and Γ_{7c} higher lying conduction-band states[10]. In this document, the valence-band and conduction-band have so far been treated separately. In the Pikus-Bir Hamiltonian, accounting for strain, and the Luttinger Hamiltonian, accounting for the k·p interaction, a diagonal 2×2 matrix was considered for the conduction-band and a 4×4 matrix included the effects on the LH/HH states, where the remote split-off band is neglected. Following this trend, the blocks of this magnetic Hamiltonian dealing with the HH/LH states will be isolated and analyzed separately, and likewise for the conduction-band edge states. The LH/HH valence-band block of this Hamiltonian takes the form (to first order in B and neglecting a term with a prefactor that is orders of magnitude smaller than κ), $H^v_{mag} = -2\mu_B\kappa\vec{J}\cdot\vec{B}$, where the $\vec{J}$ are angular momentum matrices and κ is the effective g-factor for these valence-band states. For a magnetic field in the x direction, this takes form:

$$H^v_{mag} = \kappa\mu_B \begin{pmatrix} 0 & \sqrt{3}B_x & 0 & 0 \\ \sqrt{3}B_x & 0 & B_x & 0 \\ 0 & B_x & 0 & \sqrt{3}B_x \\ 0 & 0 & \sqrt{3}B_x & 0 \end{pmatrix}. \tag{2.6}$$

The mixing induced by this in-plane field is between states which differ by 1 in the z-component of their angular momentum. So, the two LH states are mixed together and the LH and HH states with the same angular momentum orientation are also mixed. This mixing alone will lead to mixing of dark and bright exciton states of both HH and LH varieties. Consider a bright LH exciton composed of a spin up electron and a $J_z = +\frac{1}{2}$ hole. With this interaction, the valence-band state now also contains a $J_z = +\frac{3}{2}$ heavy-hole component, so that the exciton is mixed with a state with $J_z = +2$. This state is only achievable from a state with total angular momentum $|\vec{J}| = 2$, so the previously bright state must now contain

[10]The Kane model considers only 8 states: the HH/LH states, the conduction-band edge, and the split-off band.

a dark component. The bright/dark exciton states are additionally mixed by the off-diagonal terms in the conduction-band Hamiltonian, which similarly reads:

$$H^{c}_{mag} = \frac{g^{\star}\mu_B}{2}\begin{pmatrix} 0 & B_x \\ B_x & 0 \end{pmatrix}, \tag{2.7}$$

where $g^{\star}$ is the effective g-factor for the conduction-band. In GaAs, the measured values for κ and $g^{\star}$ are 1.2 and -0.44, respectively[11] [83]. With these values, the off-diagonal terms between the LH and HH states in the valence-band are (0.12 meV/T)×B, and between the conduction-band states the mixing term is (0.013 meV/T)×B. With the expected splitting of the bright/dark states measured to be approximately 40μeV in the DX case and significantly lower than this in the IX case, due to the drastically reduced electron-hole overlap, a relatively small in-plane magnetic field is expected to be sufficient to mix these states.

Overall, the expected response of the IX system to an in-plane magnetic field is to show a small blue-shift in energy of the PL, a possible lengthening of the lifetime for IX recombination, and a possible brightening of dark states. It should be noted that the whole system should not brighten due to this mixing, unless the dark states are much more heavily populated than the bright states. With the mixing of the bright/dark states, the oscillator strength is simply traded between the states, so that if the states are equally populated the system should have the same radiative rate (apart from the potential lifetime change due to the offset of the dispersion minimum).

2.3 EXCITATION AND LUMINESCENCE

In these experiments, the exciton life cycle is dominated by optical transitions, tunneling, and energy relaxation. Excitation of IXs begins by photon absorption in a single well, either resonantly into a DX state or into the free-carrier continuum. One of the carriers then must tunnel into the opposing well to generate an IX. Finally, in order to recombine, the carriers must have a relatively low kinetic energy, within the photon energy-momentum light-cone.

[11] These values for κ and $g^{\star}$ take into account the effect of remote bands from the extended Kane model, so the reduction of accuracy in going from the 14×14 model to this 4×4 model is minimized.

The transfer of charge from one well to the other may occur through tunneling either of electrons or holes. In fact, since we are pumping both wells and expecting a final state with total charge separation, we are relying on the fact that both processes will occur. It was initially believed that due to the smaller electron mass, the fastest charge transfer mechanism was that of electron tunneling. However, the rates of electron and hole tunneling have been shown to be dependent on applied DC electric field, as the field shifts the energies of carriers and causes interwell resonances. In fact, the hole states have been predicted to have a faster tunneling rate over a wide range of electric fields [60, 59]. The predicted minimum and maximum tunneling lifetimes, as the field is varied, in the studies of Ferreira et al. [60, 59] are 1 ps to 1 ns, and Alexandrou et al. [3] measure the high end of tunneling times in a structure similar to ours (though with narrower wells) at 16 kV/cm to be 300 ps, with rather large error bars. From this, we can essentially only say that the rate of charge seperation may be on a similar scale with the DX recombination rate and that the two processes will be in competition. This will makes the DX luminescence visible, as some DXs are able to recombine before becoming indirect excitons.

The cooling of charge carriers occurs by the emission of phonons. At carrier energies larger than the LO phonon energy (36 meV), the emission of LO phonons dominates the thermalization process. In fact, LO phonons have been shown to dominate cooling in GaAs QWs down to a lattice temperature of about 35 K, despite the fact that this temperature corresponds to a much lower energy scale[12] [50]. However, since this system requires cooling down to around 2 K, the cooling must occur much more slowly by LA phonons. On the positive side, the relaxation of momentum conservation in the growth direction allows the excitons to cool much faster by this LA phonon process than it would proceed in bulk[13] [26].

Similarly, in bulk, the strict conditions of energy and momentum conservation drastically

[12] After the small number of high-energy states cool by this mechanism, the fast elastic processes of Auger scattering, impurity scattering, and carrier-carrier scattering quickly reestablish a thermal distribution, replenishing these states and allowing the process to continue.

[13] The usual way to picture the allowed interactions is to plot the exciton dispersion and phonon dispersion on the same axes, with the linear phonon dispersion line beginning at the initial exciton state, since it represents the transferred momentum between final and initial exciton states. In bulk the allowed transitions will connect the final state and initial state by this line with slope $\hbar v_s$. In a quantum well, relaxing the condition of matching k_z allows one to also couple final and initial exciton states connected by any line *steeper* than the phonon dispersion, as any energy $\hbar v_s k_z$ may be added to compensate the difference.

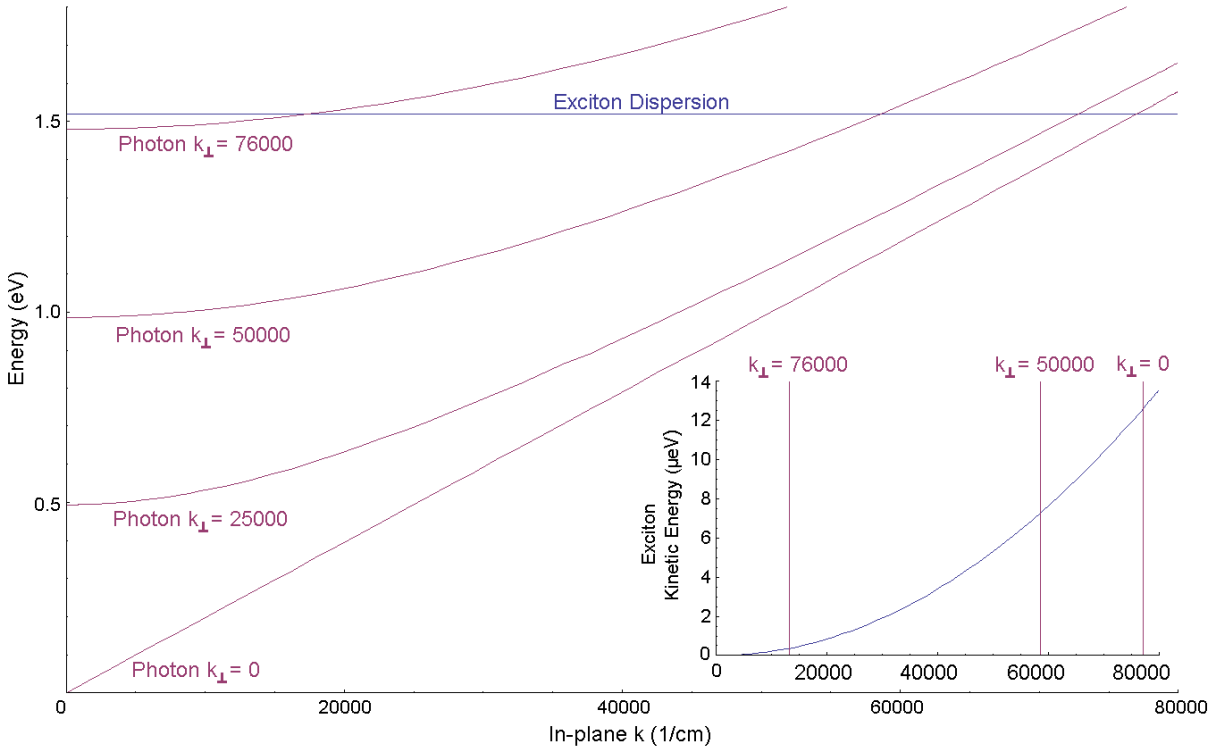

Figure 9: Dispersion relations for quantum well excitons (Blue) and photons external to the sample (Purple). The intersection marks in-plane momenta at which energy may be conserved. The in-plane momentum must be preserved between the exciton and photon. However, the photon's momentum in the growth-direction may vary. Four curves at varying growth-direction photon momentum are plotted. The inset shows the intersections on a different energy scale, the exciton kinetic energy, after removing the zero-momentum exciton energy.

limits the electron to photon conversion. Only excitons with a particular total momentum are able to meet these criteria, specifically:

$$E_0 + \frac{\hbar k^2}{2m} = \hbar c_n k. \tag{2.8}$$

However, in a quantum well, the growth-direction confinement provides a relaxation of momentum conservation, allowing variation of the photon momentum in the growth direction. The in-plane momentum must still be equal between the exciton and emitted photon. This situation is demonstrated in Figure 9, plotting the dispersion curves for quantum well excitons and photons external to the sample versus in-plane momentum, with E_0=1.52 eV and m=0.18m_0. Photon dispersions with four different growth-direction momenta are plotted, showing that the intersection points moves to smaller in-plane momentum for increasing momentum in the growth direction. The maximum in-plane momentum allowing recombination and emission out of the sample occurs with zero photon momentum in the growth direction, corresponding to an in-plane momentum of 77000 cm^{-1}. The inset shows the intersections on a different energy scale, the exciton kinetic energy, after removing the zero-momentum exciton energy. The exciton kinetic energy corresponding to the maximum in-plane momentum is approximately 13 μeV. If one is interested in the maximum kinetic energy at which the excitons are able to interact with light within the sample, this can also be calculated with $n = 3.58$. This corresponds to an exciton kinetic energy of about 161 μeV. Since the energy scale for emission out of the sample corresponds to a temperature of only 0.15 K, it is clear that at elevated temperature only a very small fraction of the exciton population will have a small enough kinetic energy to produce a photon that will be emitted from the sample. For this reason, the emission rate of a population is decreased with increasing temperature.

The maximum kinetic energy of the measured excitons is even lower than the 13 μeV allowed for emission from the sample. For example, if one limits the collection angle in air to 7 degrees from the normal (a 1" diameter lens at 4 inches), this calculation suggests that the maximum in-plane kinetic energy of the excitons represented is only about 0.2 μeV. This demonstrates that the measured spectral lineshape of exciton emission is negligibly effected by the exciton momentum. The measured spectroscopic lineshape will be dominated by homogeneous broadening at high exciton density and by inhomogeneous broadening due to

disorder at low density. Voros [78] demonstrated that we can expect the inhomogeneous broadening to be roughly 500 μeV and that the homogeneous broadening will monotonically increase with exciton density. The crossover to the regime of dominating homogeneous broadening is temperature dependent, and in [78] it begins, at 3 K, at a blue shift of roughly 0.5 meV.

2.3.1 Polarization

The linear polarization of the photoluminescence can be used as a measure of the HH-LH mixing. Predicting the linear polarization of the ground state requires finding the eigenvectors of the sum of the valence-band Hamiltonians from momentum-induced mixing (the Luttinger-Kohn Hamiltonian, Eq 1.2) and strain-induced mixing (the Pikus-Bir Hamiltonian, Eq 2.2)[14],

$$H_{L-K} = \begin{pmatrix} P+Q+P_\epsilon+Q_\epsilon & -S-S_\epsilon & R+R_\epsilon & 0 \\ -S^\dagger-S_\epsilon^\dagger & P-Q+P_\epsilon-Q_\epsilon & 0 & R+R_\epsilon \\ R^\dagger+R_\epsilon^\dagger & 0 & P-Q+P_\epsilon-Q_\epsilon & S+S_\epsilon \\ 0 & R^\dagger+R_\epsilon^\dagger & S^\dagger+S_\epsilon^\dagger & P+Q+P_\epsilon+Q_\epsilon \end{pmatrix}. \tag{2.9}$$

In general, the solutions will be of the form:

$$|\Psi\rangle = c_1\left|\frac{3}{2},\frac{3}{2}\right\rangle + c_2\left|\frac{3}{2},\frac{1}{2}\right\rangle + c_3\left|\frac{3}{2},-\frac{1}{2}\right\rangle + c_4\left|\frac{3}{2},-\frac{3}{2}\right\rangle \tag{2.10}$$

Due to the large confinement energy difference between the pure HH and LH states, the ground states will remain predominantly HH-like, and we can label them generically $|\Psi^+_{HH'}\rangle$ and $|\Psi^-_{HH'}\rangle$. However, the linear polarization will not only reflect the fraction of each state in the ground state but also the relative oscillator strength of that state. For example,

[14] In general, one could also include the magnetic hamiltonian, Eq (2.6), in this. It has been excluded here intentionally. Most importantly, it was excluded because none of the analysis in this document requires predicting the effect of a magnetic field on the linear polarization. Also, it would dramatically complicate the discussion here, which introduces the effect of valence-band mixing on measured linear polarizations. Including the magnetic Hamiltonian would require also mixing the conduction-band states, doubling the number of terms in each equation with very little additional understanding to show for this complication.

the larger oscillator strength of the LH state (see Fig. 3(b)) will cause this state to have a larger contribution to the luminescence. The probability of a particular exciton state to recombine into a photon with polarization direction $\hat{\epsilon}$, will be determined by the dipole matrix element in the direction $\hat{\epsilon}$ between the electron and hole states that consitute the exciton[15]. For example, assuming the equal occupation of these ground states, the intensity of light emitted into polarization direction $\hat{\epsilon}$ is proportional to:

$$I(\hat{\epsilon}) \propto \left|\langle \Psi^{+}_{HH'}| \, \hat{\epsilon}\cdot\vec{p}\,|S\uparrow\rangle\right|^2 + \left|\langle \Psi^{+}_{HH'}| \, \hat{\epsilon}\cdot\vec{p}\,|S\downarrow\rangle\right|^2 + \left|\langle \Psi^{-}_{HH'}| \, \hat{\epsilon}\cdot\vec{p}\,|S\uparrow\rangle\right|^2 + \left|\langle \Psi^{-}_{HH'}| \, \hat{\epsilon}\cdot\vec{p}\,|S\downarrow\rangle\right|^2, \quad (2.11)$$

where the $|S\uparrow\rangle$ and $|S\downarrow\rangle$ states are the s-like conduction-band states with spin up and down, respectively. Now that each of these valence-band states contain components with both up and down spin, none of these matrix elements vanish by conserving the electron spin. Instead we must expand each of these in the basis of Eq. 2.10, which will enable us to express these matrix elements in terms of known matrix elements in GaAs. For example, we can express one of these matrix elements as:

$$\begin{aligned}\left|\langle \Psi^{+}_{HH'}| \, \hat{\epsilon}\cdot\vec{p}\,|S\downarrow\rangle\right|^2 = \Big| & c_1^*\langle \frac{3}{2},\frac{3}{2}|\,\hat{\epsilon}\cdot\vec{p}\,|S\downarrow\rangle + c_2^*\langle \frac{3}{2},\frac{1}{2}|\,\hat{\epsilon}\cdot\vec{p}\,|S\downarrow\rangle \ldots \\ & + c_3^*\langle \frac{3}{2},-\frac{1}{2}|\,\hat{\epsilon}\cdot\vec{p}\,|S\downarrow\rangle + c_4^*\langle \frac{3}{2},-\frac{3}{2}|\,\hat{\epsilon}\cdot\vec{p}\,|S\downarrow\rangle\Big|^2 \end{aligned} \quad (2.12)$$

Since each of these integrals is composed of unit-cell periodic functions (e.g. $u_c^*(\vec{r})\bigtriangledown u_v(\vec{r})$) multiplied by functions that vary slowly over the unit cell (e.g. $\Phi_v^*(\vec{z_h})\Phi_c(\vec{z_e})e^{ik_\lambda + ik_v - ik_c}$),[16] they can be split into to a unit-cell integral and an integral over the slowly varying envelope functions[17]. This allows the use of the electron-hole overlap matrix elements calculated in the simulations by M. Szymanska, displayed in Section 1.3, which we will refer to as $\mathcal{I}_{HH}$ and $\mathcal{I}_{LH}$. Additionally, if we expand the valence-band basis functions, $|\frac{3}{2},\pm\frac{3}{2}\rangle, |\frac{3}{2},\pm\frac{1}{2}\rangle$, in terms of the p-orbital states as in Eq.(1.3a), we can employ well-known microscopic matrix elements,

$$\begin{aligned}\langle X|p_x|S\rangle = \langle Y|p_y|S\rangle = \frac{im_0P}{\hbar}, \\ \langle X|p_y|S\rangle = \langle Y|p_x|S\rangle = \langle Z|p_y||S\rangle = \langle Z|p_x|S\rangle = 0,\end{aligned} \quad (2.13)$$

[15] See, for example, Chuang [15], Section 9.5.2

[16] Here, $\Phi_i(\vec{z_i})$ is the envelope function for the electron or hole in the growth direction.

[17] See, for example, Chuang, Section 9.3.1 [15]

where P is Kane's parameter, known from experiment [67], and m_0 is the free electron mass. For example, we can trivially show that the unmixed $|\frac{3}{2},\pm\frac{3}{2}\rangle, |\frac{3}{2},\pm\frac{1}{2}\rangle$ states have no angle dependence to their emission. If we look at the matrix element between this state and a spin down electron,

$$\begin{aligned}\left|\left\langle\frac{3}{2},\frac{3}{2}\right|\hat{\epsilon}\cdot\vec{p}\left|S\downarrow\right\rangle\right|^2 =& \mathcal{I}_{HH}^2\left|\frac{\cos\theta}{\sqrt{2}}\langle X|p_x|S\rangle + \frac{i\sin\theta}{\sqrt{2}}\langle Y|p_y|S\rangle\right|^2 \\ =& \frac{\mathcal{I}_{HH}P^2m_0^2}{\hbar^2},\end{aligned} \tag{2.14}$$

it is independent of the polarization orientation. However, if we have some mixing between these states, there will be a preferred linear polarization. If we consider the state from Eq.(2.10) with $c_2 = c_4 = 0$, mixing a pair of HH and LH states, the matrix element for this hole state to be filled by a spin down electron is:

$$\begin{aligned}&\left|\left(c_1^*\langle\frac{3}{2},\frac{3}{2}| + c_3^*\langle\frac{3}{2},-\frac{1}{2}|\right)\hat{\epsilon}\cdot\vec{p}\left|S\downarrow\right\rangle\right|^2 = \\ &\left|c_1^*\frac{\mathcal{I}_{HH}}{\sqrt{2}}\langle X-iY\downarrow|\,\hat{\epsilon}\cdot\vec{p}\,|S\downarrow\rangle + \mathcal{I}_{LH}c_3^*\left(-\frac{1}{\sqrt{6}}\langle X+iY\downarrow|\,\hat{\epsilon}\cdot\vec{p}\,|S\downarrow\rangle + \sqrt{\frac{2}{3}}\langle Z\uparrow|\,\hat{\epsilon}\cdot\vec{p}\,|S\downarrow\rangle\right)\right|^2 = \\ &\frac{P^2m_0^2}{\hbar^2}\left(\frac{\mathcal{I}_{HH}^2|c_1|^2}{2} + \frac{\mathcal{I}_{LH}^2|c_3|^2}{12} + \frac{\mathcal{I}_{LH}\mathcal{I}_{LH}\left(c_1^*c_3 + c_1c_3^*\right)}{2\sqrt{3}}\left(2\cos^2\theta - 1\right)\right)\end{aligned} \tag{2.15}$$

Thus, we see that LH-HH mixing always induces some degree of linear polarization in the PL. We can determine the angle of this linear polarization by evaluating the recombination matrix elements of all of the degenerate ground state excitons and determining the angle that maximizes the sum, $I(\theta)$, of these transition rates. Similarly, the degree of linear polarization, β, is simply defined as:

$$\beta = \frac{I(\theta_{max}) - I(\theta_{min})}{I(\theta_{max}) + I(\theta_{min})}. \tag{2.16}$$

So, at each point on a sample, where the parameters that enter into the overall valence-band Hamiltonian (strain, magnetic field) may be varying, the ground state eigenvectors may be found and the linear polarization predicted.

Jeff Wuenschell carried out the above linear polarization analysis from the strain map produced from ANSYS simulations of our trapping mechanism mentioned in Section 2.1. He showed that while there is only a small degree of mixing between the LH and HH states

brought about by strain-induced mixing, there should be a large degree of linear polarization expected from the ground state PL. This is made possible by the much greater recombination rate for light holes magnifying the linear polarization induced by this small mixing.

3.0 EXPERIMENTAL METHODS

Among experimental systems intended to achieve BEC, an excitonic system is unique in its ability to convert its population directly into photons. This mechanism allows much simpler experimental techniques to probe the density profiles than, for example, atomic gas BEC experiments. After creating an exciton population by photoexcitation, the photoluminescence from recombination provides an in-situ probe of the density profile. In fact, as long as the radiative rate for exciton recombination does not vary with position, we can assume the intensity is proportional to the exciton density. Before the experiments reported here and the corresponding prediction of strain-induced valence-band mixing, it was believed that this spatially-constant lifetime was one advantage of the stress-trapping technique over, for example, the electrostatic trapping technique where the spatially-varying growth-direction electric field caused a spatially-varying recombination lifetime. Now, while we will show that this is probably not true at high stress, the photoluminescence still contains valuable information about the population dynamics.

In addition to the excitation and detection, the cryogenic components and trapping in these experiments are also much less complex than the atomic gas case. The precise temperature range at which to expect excitonic BEC is debatable, and some experiments have employed dilution refrigeration to look for this transition down into the range of mK [23]. However, the experiments here range down to about 1.7 K, the practical limit of employing only LHe-4. The trapping mechanism consists of the controlled application of force to the wafer, creating a region of hydrostatic expansion and lower exciton energy. Compared with the elaborate traps for atomic gases, our method of pressing on a wafer's substrate with a pin is somewhat primitive but also inexpensive and effective.

The experimental studies reported here all have a rather similar form, and I will first

focus on explaining the common experimental elements: cryogenic equipment, stress application, photoexcitation, and photoluminescence measurement. Then, I will detail the particular experimental procedures corresponding to specific measurements. This section will neglect the experimental context, leaving a more chronological and coherent discussion of the experiment's progress to Chapter 4.

3.1 COMMON TECHNIQUES

3.1.1 Cryogenic System and Sample Mounting

Nearly all experiments have been performed in a Janis SVT-300 optical, reservoir cryostat. The weakness of the IX luminescence signal typically requires long experiment durations, and this necessitates the use of a reservoir cryostat for efficient helium use. In general, the samples are cooled in LHe vapor, with the exception of experiments using a superconducting magnet in the sample chamber requiring liquid immersion.

The sample temperature is measured indirectly by measuring the temperature of the plate pressed against the wafer, detected by a silicon diode sensor (Lakeshore DT-670). This detector was factory-calibrated to within tens of mK, but the measurement was recorded to a precision of only 0.1 K. The mounted sensor is pressed to the metal plate with a spring to maintain contact at varying temperatures.

The only drawback of this cryostat system, in comparison with a microscope cryostat system, is the working distance for imaging, with a minimum distance from the sample to the first lens of about 3 inches. With a 2" diameter lens, this limits the system's optical resolution, allowing differentiation of features separated by more than $1.5\mu m$ using the roughly $800nm$ luminescence from this structure. Typically, this restriction is no burden to experimentation. The strain traps and corresponding exciton clouds are typically on the scale of hundreds of microns.

3.1.2 Sample-Straining Mechanisms

As explained in Section 2.1, a local hydrostatic expansion of the wafer will create an energetic trap for excitons. This is accomplished by first placing the sample on a flat platform with a hole beneath its center. Then, a sharpened pin presses down on the center of the sample's substrate side from above, causing the sample to deflect downward and creating an overall expansion beneath the pin on the opposite side of the sample, where the quantum wells reside.

The magnitude of this expansion and the degree to which it is localized to a small region under the pin are both determined by the thickness of the sample, with both of these qualities improved by the sample being very thin. Before installation into the cryostat sample holder, the samples are thinned down to about 125 μm thick (removing about 350 μm) by wet etching. Thinner samples would produce deeper and steeper traps, but become too delicate for the manual handling of these procedures (moving with tweezers, etc.). It is certainly possible to work with thinner samples – it only increases the likelihood of breakage upon loading the sample.

The sample preparation method proceeds as follows. The quantum well structures are grown by MBE by L. Pfeiffer's lab at Princeton, arriving at our lab complete, apart from the final sample cleaving and etching. For our stress application, the samples simply must be larger than the hole over which they will be mounted, giving a minimum size of about 3 mm$\times$3 mm. Square samples are typically cleaved from the wafer with a size of (4-5 mm) on each side. After cleaving, the individual sample thickness is measured. In order to etch only the substrate, the sample is mounted on an optically flat piece of glass, using Crystalbond 509 Mounting Adhesive. The adhesive is gradually melted, just above 120°C, after which the optical side of the sample (the side on which the structure is grown) is gently pressed into the melted wax. Gently moving the sample in a circular motion tends to achieve a uniform coverage of the optical side, which is easily verified by examining the reflection from the optical surface through the glass and transparent wax[1]. After the wax hardens, the

[1]Pockets of air underneath the sample can eventually be exposed to solvent during the etching, allowing the optical side to be etched away. This is particularly dangerous if one is etching the sample very thin. Coating the entire optical surface removes this possibility.

thicknesses of the sample and wax are measured again to determine the thickness of the wax by comparison with the original thickness. The wet etch solution, composed of Br_2 and Methanol (10% Br_2 by volume), is then mixed in a fume hood. After wetting a polishing pad with this solution, the mounted sample is rubbed in a circular motion across the pad, stopping in 1 minute intervals to determine the sample thickness. After achieving the desired thickness, the sample is removed from the mounting glass by soaking in acetone[2]. This wax removal may be sped up with ultrasonic vibration, if desired. The sample is then rinsed with methanol to remove the residual acetone. The sample is then placed between the mounting plates on the cryostat sample holder.

In the course of experimentation in this system, the sample-holder and stressor assembly evolved through several forms. The changes were primarily to the way in which stress was applied to the wafer. A mock-up of the original design is displayed in Figure 10. A micrometer at the top of the cryostat insert was used to force the compression of a pair of springs external to the sample chamber. Between these springs, a rigid rod was mounted, extending through an o-ring seal into the sample chamber. A sharpened pin was mounted to the end of this rod to apply a localized force to the sample. This design was first modified by moving the springs to the cryostat interior, and, subsequently, the spring-loading mechanism was replaced with a piezoelectric-driven pin to apply the stress.

With the original design, it was determined that having the o-ring seal between the springs and the sample yielded an inconsistent force on the sample, due to the friction between the o-ring and rod (this connection seals the cryostat sample chamber). In addition to uncertainty in the actual force applied to the sample, the friction makes the rod move in a jerky manner. The stressor rod should only move through the o-ring when the total force on the rod toward the sample exceeds the maximum static friction force, and it should move until the maximum kinetic friction force equals the applied force. Thus, the force will be applied with a minimal increment equal to the difference between the maximum kinetic and static friction forces. While this increment may be small, depending upon experimental

[2]It was a standard practice in this lab in the past to mechanically polish the substrate side of the wafer after etching to achieve a flat surface, for better contact to the mounting plates. However, it has been demonstrated that this degrades the sample quality, and this is no longer performed. So, there tends to be a slight curvature to the sample, as the isotropic nature of this wet etch tends to remove material from the sample edges slightly faster.

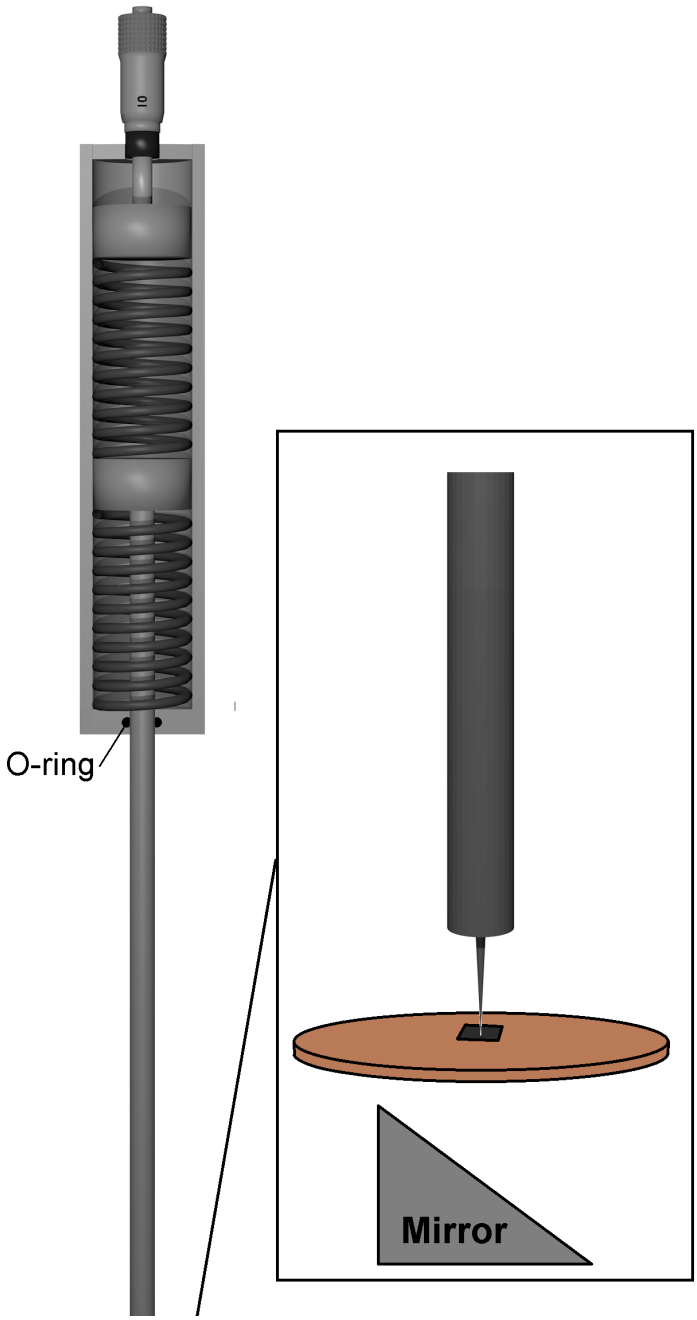

Figure 10: The essential features of the old cryostat insert, with external springs. A micrometer pushes on a pair of springs external to the cryostat. These springs push on a rod that extends into the cryostat through an o-ring seal just below the springs. At the bottom of the cryostat insert, the sample is positioned over a hole in a metal plate. A sharpened pin is attached to the rod extending from the cryostat exterior, which pushes on the center of the sample and creates a localized strain. A 45 ° mirror below the sample allows optical access through the cryostat windows.

conditions, moving the springs to the opposite side of the o-ring, into the cryostat interior, avoids this issue entirely.

The springs in the internal-spring configuration were chosen to allow the pin to quickly approach the sample and to allow finer resolution once the pin touches down onto the sample. The spring constant of the upper spring is chosen to be relatively low with respect to that of the sample so that more displacement of the stressor rod (more turns on the micrometer) is required to achieve a particular deflection of the sample. The lower spring is chosen to have a relatively small spring constant with respect to the upper spring so that, prior to touchdown on the sample, most of the compression is in the lower spring, reaching the sample quickly without exhausting the travel range of the upper spring that will provide the force on the sample.

Later, the spring-driven stressor was replaced with a piezo-driven stressor, in order to allow finer resolution of the force application. The samples would often break at stresses just higher than the stress required for onset of the exciton darkening phenomenon. I believed that finer resolution of the force application would allow us to pass beyond this stress limit, and designed a system around mounting the pin on a piezoelectric-driven, slip-stick stage[3]. This type of stage is a somewhat strange choice for force application, as its method of travel is severely limited by pushing against a load. However, the limited force application of this stage was actually a point in its favor for this application because it may be incapable of supplying the necessary force to break the sample, making the high-stress regime safely approachable. The completed design was found to demonstrate this behavior; it was tested and shown to be incapable of breaking the 125 μm-thick wafers[4] that we typically employ in these experiments.

With any of these sample holders, a careful procedure was employed to safely apply stress to the sample. First, the excitation laser is defocused (or an additional broad laser was incident) to excite the photoluminescence from a large region on the sample. Then, while watching a spectral image of the sample, displaying the emission energy as a function of position along the sample, the stressor-micrometer is rotated slowly. With no strain, the

[3]Attocube, Model ANPx101/RES/LT

[4]However, it may be possible by increasing the amplitude and frequency of the voltage pulses to the piezoelectric beyond the manufacturer specified limits.

energy of the DX and IX photoluminescence is constant across the sample[5], and the onset of strain shows a bowing of this line. Apart from the intended strain shift, a more drastic change is typically evident upon the onset of force on the sample that is typically much easier to observe. With the bias supplied to the sample through the two surrounding plates, the electric field is often dependent on the degree of contact of the sample with these plates. Therefore, pushing on the sample generally modifies the electric field within the wells and causes a sudden Stark shift of the IX line[6]. Once a small amount of stress is applied, the imaging lens position is varied slightly, in the direction perpendicular to the slit, to verify that the image of the trap center is positioned over the spectrometer slit. Then, the stress is increased to achieve the desired trap depth.

3.1.3 Electrical Biasing

In each of the stressor systems, the sample is placed between two metal plates, each with a circular hole through its center that is smaller than the sample. The hole underneath the sample allows it to flex under the applied force, and the hole above the sample allows the pin to press against the sample directly. These plates are held at varying relative electric potential in order to control the electric field across the quantum wells. The electrical bias is simply supplied by a constant voltage source through a resistor, for current sensing, connected to the metal plates via an electrical feedthrough into the cryostat.

With the center of the strain trap occuring roughly in the middle of the holes in the biasing plates, an electrically conductive layer is required on both sides of the sample in order to transmit these potentials to the excitation region on the sample. The substrate side conductive layer is easily accomplished by employing an n-doped substrate. The optical side of the structure requires a relatively transparent conductive layer. The very thin p-doped capping layer of the structure fulfills this criteria in a less-than-ideal manner, as the excitation and luminescence are both at higher energy than the band gap in this layer. Thus,

[5]However, after repeated experiments at high stress, a blue-shifted dimple can develop at the location of the trap center that persists after stress is released and between experiments.

[6]Applying the bias from pin-sample-plate will also accomplish this sudden Stark shift as an indication of touchdown, but this configuration generally has a higher overall resistance and, consequently, a smaller effect.

there is some absorption due to this layer. There is also absorption of the optical excitation within the substrate, but this is not in the observed optical path and has no direct effect on the optical signals.

The field across the quantum wells is strongly affected by the quality of the contacts and the value of the external resistor. Poor conduction to the sample will result in inadequate current to compensate the generated photocurrent within the sample and, therefore, an excitation power-dependent electric field across the wells[7]. It is often the case that even with no external resistor, there is a strong photocurrent dependence to the electric field across the wells, evident in a spatially-uniform blue shift of the IX PL across the sample. Additional evaporated metallic layers on either surface do not result in significantly improved electrical connections, as the connection is most directly affected by the varying pressure between the plates and the sample. A thin layer of indium foil pressed between the sample and the metal plates has made the most significant improvement to the sample-plate electrical conduction, and, to a large degree, it makes the electrical connection less sensitive to the applied force. Foil on both sides of the sample is preferable for the electrical connection, though the foil on the optical side must again have a hole in the center. Pressing these foil pieces to the very thin, delicate sample is quite difficult without breaking the sample, and, therefore, indium foil on both sides of the sample has only been employed in the magnetic field experiments, as explained in Section 4.3. An example of the photocurrent modification to the IX PL energy is demonstrated in Section 4.1.2, where the effect is differentiated from the IX-IX repulsion blue-shift that is also dependent on the excitation power.

3.1.4 Excitation

Excitons were created by an incident laser resonant, or nearly resonant, with the direct exciton energy. To this end, the laser must have a wavelength of roughly 800nm. A 250 mW, 808 nm multi-mode diode laser was temperature-tuned to an appropriate wavelength. The laser was pulsed by applying a 5 V trigger pulse to a transistor switch circuit, with

[7]With any resistance between the sample and applied bias, the potential across the wells will be determined by a voltage division between the external and internal resistance, and any photocurrent will essentially act to decrease the internal resistance and decrease the internal voltage. If the external resistance is made small enough, this effect can be made negligible.

the timing controlled by a digital pulse generator. For temporal resolution, distinguishing excitation and decay, the laser was typically turned on for 1-2 μs and then switched off,[8] with a repetition period of 8 μs. This pattern was varied slightly throughout to meet the goals of some particular experiments[9]. The average power of the excitation was varied between roughly 1 μW to 5 mW. The laser was focused by a 150 mm focal length lens and passed through the same cryostat window through which the PL exits. It entered at a large angle so that the laser's specular reflection was not collected by the imaging lens.

It is sometimes desirable to employ an excitation energy slightly higher than that of the direct exciton, such as when mapping out the energy of the strain trap. With the application of stress, the DX energy varies with position. Thus, if it is desired that the system be nearly uniformly excited over the entire trap with a defocused laser, the DX resonance should be avoided, and the laser energy must be set higher, exciting the free-carrier continuum rather than exciton states. A much shorter wavelength laser is not used, however, as in many similar coupled quantum well experiments that employ HeNe lasers, in order to avoid heating the wafer with the excess electron energy. In addition, in our samples, a significant photocurrent is excited for laser excitation with wavelength shorter than 772 nm (at zero applied force)[10] that easily overwhelms the built-in and applied field. The nature of this absorption was not studied in depth; it simply set the high end of the excitation range employed in these experiments. The temperature was originally manually stabilized by modifying the bias across the peltier as the temperature was seen to drift. It was later determined that this energy tuning was too critical to allow any significant drift, and a commercial PID setpoint system was employed to dynamically set the peltier bias.

3.1.5 Photoluminescence Detection

Some of the PL emitted from the sample passed through the cryostat window and was focused by an imaging lens. The focal length of this lens varied between 75 mm to 150 mm,

[8] To approach the maximum density of IXs for a particular excitation power, the laser should be on for roughly the lifetime of the IXs.

[9] For example, the experimental duration was increased when it was desired to observe several decades of intensity decay, often requiring about 100 μs

[10] It should be noted that almost all electronic transitions shift downward in energy with expansion of the crystal, so this wavelength minimum should be increased if one is applying stress to the sample.

depending on the experiment, with magnification from -11.2 to -4.4. The image was focused onto the entrance slit of a 500 mm focal length imaging spectrometer (SpectraPro 2500i), with a 1200 g/mm grating with 750 nm blaze.

An intensified CCD (ICCD) camera (LaVision Nanostar) mounted on the spectrometer exit port collected time-resolved images of the luminescence. The intensifier employs an S25 (Gen II) photocathode to convert the photons into electrons. These electrons are accelerated into a multichannel plate (MCP) by a gating voltage on the MCP front surface of -50 V (off) to 180 V (on) with respect to the photocathode. The internal HV pulser in the ICCD is able to switch this voltage quickly, so that 5 ns exposures may be achieved. The MCP consists of a fiber optic plate with slightly tilted channels and a high voltage across its length, generating a large electron gain as it is traversed. This voltage (0-1 kV) determines the gain of the MCP. The electrons are then accelerated by a static 5 kV to a phosphor screen, where they are converted back into photons. This is followed by a CCD with 1280×1024, 14.5 μm wide pixels.

Unfortunately, the cooling requirements of the HV pulser in this camera impose severe restrictions on the experiment. The pulser is only able to stay cool at pulse-repetition rates below 25 kHz. With microsecond exciton lifetimes, the desired experiment repetition rate is about 125 kHz. With the support of the manufacturer, it was determined that with a 125 kHz experiment (laser) repetition rate, the ICCD could only be used in a 100 pulses on, 400 pulses off configuration. Even with this reduced duty cycle, the HV pulser on this camera ceased functioning after five years of operation in this mode. If possible, it is advised that further experiments in this system would gain substantially from an upgrade of this camera. A significant signal gain should be available, since some current ICCD systems do not have such a restrictive timing limit, and, furthermore, the switch from a GenII (multialkali) photocathode with ≈5% quantum efficiency at 800 nm to a GenIII(filmless) GaAs-based photocathode with >25% Q.E. should yield another factor of 5 in the signal, potentially dramatically decreasing the necessary exposure times and, therefore, liquid Helium consumption.

The ICCD gate timing is performed by a digital delay generator. This is the same pulse generator that provides the 5 V pulse to switch the excitation laser diode. After this

excitation trigger and a variable delay, it subsequently generates a TTL signal to trigger the ICCD optical gate. Typically, the ICCD is optically gated to collect a few microseconds of the 8 μs experiment. The CCD is read-out every 1-10 seconds, integrating on-chip until the CCD full well capacity of 25k electrons is approached. Many of these exposures are then summed in the LaVision DaVis software to achieve an appropriate signal/noise ratio. A single time-resolved image of the IX PL may take 15 minutes of these exposures due to the low signal level.

In general, the camera is collecting one of two types of images, either 2D spatial images or "spectral images" (1D spatial + 1D spectral). Both of these collection schemes are performed through the imaging spectrometer. For the spectral imaging mode, the spectrometer is set to disperse the desired wavelength range of the first-order diffraction image over the camera in the horizontal direction. The vertical dimension remains unaltered from the image of the spectrometer input slit, so that the output to the camera is vertical slit position vs wavelength. The dispersion from the spectrometer is such that each pixel on the CCD represents a spread of wavelengths of 0.02 nm (or 36 μeV at 820 nm), which is calibrated with a Kr or Ne calibration lamp. The imaging mode is achieved by setting the spectrometer wavelength to 0-nm to collect the "0-order" reflection of the image. In order to image just the IX photoluminescence, the collection is time-resolved, and , often, the light is also passed through a bandpass filter centered at $\approxeq 819 \pm 5$ nm.

3.1.6 Magnet system

In order to determine whether the PL darkening was due to the presence of dark excitons, a magnetic field was applied along the quantum well plane to attempt to mix the dark and bright states. To this end, it was necessary to design a new sample holder and stressor system to incorporate electromagnet coils within the cryostat sample chamber. Including all of these experimental elements within the sample chamber's 1.46" inner diameter severely limits the size of the electromagnet and its field/current. So, an efficient coil design was critical to achieve a significant magnetic field with experimentally tolerable currents within the cryostat.

A sketch of the important components of the magnetic stressor assembly is shown in Figure 11. Figure 11(a) shows the mounting plate for the sample below the stressor plate that houses the compression springs and pin. Two rectangular sections are cut from each of these plates to allow a cylindrical coil to be positioned on either side of the sample, oriented with the coil axis in the sample plane to cause an in-plane magnetic field. Figure 11(b) displays a single coil on the vertical mounting bar that attaches it to the upper part of the stressor assembly. The coils are attached to the upper part of the assembly due to space constraints. In addition, this convenient geometry allows the coils to be more easily removed, which is necessary for sample loading/removal.

The desired superconducting wire properties were determined by simulating the field[11] from the magnet coil at the current required to reach 2 T at the sample. For a particular wire diameter, the manufacturer specifies the critical current vs magnetic field. Thus, the critical current for the maximum field inside the coil was compared with the required current to determine whether the wire was suitable. This essentially rules out the thinnest wires, as the critical current decreases with decreasing wire diameter much faster than the input current demand to reach 2 T (from increasing the number of loops that will fit in a given space). The criterion on the large diameter end was imposed by the desired maximum input current into the cryostat sample chamber, considering that the non-superconducting leads will be generating heat. A Cu-clad NbTi wire with clad-diameter of 0.114 mm (insulated diameter 0.14 mm) was chosen to meet these requirements, with the expectation that it should take under 10 A to reach over 2 Tesla. The final coils were found to together provide 0.236 Tesla/A at the sample in the final configuration.

The choice of lead wires to the superconducting coils was nontrivial, as they are sources of a large amount of heat. Large diameter wires are unacceptable in conducting too much heat into LHe from the exterior, and small diameter wires will generate too much heat due to the large current. In past magnet experiments in this lab, we have simply used the superconducting wire as the entire lead to the cryostat feedthrough, but those used significantly lower currents (<2 A) due to the larger available space for the coils. For this

[11]This simulation used the exact solution of the field from a single loop and stacked these loops to find the total field. This fast computation neglects the pitch of the coil wraps, which is very small compared to all other distances in the problem.

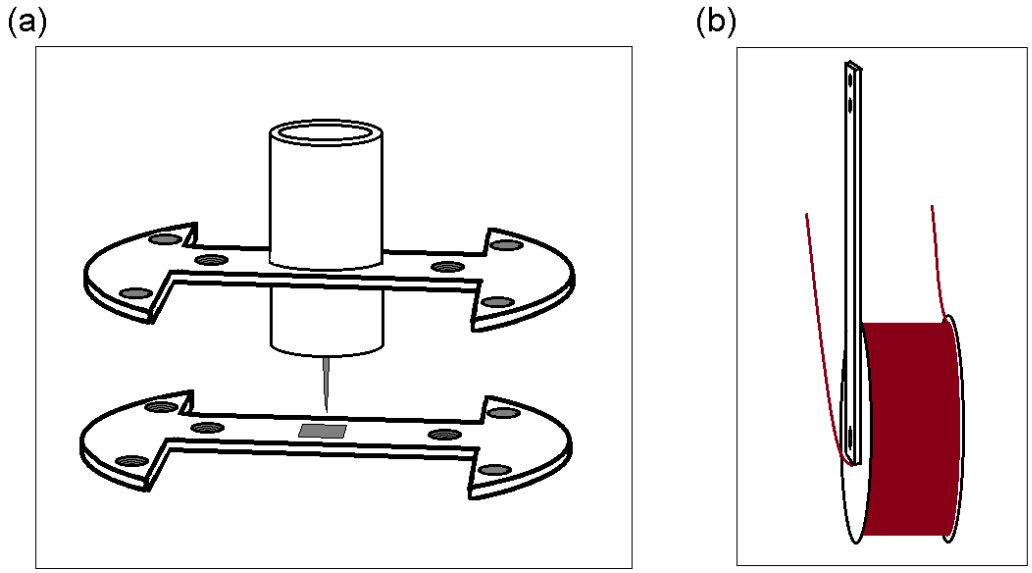

Figure 11: Sketches of the primary magnetic stressor components. (a) The sample base plate is shown on the bottom, with the sample centered, in gray. An additional plate would sit on top of the sample, pressed against the sample via spring loaded screws at the two tapped holes in the inner rectangular section of the sample base plate. The stressor plate sits above this, separated by vertical support posts (not pictured) at the four outermost holes in the plates. The spring shaft is centered on this upper plate and contains the two compression springs (not pictured) that apply force to the pin. Two large rectangular sections of each of the circular plates are removed to allow coils to be placed in close proximity to the sample (oriented with the coil axis in the sample plane). A coil is positioned on either side of the sample in these two rectangular slots. The diameter of the circular plates is 1.45", just fitting into the 1.46" inner diameter of the cylindrical cryostat sample chamber shaft. (b) One coil is pictured with its mounting bar. When installed, it is oriented so that the coil axis is in the plane of the sample. The vertical rectangular bar is mounted against the outer edge of the coil, held by a screw into the coil center. This mounting bar extends upward about 3 inches, to attach to the upper section of the stressor assembly with two screws.

experiment, the superconducting wire was extended from the coils up to several inches above the coils, to the maximum height where there should always be liquid Helium so that the wire always remains superconducting. Then a junction was made to a larger diameter (20 AWG) wire.

Initially, my intention was to employ an available, commercial high-current DC source to supply the current to these coils. Upon ramping up the current in the coils, under experimental conditions, the source immediately jumped from <1 A to over 15 A, due to a faulty adjustment knob, which quickly burned out the magnetic coils. While a setback, the nature of this burnout highlighted the weak points of this design. The wire was most damaged at two points, at the junction between the SC and normal wire and at the point where the SC wire entered the coil for the innermost wraps. Two new coils were wrapped to replace these initial coils, with careful attention to avoid any small kinking of the wire where it enters the innermost part of the coil, and the normal wire leads were extended slightly farther down toward the sample (farther past the normal LHe level) to facilitate cooling of the wire junction. This experience also suggested that the vicinity of 15A is not a safe current range for this device. The current, henceforth, was supplied up to 6 A by two 3 A DC current sources in parallel. It is likely that higher field could be safely achievable with this system above 6 A, but, due to the desire to use this system for future projects, it was unprofitable to push the current higher.

To safely operate this magnet system, the Helium level in the sample chamber was carefully monitored. This first required the installation of a Helium level monitor alongside the cryostat insert rod. Before supplying current to the magnet, the resistance of this monitor was measured to ensure that the liquid was above the level of the SC-normal wire junction. The liquid helium flow was then adjusted to approximately equilibrate at this level while maintaining the liquid helium below its superfluid transition temperature[12]. The current

[12]This procedure of adjusting the helium flow should proceed as such: 1) Begin to pull liquid helium into the sample chamber, 2) Adjust the exhaust pump valve to bring the liquid below its superfluid temperature, 3) increase the helium flow into the chamber so that the level slowly rises to the desired level (perhaps adjusting the flow while the level is visible in the cryostat window to get a feel for the necessary equilibrium flow rate), and 4) adjust the flow rate to maintain a constant resistance on the level monitor. The important point here is not to reverse steps 2 and 3. Adjusting the temperature to the superfluid transition will cause wild bubbling of the Helium. If this is done while the helium level monitor is submerged, the splattered Helium will make finding an equilibrium reading very difficult.

is slowly increased, while monitoring resistance across the electrical feedthroughs to ensure that the coil resistance is constant.

3.2 SPECIFIC MEASUREMENTS

3.2.1 Lifetime Measurement

Voros et al [79] demonstrated that, due to the long lifetime of IXs, the excitons will sample a large region of the trap before recombining (drift and diffusion occur much faster than recombination). If this is always true, this means that we can't measure the lifetime of excitons at a single point on the sample by looking at the decay of the luminescence at that point because the rest of the trap will be continually contributing/removing excitons from this region–the local density is always determined by the trap profile and the total density. Thus, we are left measuring only the total population lifetime. While my previous statement might suggest it, we also cannot measure the decay at a single point to determine the total population decay (at least we cannot without knowing and accounting for the shape of the trap and the change in the chemical potential over time). As the total number of particles decreases, the total interaction energy decreases, and the excitons become less likely to be found at the outer regions of the trap. This density-driven shift of the excitons in space and energy means that we must always look at the decay of the spatially- and spectrally-integrated luminescence over time to determine the lifetime of the IX population.

This may be accomplished either by integrating a 2D image over the spatial dimensions or by spectrally- and spatially- integrating a spectral image. I choose the latter option as it offers the opportunity to spectrally filter out the DX and substrate luminescence. For this, spectral images are taken with the spectrometer slit completely open to view the diffracted luminescence from the entire illuminated region. It is a happy coincidence that the spectral+spatial width of the IX luminescence is typically much smaller than the spectral distance between the IX PL and neighboring emissions, making the spectral filtering possible. So the lifetimes reported here are based on the total first-order diffracted luminescence,

integrated spatially and over some spectral window.

3.2.2 Spatial Coherence Measurement

In order to test for BEC, we have attempted to measure any long-range spatial coherence of the excitons in our system. A Michelson interferometer was constructed following the imaging lens. It has been noted by others that the numerical aperture of the collection system should be maximized in order to avoid measuring an inflated coherence length due selecting a small range of in-plane momenta [49, 48]. Thus, for this experiment, the typical reservoir cryostat was swapped out for a continuous flow cryostat, allowing a slightly smaller working distance, and a 3" focal length (2" diameter) lens was used instead of the usual 4" focal length. This allowed a collection angle of roughly 18 degrees from the sample normal.

This collimated signal was then incident on a plate beamsplitter, the first element of the Michelson interferometer. A plate beamsplitter was used instead of a pellicle because the center of a 2" pellicle was found to vibrate wildly in our setup, seemingly from air currents in the room. The signal was reflected back by two 3" diameter, front surface mirrors. Large diameter mirrors were used again to avoid reducing the NA of the system (although smaller, 2" mirrors, had they been available, would have been more suitable). Once recombined, the signals were refocused onto the spectrometer slit by a 500 mm focal length lens. This gives a spatial calibration for the CCD of capturing 2.2 microns of the sample per pixel.

Due to the long exposure time required for these images, I constructed an active stabilization system for the interferometer to negate the effect of path length drift over time. The path length was coarse-adjusted by a motor-controlled micrometer screw and fine-adjusted by an additional stage employing a piezoelectric element in place of the micrometer screw. The piezoelectric bias was controlled by the voltage-amplified output of a DAQ board. For feedback on the path length difference of the interferometer, a reference HeNe beam was additionally sent through the interferometer. The power of the reference beam output was measured with a photodiode, the signal of which was amplified and input into a computer via the DAQ board. A dedicated PC running the MATLAB Real-Time xPC Target environment read out the DAQ input voltages, interpreted the relative phase, and calculated the

output signal to send to the piezoelectric element to adjust the phase. The zero time delay location was found by passing a femtosecond laser through the interferometer, scanning the delay, and locating the position of maximum signal oscillation. The phase was stabilized to roughly $\pm$ 3 degrees, and this variation happened on very short time scales. Thus, this limitation on the phase stabilization was likely caused by the very large mass of the thick, 3" mirrors and the corresponding difficulty of pushing these around at the acoustic frequencies required to compensate for small table vibrations. Most importantly, though, the long-term drift of the phase was eliminated.

The measurement of coherence proceeds by very slightly misaligning the images from the two interferometer arms to observe any fringes that occur due to the slightly differing incidence angles. This technique is modeled after similar experiments in microcavity polaritons. It should be noted that this procedure is only valid for systems where we expect the coherence length to be longer than the image misalignment used to detect the fringes. For example, if a fringe maximum is to be observed every 400 pixels of the image, then the two rays[13] must have $\Delta\theta = 0.008\,^\circ$. This corresponds to a misalignment of the two images, such that regions that are 8.5 μm apart on the sample are overlapped. Increasing the spatial frequency of the fringes requires an even larger angular misalignment and, consequently, a larger spatial misalignment. Thus, we have implicitly assumed by using this scheme that we have a coherence length on the order of many microns. If, for example, the coherence length were 1 μm, then the fringes will fade for image misalignments that overlap regions of the sample more than 1 μm apart. Overlapping points 1 μm apart on the sample produces an interference maximum every 4.5 cm, which is much larger than our CCD size. These fringes would not be observable. The size of the luminescencing region of the sample is typically about 500 μm, giving a practical limit to the observable fringe spacing. With this fringe period, the two images will overlap parts of the sample that are about 7 μm apart. This is approximately the minimum coherence length that is detectable with this measurement scheme. Therefore, if we detect any fringing at all, we are well out of the Maxwell-Boltzmann-like exponential

[13]Here, they are actually two individually-converging ray bundles, but we are assuming that for each ray in the bundle there is a corresponding ray in the other shifted by some overall $\Delta\theta$. In addition, we have used the paraxial ray approximation by using $\sin\theta_A - \sin\theta_B \cong \sin(\theta_A - \theta_B)$, so that all off-axis points have the same path length dependence on the misalignment angle. This is decidedly accurate in our case, as these angles for points included in the image are less than 0.005 radians.

decay, which has a coherence length of about 100 nm.

3.2.3 Linear Polarization Measurements

In order to quantify the degree of valence-band mixing due to strain, one can measure the linear polarization of the IX PL as a function of position. This measurement proceeds in the same way as for normal imaging, except that a linear polarizer (the analyzer) is inserted before the spectrometer. Then, for each desired polarization map, many images are taken with different analyzer orientations, and the degree of linear polarization and the linear polarization angle are determined from fitting this data. Though we are primarily using this technique to study the strain-induced mixing, it is not only this linear polarization analysis that requires mapping of the polarization. Due to the spatially-varying polarization and the strong polarization bias of our detection system, simply measuring accurate intensity profiles requires this analysis as well.

When considering intensity data from any source with a varying linear polarization (degree and angle), it is important to compensate for the polarization detection bias of the system. In our system, this is required primarily due to the spectrometers high degree of bias toward vertically polarized light. In the desired wavelength range, the polarization degree induced by the spectrometer grating on unpolarized light was measured to be just under 90%, significantly skewing the intensity map of any image containing high degrees of linear polarization over a wide range of angles. For the purposes of both linear polarization measurement and detection bias compensation, we require 1) knowledge of the degree and orientation of the polarization bias and 2) many images with different analyzer orientations.

In seeking to satisfy this first requirement, to characterize the degree of spectrometer polarization bias, it was found that it is quite sensitive to the details of the imaging setup. It was expected that inputting unpolarized, collimated white light directly into the analyzer and, subsequently, the spectrometer, would allow extraction of the spectrometer polarization bias through fitting the transmitted intensity at each analyzer angle. However, the degree of this polarization bias varied by up to 5% when comparing the result of directly inputting collimated white light into the analyzer to the result of putting the same light through

various subsections of the optical path before the spectrometer. Therefore, it is necessary to replicate the photoluminescence characteristics as closely as possible with unpolarized light. For this purpose, I collected PL from the substrate of the (unstressed) sample in nearly the same spectral range as the experiments, excited by unpolarized white light, with the sample temperature at about 70 K. With the sample unstressed and with unpolarized excitation, there should be no bias in linear polarization of this PL. This data is then fitted to determine the intrinsic polarization bias.

Extracting an intensity or polarization map first requires compensating each image by the degree to which the analyzer and spectrometer bias are aligned. Specifically, for each analyzer angle, each entire image is divided by a correction, C,

$$C = (1 - \eta) + \eta \cos^2(\alpha) \tag{3.1}$$

where α is the angle between the analyzer and the vertical, and η is the degree of polarization bias due to the spectrometer. At this point, one may extract the total intensity emitted at each point. A pixel at point (x,y) for a given analyzer angle, will have an intensity after the analyzer, I[x,y], of

$$I[x, y] = A[x, y](\beta[x, y] \cos^2(\alpha - \theta[x, y]) + (1 - \beta[x, y])), \tag{3.2}$$

where θ[x,y] is the local emission angle, β[x,y] is the local degree of linear polarization, and A[x,y] is the intensity when the emission angle and the analyzer are aligned. The total intensity at each point, adding the polarized emission and the unpolarized part, is:

$$I[x, y] = A[x, y] + A[x, y](1 - \beta). \tag{3.3}$$

These parameters then must be fitted for each pixel of the image.

It should be noted that this analysis was not done for every image in this document, and it will be noted when it was performed. It is most relevant in the spatial images of the high-stress trap, where there is significant variation in polarization direction over the image. In this case, if we show a single image taken without performing this procedure, the shape of the intensity map could be distorted, depending on the orientation of the sample crystallographic axes with the spectrometer slit. Typically, this causes the image to look

slightly rotated (with the higher intensity lobes tilted slightly off-axis) due to the way the linear polarization rotates as one moves in a circle around the trap center.

4.0 EXPERIMENTAL RESULTS

4.1 UNSTRESSED AND LOW-STRESS RESULTS

This system at low stress was previously explored by Z. Voros et al. [78], focusing in particular on the IX-IX interaction and exciton equilibration. Most of the features of the low stress system reported here are covered in that document and past work from this group. These low stress results are reviewed here predominantly to provide context for the high-stress behavior and, in particular, to highlight some common experimental difficulties/ambiguities, such as identification of spectral lines and the origin of their energy shifts.

4.1.1 Unstressed Spectrum

Figure 12 shows a typical unstressed spectrum for a sample with 14 nm wells. The presence of the higher energy, brighter DX photoluminescence makes it apparent that this image is not time-resolved. It will typically be the case, here, that any image that displays the DX lines has been time-averaged over the entire excitation and decay, since the DX decay (into IXs or photons) is relatively fast. Similarly, the dim light at the high energy edge of the image is the trailing end of the scattered excitation laser, and the dim spectrally-broad light on the low energy side is substrate luminescence. In this case, the laser is defocused, to illuminate a large section of the sample, and non-resonant (detuned by about 15 meV). There is zero applied bias in this image, so the built-in field from the *p-i-n* structure is providing the electric field to set the IX energy far below that of the DX. The bright luminescence directly below the HH DX state is the HH BiDX line.

If we look at the higher energy half of this spectrum in more detail, as in Figure 13, it

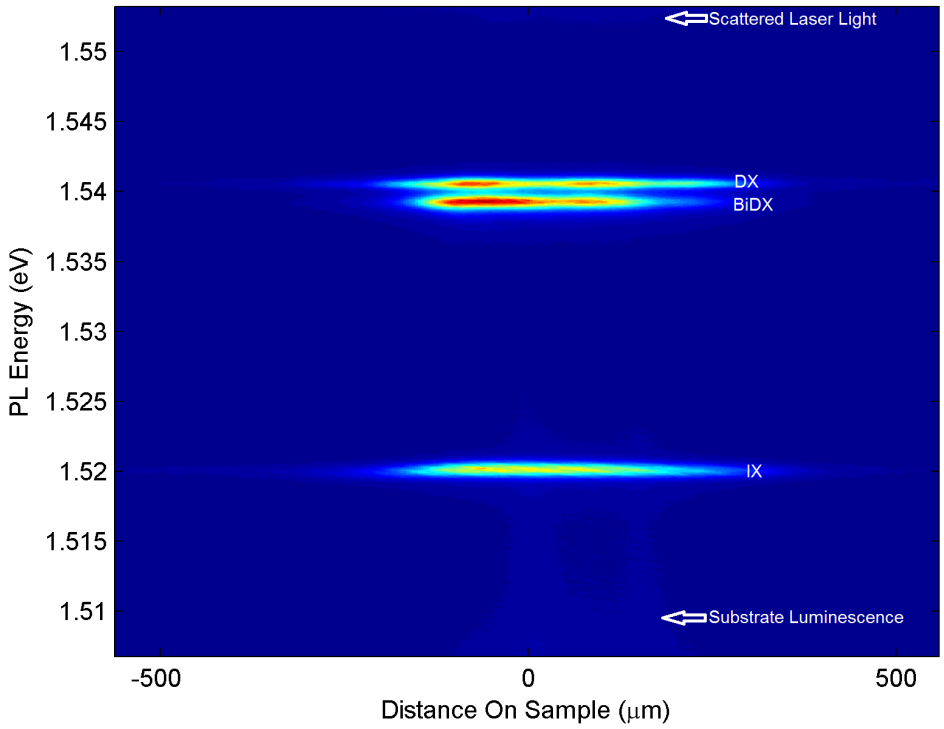

Figure 12: Spectral image of unstressed photoluminescence. The sample has 14 nm wells and is excited over a wide area by a defocused laser. The DX and BiDX lines, at higher energy, are observed here in addition to the IX line, as this image is not time resolved. Temperature: 4 K. Applied Bias: 0.0V. Average Excitation Power: 0.75 mW.

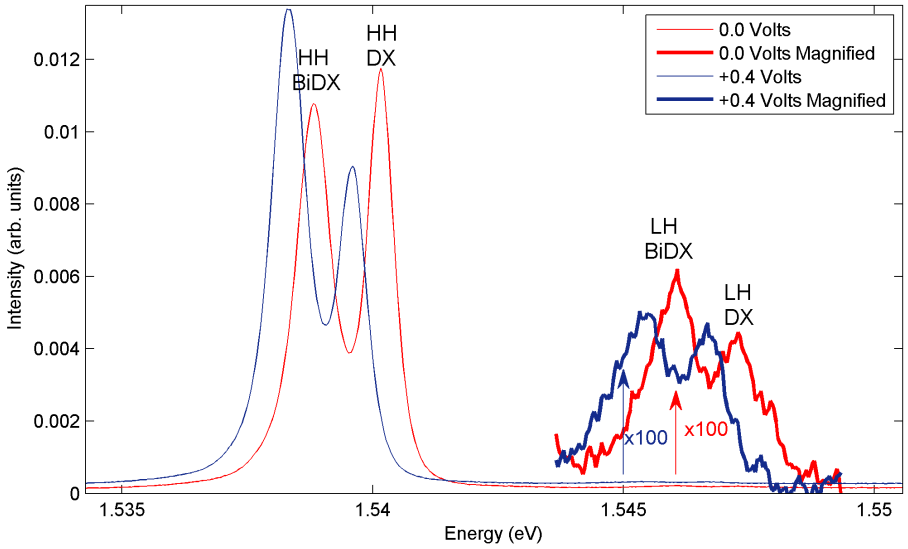

Figure 13: DX spectra under two different applied biases. The spatially-integrated spectrum from Figure 12 is shown along with the spectrum with a 0.4 V applied bias augmenting the built-in field. The presence of the LH DX luminescence is detected in both cases, and it is shown to also have a bound molecular state at slightly lower energy, labeled as the LH BiDX. The Stark shift of these DX states is much smaller than that of the IX states (not pictured).

is possible to discern the LH DX luminescence with significantly lower intensity. This plot also shows the spectrum with a slightly higher electric field, with 0.4 V applied across the sample. With the biased data, we can see that both the HH and LH states shift similarly under the QCSE. The LH/HH DX splitting, $\Delta E^{DX}_{LH/HH}$, is observed to be 7.0 meV for this sample, in both circumstances. In addition, from the magnified section, we see that the LH DX spectrum also has an associated biexciton state, with both HH and LH lines split from their molecular counterparts by 1.3 meV. The presence of this second LH line initially caused some confusion, as it is far more common to observe only a single LH emission line. This is one circumstance where the excitation characteristics are extremely important. Here, we see both lines because the excitation is unfocused. Performing this same experiment with a focused laser, i.e. with an extremely high excitation density, shows only emission from a state 5.7 meV above the HH DX. Only the molecular LH DX line (LH BiDX) is observed in this case because it becomes very probable that an exciton is able to find the necessary carriers to create the lower energy molecular state. Dimming a focused laser until the bare LH DX is also observed would produce an extremely low total signal from the LH states. Thus, the most efficient way to observe both the DX and BiDX lines is to excite with high power over a large area and spatially-integrate the results. The density-driven growth of the BiDX line responsible for this behavior is similarly observed for the DX HH, which can be seen later in Figure 16(a).

4.1.2 IX Stark Shift

As we have predicted in Section 1.3, the Stark shift of the IX states will be far more pronounced than that of the DX, due to the electron-hole separation. This is demonstrated in Figure 14, where spectral images of the HH DX and IX states are presented at varying applied bias with a low stress applied to the sample. In this case, the bias is applied in opposition to the built-in field, so the Stark shift is reduced as the bias is increased.[1] Clearly, the IX energy shifts strongly to higher energy as the electric field across the wells is reduced,

[1]This is not typical for the high-stress experiments of interest to this dissertation. These low electric field conditions are used here simply to demonstrate the main effects of the bias change, as the effects (e.g. decreasing linewidth) are more pronounced in this regime.

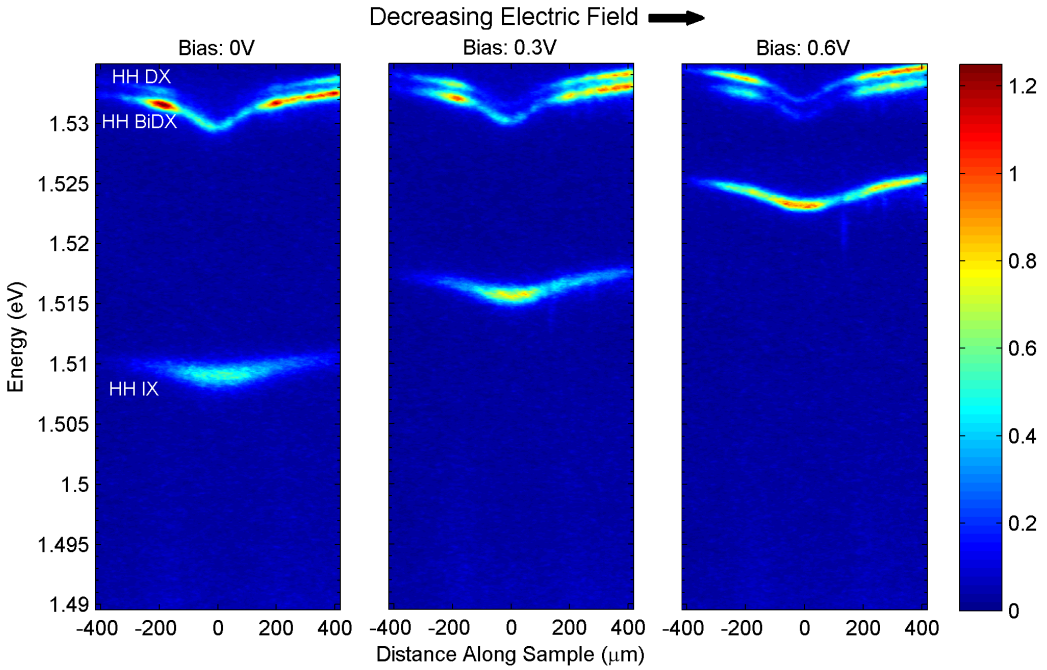

Figure 14: Spectral images with varying applied bias in the presence of a weak stress trap, as described in Sections 2.1 and 3.1.2, demonstrating IX Stark shift. The IX spectral line is observed to increase in energy with decreasing electric field, in accord with the prediction of the Stark shift. In this case, the bias is measured in opposition to the built-in field, decreasing the electric field across the wells with increasing bias. We can infer from the observed narrowing of the linewidth and trap flattening that the IX lifetime is increasing with increasing electric field.

in accord with expectations. The HH DX state also shifts to a higher energy by a much smaller degree, due to the smaller degree of polarization allowed by the single quantum well.

In addition to the shift itself, there are a few important features in this series. First, we note from the DX intensity profile that the absorption of the defocused laser is highly spatially non-uniform, favoring the trap perimeter. In this series, the laser energy is roughly set to the unstressed LH DX energy, so with stress applied it becomes resonant to the LH DX state only on the outer regions of the trap. If this feature is undesirable, it can be remedied by slightly decreasing the excitation laser energy to favor the trap bottom. However, in this case, the non-uniform intensity profile is advantageous, allowing us to highlight the difference in intensity profiles between the DX and IX PL. The IX spatial intensity profile near 0 V is determined solely by the trap profile, as the IXs live long enough to spatially equilibrate in the trap. As the bias is increased, to decrease the field, the IX intensity profile more closely resembles that of the DX absorption. So, we see the first signs that the IX lifetime increases dramatically with increasing electric field. The dim center of the DX luminescence, here, is only due to the laser being set to the resonance of the LH DX on the trap perimeter. Later, at higher stress, a separate transition occurs that darkens the center of the DX state and, at an even higher stress, darkens the center of the IX state. In that case, the transition occurs even with the excitation much higher in energy than the DX transitions, where there is very little excitation preference for the trap periphery or center. So, the case illustrated here demonstrates the importance of controlling the excitation energy, if one is concerned with the spatial structure of the PL. One could easily be fooled into observing the IX trap-center darkening transition, on which this dissertation is focused, at a much lower stress if the excitation is resonant to the trap periphery and the IX lifetime is short enough to allow the IX intensity profile to reflect the DX excitation profile.

Further evidence of this lifetime change exists in the flattening of the IX energy profile and the increase in the spectral linewidth with increasing electric field – both of these reflect the increase in density resulting from the decreasing decay rate. With a larger electric field and its corresponding lengthened lifetime, a larger IX population is able to build up during the laser pulse. The dynamic blue shift (the shift due to exclusively to IX-IX repulsion) and linewidth of the IX PL spectrum have been experimentally demonstrated to monotonically

increase with density [80]. The monotonicity of the blue shift with density is consistent with the mean-field description given in Section 1.4. The increase in the linewidth reflects the increase in the IX-IX elastic scattering rate with increasing density. Here, both of these features are seen with increasing electric field, in a slight flattening of the trap and in a dramatic increase in the linewidth of the IX spectrum.

However, the observed linewidth change is actually somewhat inflated by the dynamic blue-shift in these images, as the images are time-averaged. The larger electric field cases show a larger dynamic blue shift, which decays over the course of the period between pulses (a 6 microsecond delay, in this case). Due to the relatively low electric field in all of these images, the IX population is able to decay significantly over this period, decreasing the dynamic blue shift over time. For this reason, when comparing linewidths, one must use exposures much less than the lifetime of the IX population so that the population remains relatively constant during the exposure. So, the linewidth increase with increasing electric field observed here is at least partially due to a larger dynamic blue shift and its subsequent decay, but this is still symptomatic of a lifetime increase and its correspondingly increased density. An accurate representation of the linewidth with varying density is presented later, in Section 4.1.3, Figure 17, where a time-resolved measurement displays accurate time-slices of the data.

In Figure 14, there are also a few spatially-localized, spectrally-broad peaks trailing down from the IX line (the most prominent extends below the IX line at about +100 μm from the center in the 0.6 V image)[2]. At high electric field, the intensity of these streaks dim and eventually disappear. It is certain that there is some defect at this position. It may be that the AlGaAs barrier is slightly thinner in this small region, yielding a slightly lower energy at low electric fields due to an increased binding IX binding energy. This is only one possibility, but it seems to offer qualitative agreement with the features of this streaking[3]. The dimming of these localized spectral peaks with increasing field could be due

[2]These streaks are actually much more localized in space than indicated in this image series. The fact that they are more than a pixel or so wide is indicative that the imaging system is very slightly out of focus, and the shape of this line can be regarded as roughly the point-spread function of this image in the direction along the 'distance direction'.

[3]A lower alloy fraction of Al in the barrier could also reproduce these prediction to some degree, producing a lower barrier rather than a thinner barrier.

to an increasing lifetime, either directly by allowing these states to cascade down into the lower IX state before recombining or due to the corresponding increased density, where the states become relatively dimmer by being washed out by holding a smaller fraction of the total population (due to the IX-IX repulsion, spatially-localized defect states tend to allow a relatively low occupation before 'filling' the defect potential). It was shown by Denev et al. [19] that such barrier defects are likely responsible for a large part of the current through the wells in coupled quantum well structures that have high in-plane diffusion constants, allowing carriers to find these regions of increased tunneling probability. In any case, the IX line is typically well below these localized states in energy, and samples with many of these defects are typically replaced, as they tend to occur alongside an increased current through the wells.

In addition to the desired Stark shift characteristics displayed in Figure 14, a less desirable aspect of this Stark shift behavior is demonstrated in Figure 15, showing two measures of the IX energy shift with bias for two different times during the same experiment. Again, the bias is applied in opposition to the built-in field. The two cases here display the shift, under the same experimental conditions, before (red) and after (blue) a large stress is applied and released from the sample, and the disparity in the shift illustrates the difficulty of achieving consistent sample-plate contact due to this experimental design. Due to this difficulty, we must be aware that the applied bias cannot be used to directly determine the IX spectral position. Typically, when trying to make a comparison to theory, one must determine the electric field across the wells. In order to do this, we must make a theoretical prediction of the IX energy and match this with the observed spectral position to determine the relevant electric field. For example, from the energy splitting of 23 meV (in the low density regions on the trap periphery, avoiding the effect of the dynamic blue shift) between the HH DX and the HH IX in the 0 V condition, we can infer from the theoretical simulation presented in Section 1.3 and, in specifically, Figure 3, that the electric field at 0 V is just over 10 kV/cm.

The electric field across the wells is also affected by photocurrent generated in the sample by the excitation laser, as mentioned in Section 3.1.3. This has been reported on previously by Negoita et al. [52], demonstrating that a DC blue shift with increasing average excitation power existed in this experimental configuration, essentially due to photocurrent and appre-

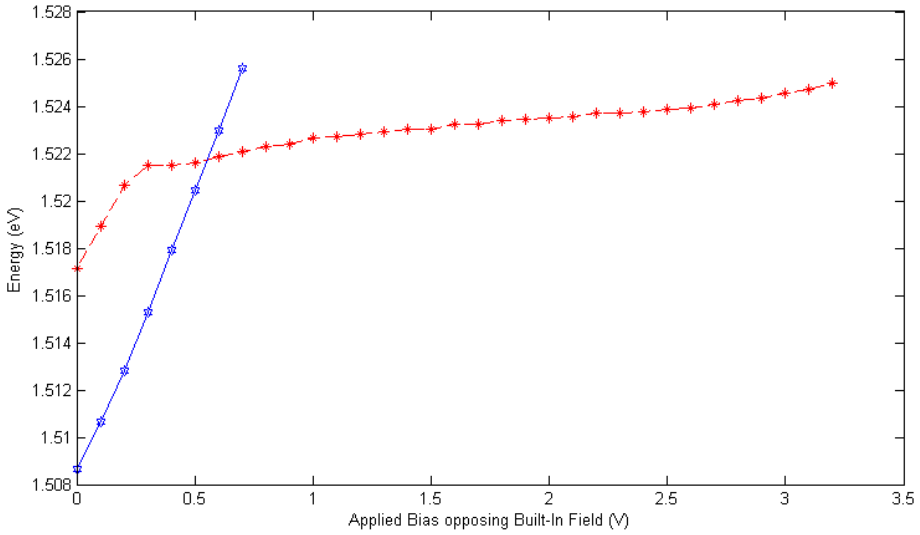

Figure 15: IX spectral peak energy vs applied bias, before (Red) and after (Blue) stress is applied and removed. The difference between the shifts is due to a change in the contact between the sample and mounting plates. After stress is applied to the sample, the sample-plate contact has a lower resistance, so that more of the applied bias is dropped across the well region. In addition, the shift becomes linear over the sampled bias range. Both sets of data were taken with an excitation power of 0.2 mW, at T=2 K.

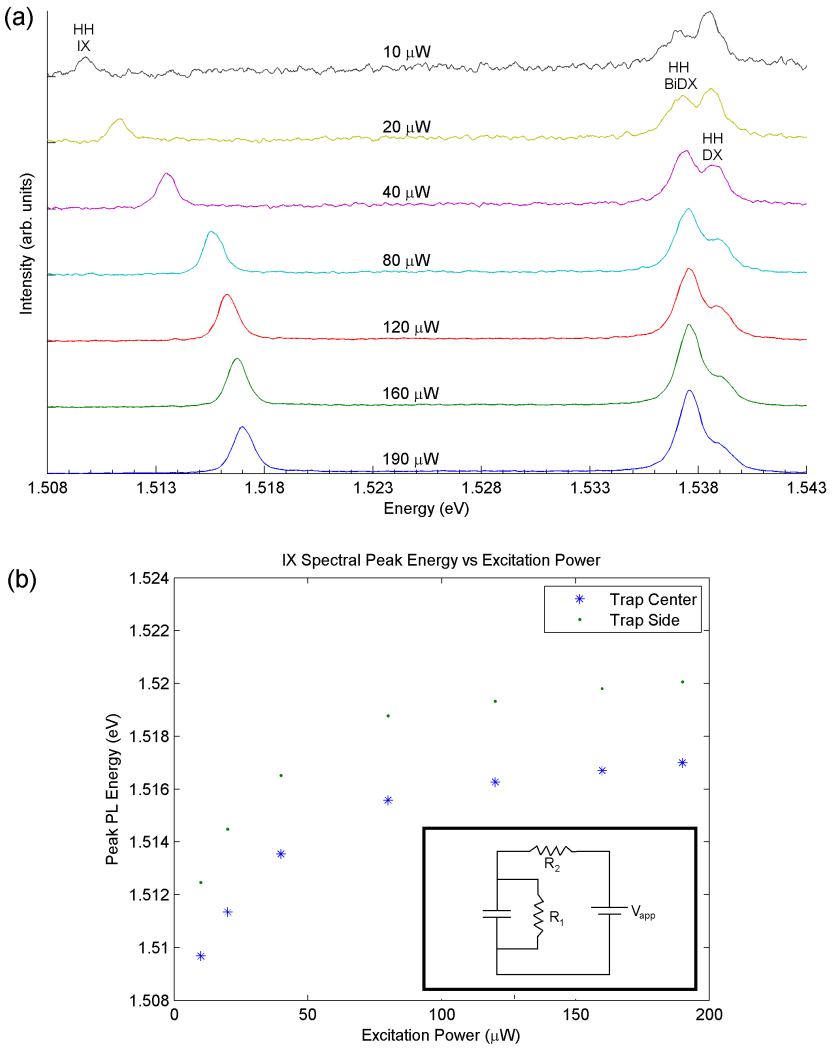

Figure 16: Modification of Stark shift due to varying excitation power. (a) Time-averaged PL spectra at varying excitation power. Each series' intensity is divided by the excitation power, displaying each on a similar scale, and displaced by a fixed value. The IX spectral line is seen to shift to higher energy with increasing excitation power, in a manner consistent with both a photocurrent-driven blue shift or a repulsion-driven shift. At high intensity, the BiDX line (lower energy line within the high energy pair) is observed to dominate the recombination. (b) The IX peak energy at the trap center and trap side in the same series. It is clear that the IX energy at the trap center and sides shift equally, inconsistent with a shift due to IX-IX repulsion. This indicates that the effect of increasing excitation power in this case is exclusively due to photocurrent. (inset) Equivalent circuit for quantum well biasing. The capacitor represents the conducting planes on the exterior of the superlattices. R_1 represents the resistance of the superlattice and CQW structure, and R_2 represents all external resistances, including contacts and current probe resistances. Generating free charges within the superlattice/CQW structure reduces R_1 and, consequently, reduces the voltage across the structure and the Stark shift in the CQWs. Sample Temperature: 5.0 K. Applied Bias: 0.8 V, reinforcing built-in field.

ciable resistance of the sample-plate contacts. Figure 16 shows an example of a situation when the photocurrent-driven shift is dominant over any dynamic blue shifts from IX-IX repulsion, and where this shift could easily be mistaken for a dynamic blue shift. There is a small stress applied, with a trap depth of about 4 meV, so that it is plausible that there could be a significant density-driven blue shift. From Figure 16(a), where the time-averaged spectrum through the trap center is displayed, it is impossible to tell the nature of this shift[4]. In this case, it is only clear that the increasing excitation power is shifting the IX emission to higher energy. However, in Figure 16(b), where the IX peak energy from two different positions in the trap, the trap center and a point on the periphery, are compared, it is clear that that shift is exclusively due to photocurrent. If the shift was caused by the IX density, the splitting between side and center energies would decrease with excitation power, as the trap flattens from IX-IX repulsion. The inset to Figure 16(b) shows a very simple equivalent circuit to represent the biasing conditions. Since the insulating superlattices block charges from flowing between the two conducting doped regions, on either side of the sample, the charging of the exterior of these regions is represented by the capacitor. The resistance of the interior of the superlattice and CQW structure is represented by R_1, and R_2 represents all exterior resistances, such as that of the contacts and the resistance used to probe the current flow. Optical excitation tends to reduce R_1. This modifies the voltage division so that less of the applied bias is dropped across the superlattice/CQW region, reducing the Stark shift of the IX states. Since the metallic layers on either side of the sample ensure that the field is constant across the sample, the DC shift (from photocurrent) causes a rigid shift of the entire trapping potential rather than a spatially-varying distortion. If the series resistance, R_2, is not extremely small compared to R_1, this DC shift will be appreciable. Traditionally, the identification of this shift in contrast to the dynamic blue-shift (due to IX-IX repulsion) relies on either 1) a temporal measurement demonstrating that the shift is not varying in time or 2) a comparison of the trap profile as a function of excitation power.

The series of spectra in Figure 16 were taken with a defocused laser at 770 nm, in order to enhance the photocurrent effect. Qualitatively, I can say that a focused laser, while still showing some DC blue shift with excitation power, generally seems to have a lower

[4]Although, one might be skeptical of such a large shift due to IX-IX repulsion in a trap only 4 meV deep.

photocurrent overall, most likely due to the excitation of fewer defect regions (e.g. regions of narrower barrier), though a systematic study of this phenomenon was not conducted. As mentioned in Section 3.1.4, excitation with a laser at a lower wavelength than 772 nm also dramatically increases the photocurrent, perhaps due to more efficient excitation of the superlattice states.

4.1.3 IX Dynamic Blue Shift

While we have demonstrated in the previous section that it is possible to observe a blue shift of the IX energy that is exclusively due to photocurrent modifying the built-in field, it is certainly not true that the repulsive effect is never observed. The previous situation with defocused excitation, lower-wavelength laser is, in fact, the exceptional case. It is similarly possible to observe a case where the excitation power dependence of the blue shift is completely due to the density-driven, dynamic blue shift with no measurably DC blue shift (due to photocurrent), e.g. this is often the case with high instantaneous excitation power and lower average power (low duty cycle) with a focused, resonant laser. The most common situation in our experiments is the intermediate case, where there may be some DC blue shift at the highest excitation powers and there is a dynamic blue shift (at early times) for all but the lowest excitation powers.

An example case demonstrating both a large dynamic blue shift and a large DC blue shift is shown in Figure 17. This time-resolved series has exposures 200 ns in length beginning at the time indicated above each image. The laser is on for 2 μs, after which the first image in this series is collected from 2 to 2.2 μs. The average laser power of 3.2 mW, is quite high for our experiments, and this first image makes it plain that the trap potential is completely flattened by the large IX density. As the IXs begin to decay, the dynamic blue shift decays as well, in accord with its origin in IX-IX repulsion. Since this data is collected from the same sample as that of Figure 17, with the same applied bias, a direct comparison of the IX energies makes it apparent that the very large excitation power is causing an even larger DC blue shift, in this case. However, the time resolution employed here allows differentiation of the DC photocurrent blue shift and the dynamic blue shift due to IX-IX repulsion. Of

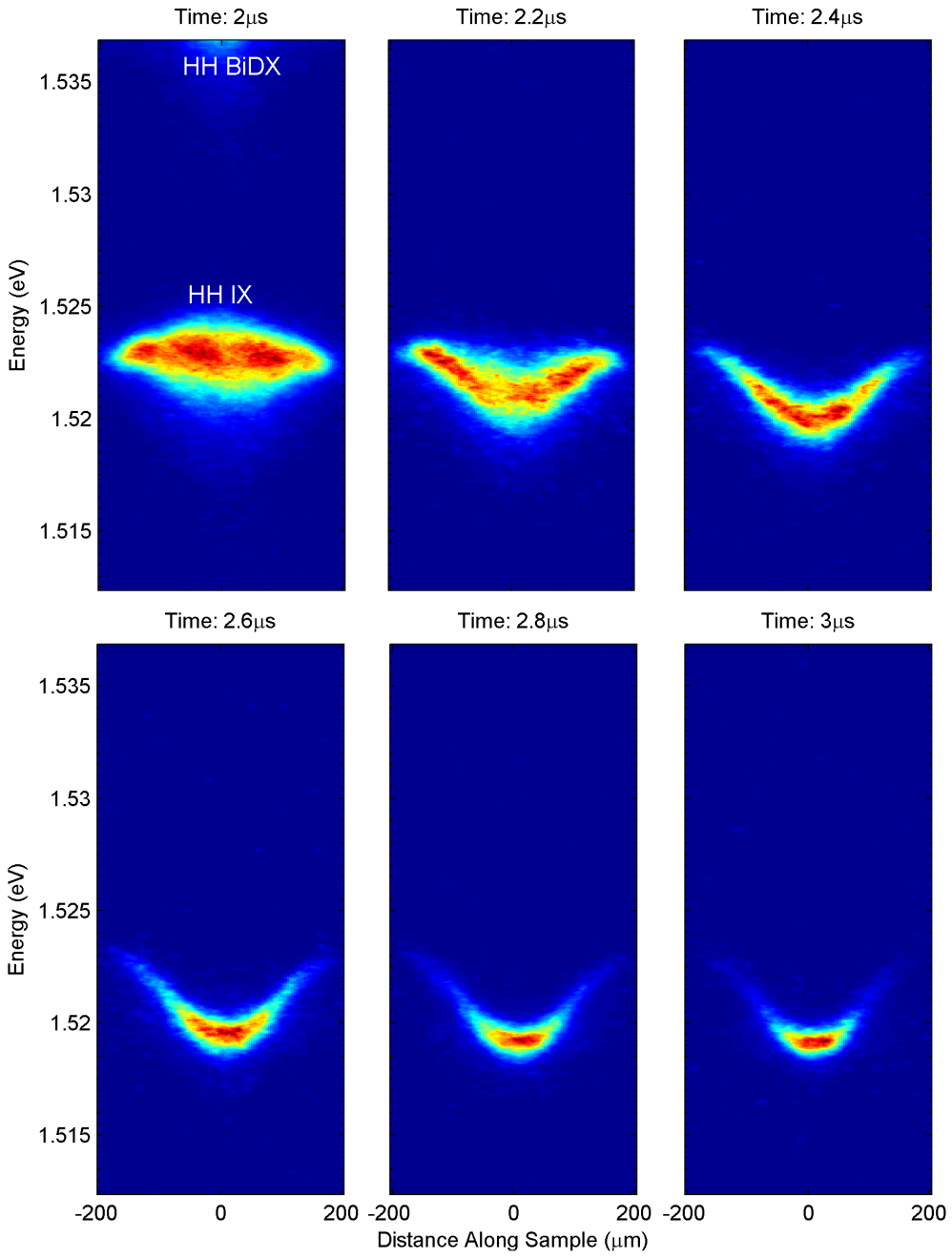

Figure 17: Time-resolved spectral images showing the dynamic blue shift. The excitation is again defocused to illuminate the entire trap region, but the laser is now resonant with the HH DX. The intensity color map is scaled for each image, in order to highlight the features of each. Sample has 12 nm wide wells. Temperature: 2.0 K. Applied Bias: 0.8 V. Excitation Power: 3.2 mW.

course, the photocurrent shift is not perfectly static, but it decays with a time constant much longer than the repetition rate of the experiment, so that it is effectively constant.

The lifetime of the IX population in Figure 17 is quite short compared to most of the experiments presented in this document (though still quite long for excitons in general), owing to the rather small electric field in the wells. The fact that there is not a single chemical potential across the entire trap (the spectral line is not at approximately the same energy for all positions, most clear in the top-right image at a delay of 2.4 μs) is due to the recombination time being shorter than the time required for excitons to diffuse across the trap region. It is particularly dramatic in this case of very fast recombination, but to some extent this can be seen in other images presented here. However, it is expected that when the lifetime is significantly longer than 2 μs, the time observed by Voros et al. [81] to see spatial equilibration in these samples, the spectrum at any given time should be essentially flat as a function of position in the trap.

4.2 HIGHER STRESS RESULTS AND LUMINESCENCE DARKENING

4.2.1 IX Trap Asymmetry

Increasing the stress beyond the range of previous experiments, we first observe a marked anisotropy of the IX PL spatial profile. As demonstrated in Figure 1 of the introduction, at elevated stress the intensity map becomes elongated in one direction. This corresponds to the [110] direction, which is indentified visually, as it corresponds to a cleaving axis of the GaAs wafer. Therefore, the elongated axis is always parallel to a wafer edge. We can map out the energy of the DX and IX states in order to determine the origin of this lengthening. Two-dimensional maps of the IX and DX energies are achieved by taking a series of spectral images. With the spectrometer slit aligned to some slice of the sample, the energies at each vertical position are fitted from all of the spectral peaks at that position. The image is then scanned across the slit, repeating this process for many slices and mapping out the energies at each point. This is demonstrated in Figure 18(a-b), showing energies of the DX and IX

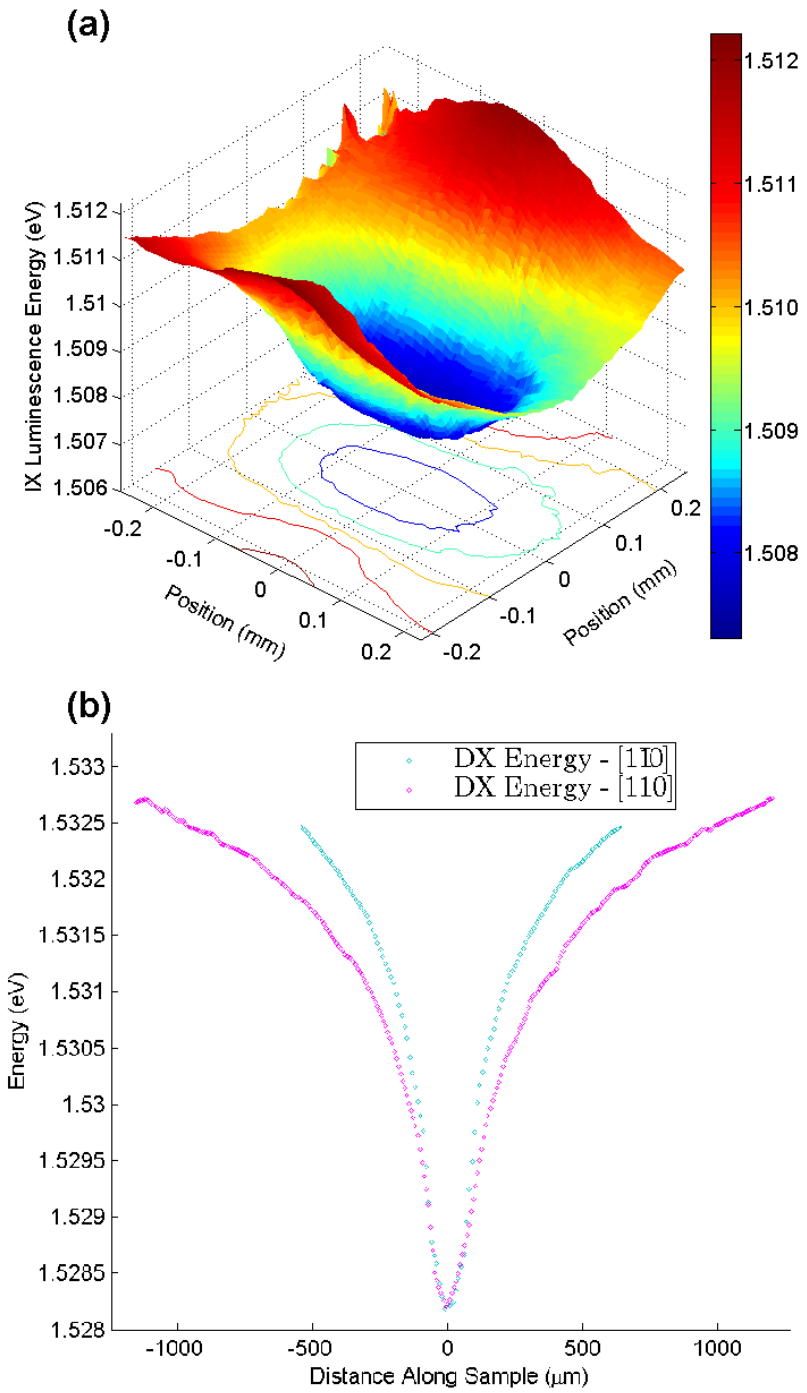

Figure 18: 2D energy profiles of IX and DX traps at stresses where darkening occurs. Spectral peaks are mapped from 40 spectral images, scanning across the sample. (a) Surface map of IX spectral peak energies. Iso-energy lines are projected onto the spatial axes to highlight the anisotropy and also to suggest the shape of an equilibrated high-density population. (b) Cross-sectional plots of HH DX spectral peak energies along the [110] and [1$\bar{1}$0] directions through the trap center, showing that the DX states also show the asymmetry between these directions but to a lesser degree.

states at high stress.

Figure 18(a) shows a surface plot of the IX energies. For mapping the IX energy, it is very important that excitation power is extremely low and that the IX has a short lifetime, so that no blue shift modifies the trap-center energy. Here, a defocused pump excites a 0.5 mm-wide region, so that the short-lifetime IXs (luminescencing at approximately their original excitation location) will illuminate more than just the center of the trap. It is clear that the IX trap becomes very anisotropic at high stress, exhibiting weak confinement along the [110] direction, and stronger confinement along the $[1\bar{1}0]$ direction.

Figure 18(b) similarly shows the results of mapping the DX energies at high stress in cross-sections through the trap center of the HH DX. Moving away from the trap center, the DX energy increases more slowly along the [110] direction than the $[1\bar{1}0]$ direction, just as in the IX case. However, this anisotropy is much smaller than that of the IX.

We can easily explain the large magnitude of the IX shift in contrast to that of the DX. The most salient difference between IX and DX states is the presence of a strong Stark shift in the IX case. So, the best candidate to cause the large difference in the shift between the states seen here is a spatially-varying electric field. Since GaAs lacks an inversion center, this could be caused by a piezoelectric polarization in the growth direction from ϵ_{xy} strain. Our simulations, shown in Figure 6, show that the ϵ_{xy} strain flips sign between the [110] and $[1\bar{1}0]$ directions and that it increases with distance away from the trap center. This is consistent with the observed trap anisotropy, if in the [110] direction the sign of ϵ_{xy} is such that the piezoelectric polarization augments the built-in field. In the [110] direction, then, the Stark (red) shift would increase moving away from the trap center, yielding a less steep trap profile. Similarly, in the perpendicular direction, the confinement is enhanced by a Stark shift reduction. Thus, we can refer to the [110] direction as the weak-confinement axis, and $[1\bar{1}0]$ as the strong-confinement axis. The DX asymmetry mirrors that of the IX state but to a lesser degree. Since the DX state can also be slightly polarized by an electric field, a piezoelectric polarization could potentially also explain the DX asymmetry.

The mapped DX, BiDX, and IX energies can be fitted using our strain simulation and the Pikus-Bir Hamiltonian to allow some rough constraints to be placed on the simulation parameters. The free parameters used in the simulation to determine the energy of each of

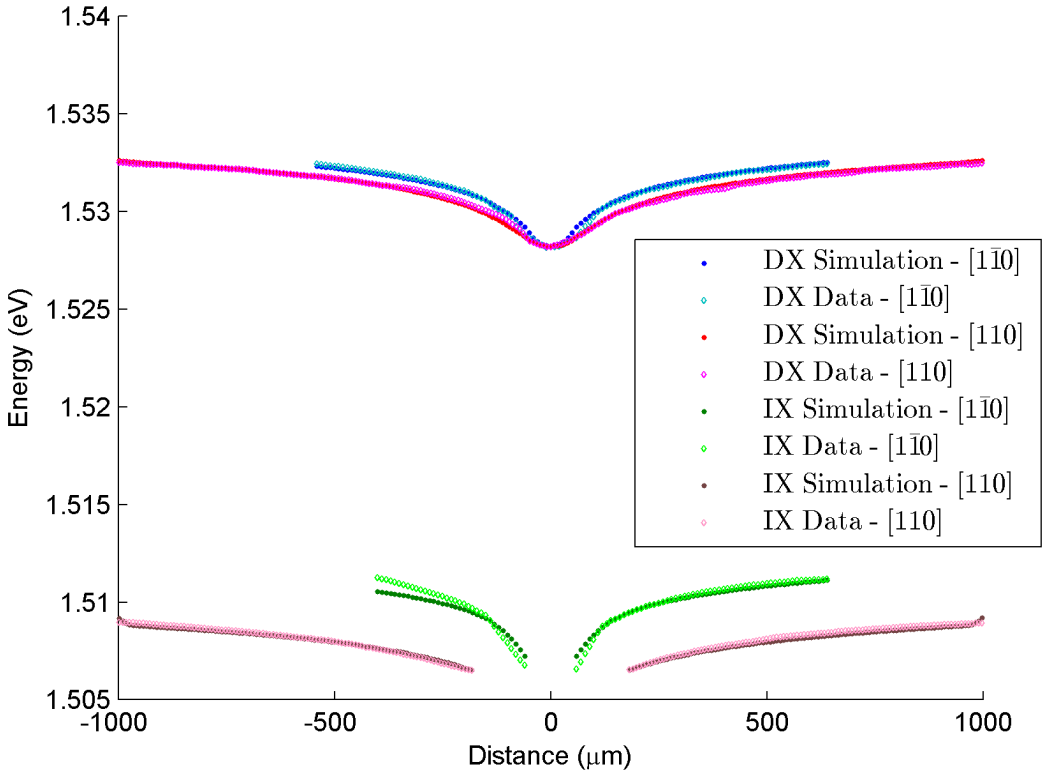

Figure 19: Fitting cross-sectional plots DX and IX energies along the [110] and [1$\bar{1}$0] directions through the trap center. The asymmetry along these two directions is modeled by allowing a Stark shift due to piezoelectric polarization and an offset to the off-diagonal strain ϵ_{xy}. Fit Results – Piezoelectric Constant: 5.0, $\Delta E^{IX}_{LH/HH}$= 11 meV, ϵ_{xy} offset: 0.00011.

the states are: 1) the Stark shift of the IX line, 2) the piezoelectric coefficient, 3) the applied force, 4) the unstressed IX HH-LH Splitting ($\Delta E^{IX}_{LH/HH}$) and 5) a constant ϵ_{xy} offset. The DX energy at zero stress is fixed from experimental observation, as is $\Delta E^{DX}_{LH/HH}$ (7.3 meV, here). The BiDX profile is predicted by simulating the DX and subtracting 1.3 meV, assuming that the only difference between these energies will be a constant binding energy difference.

The splitting, $\Delta E^{IX}_{LH/HH}$, is allowed to vary since the LH IX and HH IX Stark shifts are expected to be different. More precisely, the LH IX Stark shift should be smaller, further increasing the separation between these two states[5]. A constant ϵ_{xy} offset is essentially just a rough approximation for the effect of any unaccounted constant mixing between the LH and HH states. This mixing could certainly arise from other means than an ϵ_{xy} offset. However, since ϵ_{xy} from the applied force tends to be greatest along the [110] and [1$\bar{1}$0] directions, this seems to offer a convenient means to explain the asymmetry observed between these directions. This offset will add some mixing between the states at the trap center, pushing down the trap center energy. In addition, this offset will introduce an alternative source for the [110]/[1$\bar{1}$0] asymmetry than the piezoelectric Stark shift. This term is included to determine to what extent its inclusion/exclusion affects the fitted piezoelectric constant and quality of the overall fits. The applied force and Stark shift are going to vary greatly from experiment to experiment on a sample, but the piezoelectric constant should be constant within the same sample. In addition, the values gleaned for the strain offset and $\Delta E^{IX}_{LH/HH}$ would provide a helpful context for other experiments. While we expect $\Delta E^{IX}_{LH/HH}$ to depend on the electric field, it will vary quite slowly, in accord with the slight difference in the dipole moments of these two states. The mixing offset, which may arise from a number of causes, may vary greatly from experiment to experiment, as we are uncertain as to its origin, but proving its existence in a single experiment suggests that it likely exists to some extent in others.

Figure 19 shows the results of this fitting, plotting the simulation results, using the final parameters, on top of the experimental data for the DX and IX spectral lines along the [110]

[5]Later, in Section 4.2.6, $\Delta E^{IX}_{LH/HH}$ is directly observed to be 1.7 meV larger than $\Delta E^{DX}_{LH/HH}$ at zero applied bias, in the singular case where the IX LH spectrum was able to be observed. This does not fix the splitting at this value for all experiments, as this splitting is expected to vary with electric field, but it does further the argument that the IX splitting is generally larger than that of the DX.

and $[1\bar{1}0]$ directions. The IX data at the trap center is not included in the fit since the IX energy there is significantly blue-shifted due to the IX density, so it will not correspond to this prediction. In addition, the IX and DX data along the $[1\bar{1}0]$ direction seem to deviate strongly from fits on one side of the sample (the left side of the $[1\bar{1}0]$ plots). This left side of the data was not included in the fits, but is included here to illustrate the deviation. This overall slope is typically the result of the stressor pin hitting a point away from the center of the hole below the sample, a situation which is not allowed in our simulation. The fitted piezoelectric constant is 5.0. The value of $\Delta E^{IX}_{LH/HH}$ is not well determined by this fitting, as the fits are fairly insensitive to this value. In addition, the initial state splitting and piezoelectric constant have very similar effects on the data[6], so it is difficult to independently determine either value. The fit plotted in Figure 19 uses 11 meV for this splitting, but it would look nearly identical for values above 6 meV. Previously, we reported [69] this value to be 4.7, using the results of a similar fitting that held the IX splitting to be the same as that of the DX states. With this data set, constraining the IX splitting to 7.3 meV yields 4.8 for the piezoelectric constant, consistent with our previous results.

In addition, the fit was run again without an ϵ_{xy} offset. Removing this term, the DX anisotropy is not large enough in the simulation to match the data, i.e. the splitting between the DX states along the [110] and $[1\bar{1}0]$ directions is too large, by about 0.2 meV, in the data to be accounted for by the piezoelectric Stark shift of the DX states. We have not included the Stark shift of the DX states as a free parameter. Instead, our data in this sample suggest that, in this range of electric field, the DX state shifts by roughly a factor of 14 lower than the IX Stark shift, and this Stark shift is included for the DX states in the fits. If the DX Stark shift is allowed to be much larger, increasing it from 7% of the IX shift to 20% of the IX shift, the DX asymmetry can be accommodated with no offset strain. However, it is unlikely that the measurements of the DX Stark shift are off by this degree. Hence, it is unlikely that the DX Stark shift can wholly explain the asymmetry, and we require a very small amount of offset mixing to account for the asymmetry. In this case, the 0.011% ϵ_{xy}

[6]Both the piezoelectric constant and $\Delta E^{IX}_{LH/HH}$ tend to change the asymmetry between energies along the [110] and $[1\bar{1}0]$ directions. Increasing the piezoelectric constant increases the energy difference along these directions. Similarly, decreasing the splitting between the LH/HH states causes increased repulsion between these valence-band states. This also increases the energy discrepancy between the states measured along the two different directions.

strain fits the data well for the prescribed DX Stark shift[7].

4.2.2 Darkening of Trap-Center Luminescence with Increasing Strain

As shown in Figure 20, upon further increasing the stress, the luminescence darkens at the trap center, where the density should remain greatest. Figure 20(a) is a reproduction of Figure 1, displaying this darkening occuring in spatial images of the IX PL from a sample with 12 nm-wide wells at a temperature of 2.2 K. The excitation is focused at trap-center and nearly resonant with the HH DX. With increasing force, the IX profile becomes increasingly extended in the horizontal direction (the weak-confinement axis), eventually developing a darkened center at the highest stresses. The luminescence pattern overall becomes spread over a larger area of the sample. The color maps in this series are consistent between images, so we observe that the intensity is actually darkening at the trap center with increasing force. We see in the last image in this set that there is a striking contrast in the shape of this dark spot and the shape of the trap and IX density. It does not seem to have inherited the large anisotropy of the IX system.

Figure 20(b), a similar sequence in a sample with 14 nm wells, shows spectral images through the trap center (along the weak-confinement direction) with increasing force. Directly observing the IX spectral line, it is clear that it is indeed the IX state that darkens. At the highest stress with pronounced darkening, the total stress-induced shift of the DX line is 5 meV from its unstressed position. In both image sets in this figure, the camera is gated to collect the entire interval after excitation, so the images represent a time-average of the IX PL over 6 μs.

The forces quoted in the spatial images are inferred from the compression of calibrated springs. However, these springs are in our original stressor design, in which the springs are external to the cryostat and the spring-driven rod must pass through an o-ring seal to reach the sample. Therefore, we must take the actual values of these forces with some degree of uncertainty, as there is likely a good deal of this force removed by the static friction of the o-ring.

[7]Increasing the DX Stark shift to 10% of the IX shift, requires a 0.0085% strain offset to fit the data. Decreasing the shift to 5% of the IX shift, requires a 0.012% offset strain.

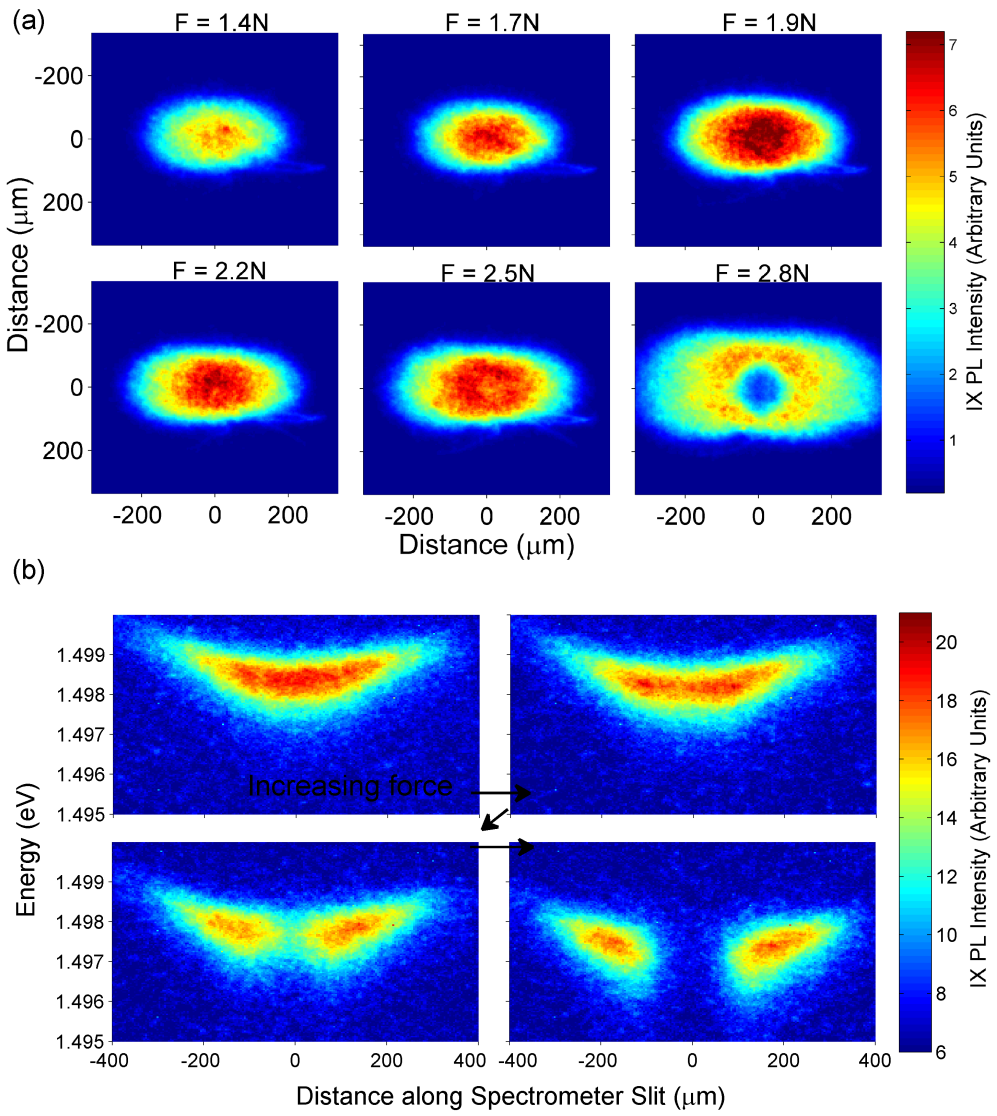

Figure 20: Spatial and spectral images of IX PL with increasing force applied to sample. (a) Spatial images of IX PL as the darkening occurs. The applied forces are inferred from the compression of calibrated springs, external to the cryostat body. This sample has 12 nm wide wells. T=2.2 K; The excitation had P_{avg}=120 W, focused at that the trap center, with an energy 4 meV above the HH DX absorption at the trap center. Applied Bias = 0.50 V, augmenting the built-in field. The horizontal axis (with weaker confinement) corresponds to the [110] crystal axis, and the vertical axis corresponds to $[1\bar{1}0]$. (b) Spectral images of IX PL during the transition. The slit is aligned along the elongated axis. This series is performed with a different sample than above, with 14 nm wide wells. P_{avg} = 2.4 mW. Applied Bias = 0.0 V. T = 2.1 K. In both upper and lower series, the camera was gated to capture the entire decay after end of excitation pulse.

As demonstrated by the different samples in these two image sets, this pattern has been reproduced in samples with varying well widths (8-14 nm). The strain at which the pattern first appears is consistently lower as the well width is increased. The primary effect of varying the well width is a modification of the LH/HH splitting due to the confinement, but there are a number of different effects associated with this change,e.g. decreasing disorder potential height, a concomitant increase in mobility with increasing width (if limited by interface roughness scattering) [63], and a change in the effective hole masses [5, 85, 62].

4.2.3 DX Darkening

In addition to the IX darkening with increasing stress, the DX state is also observed to darken. Figure 21 shows three spectral images with increasing force, all taken with the CCD ungated to allow observation of the DX and BiDX states. The DX darkening occurs at a slightly higher stress than the IX darkening. In all of the images, the IX darkening is present, while the DX state at the center of the trap begins darkening in the second image. In contrast to the darkening in the IX case, there is no higher stress at which the DX PL again brightens at the trap center. This behavior seems to be consistent with the LH DX state crossing to become the lowest energy DX state. The LH DX state should have a lower recombination rate for the same reason that the LH IX state has a high recombination rate – the lower growth-direction mass causes more penetration of the light hole into the barrier. So, rather than becoming bright when the LH DX becomes the lowest state, it should become dark. Section 5.1.6 contains a quantitive evaluation of this supposition.

4.2.4 Relative Darkening of Trap-Center Luminescence with Increasing Density

In addition to increasing strain, we observe that at a fixed high strain, this effect appears with increasing density. We have previously published [69] images showing the appearance of this effect with increasing excitation power. Due to the ambiguities associated with varying the excitation power between images (varying photocurrent/Stark shift), Figure 22 displays a series of intensity profiles (cross-sections along the weak-confinement axis) that does not rely on varying the excitation power. Here, the excitation laser is on from t=0 to 7 μs, and

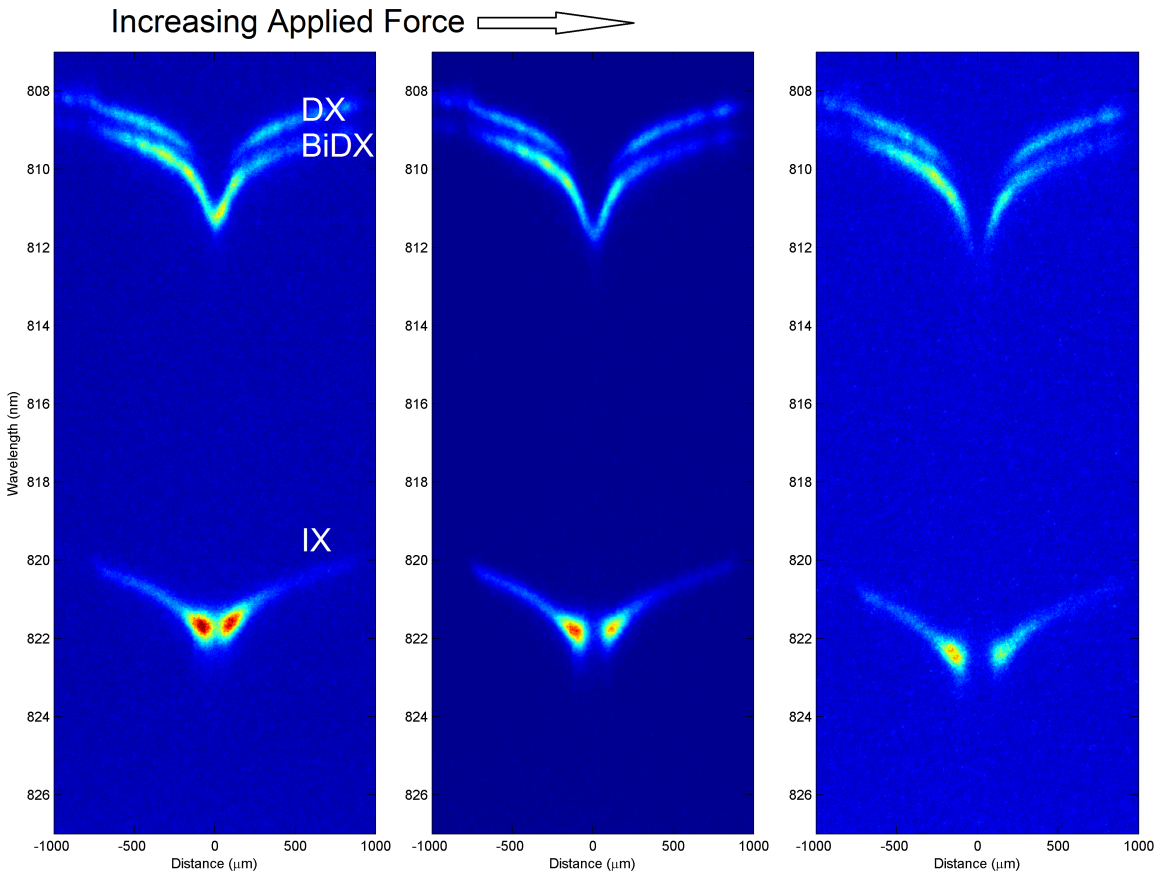

Figure 21: A series of spectral images showing darkening of the DX PL at the trap center with increasing force. At a slightly higher applied force than required to produce IX darkening, the DX center also darkens.

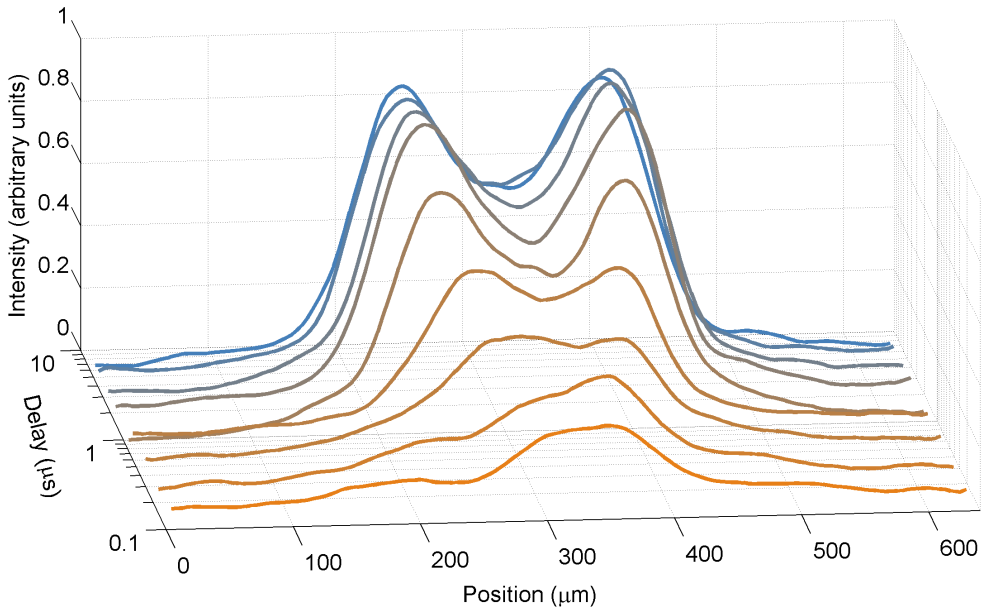

Figure 22: Time-resolved series showing the darkened center appearing as the population grows. The IX PL is collected over short intervals as the population grows throughout a long excitation pulse. The time is displayed on a logarithmic scale. As the total exciton population grows, the center intensity appears to saturate, while the intensity on the periphery continues to grow.

the repetition period is increased so that the population decays substantially between pulses. Gating the camera to collect images throughout the excitation period, we see the population grow with time. At very early times, the IX profile is singly-peaked at the trap center, but the intensity quickly develops a dip at the trap center. The DX intensity profile (not shown) remains peaked at trap center for the entire range. The displayed intensity profiles are not normalized, so we can directly compare between them. We see in this case that the "darkening" of the center luminescence does not actually occur in an absolute sense, in contrast to the stress-induced case where the intensity actually decreases in the center. Here, the dark center pattern emerges as the luminescence in the center seems to saturate, while the sides continue to grow. From this difference in character of the effect, we surmise that the fundamental nature of this pattern is not necessarily a darkening of the center but only a relative darkening. The actual darkening with increased strain is caused by an additional effect.

It is perhaps not obvious in Figure 22, due to the perspective, that the peak positions are moving slightly farther outward as the density increases. This trend continues as the density is increased, but the density in this series is limited by the equilibrium density of the system ($N_{eq} = G\tau$), where G is the exciton generation rate.

Furthermore, this appearance of the intensity patterning by only increasing the density rules out a strain-induced, higher-energy bump at the trap center. This is important, as it is likely the first conclusion that springs to mind in looking at, for example, Figure 20(a), where the exciton cloud just seems to be pushed away from the center. We can discard this explanation because at lower excitation power, we see the trap to be perfectly well-behaved, showing the typical harmonic trap profiles (though, different with different harmonic trap constants in the weak and strong confinement directions). The 2D profile of Figure 18(a) is an example of this behavior, as, at high density, the dark center pattern is observed in that trapping potential.

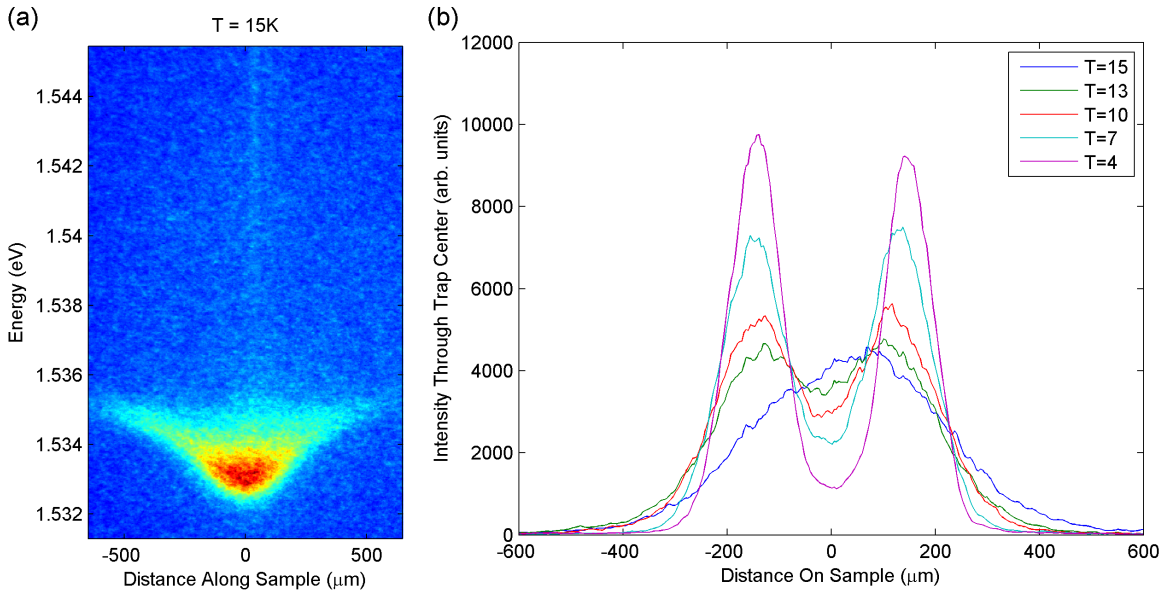

Figure 23: Disappearance of the intensity pattern with increased temperature. (a) Spectral image through the trap center at 15 K, in a trap that shows a darkened center at lower temperature. The spectrometer slit is aligned to the weak-confinement axis. The entire decay is collected without CCD gating. (b) Intensity cross-sections through the trap center at varying temperature. Apart from the temperature, these profiles were collected under the same conditions as the spectrum in (a).

4.2.5 Hole-Pattern Transition with Varying Temperature

In order to complete the picture, the temperature dependence of this phenomenon was explored. The pattern of relative darkening at the trap center disappears at elevated temperature. In Figure 23(a), a spectral image of the IX PL is displayed at 15 Kelvin, showing a cross-section of the luminescence through the weak confinement axis. At this temperature, the intensity is singly-peaked at the trap center. Figure 23(b) shows intensity cross-sections of the IX PL in the same trap as the temperature is decreased from this point. The pattern begins to appear abruptly just below T=15 K, with the contrast between the trap periphery and center increasing as the temperature is lowered.

The cross-sections in Figure 23(b) are actually cross-sections of the spatial images, not spectrally-resolved. There is, however, a bandpass filter present in the imaging system during the collection of these cross-sections, so we can be certain that we are only collecting the IX spectral range and not also the DX or laser. Furthermore, from the spectral image on the left, we observe that the darkening pattern seems to disappear from the IX PL spectral line itself; it does not require the thermal excitation of any distinct states. In particular, we don't see a spectrally distinct LH IX becoming illuminated at higher temperature.

The temperature and density dependence of this transition was previously plotted in the dissertation of Z. Voros [78] in our initial investigation of this phenomenon. I will not reproduce the analysis of that data here, but simply state the conclusions. In that data set, we discovered that the density at which this pattern appeared (specifically, when intensity of the center first become lower than the sides) increases with increasing temperature. That analysis plotted the transition density vs temperature alongside a plot of the critical excitation power for 2D (non-interacting) BEC in a harmonic trap ($N \propto T^2$), showing that at low density the transition temperature seemed to follow this prediction. In addition, this analysis for two different stresses showed that the critical temperature at a particular excitation power was higher for deeper traps. This is qualitatively consistent with the critical temperature dependence on the harmonic trap frequency.

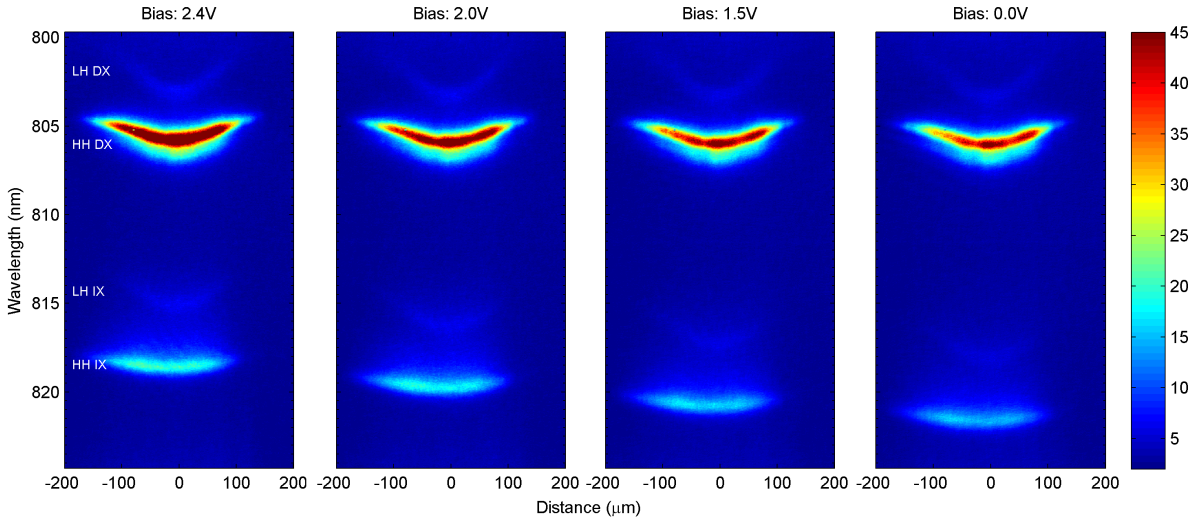

Figure 24: Series of spectral images with varying bias, displaying LH IX at low stress. The bias is applied opposing the built-in field. The sample temperature is elevated, with its actual value unknown due to the apparent mismatch between the sample temperature and the cold-finger sensor in this microscope cryostat. The large bias values and corresponding small Stark shift are due a large resistance in the sample contacts in this setup.

4.2.6 Direct Observation of LH IX Luminescence With Microscope Cryostat

In our typical experimental setup, luminescence from the LH IX state, which should be lower in energy than the HH DX state but higher than the HH IX state, was never observed, even at elevated temperature. Attempting to see this spectral line, we mounted a 14 nm-wide quantum well sample in a microscope cryostat, where the shorter working distance allowed a larger numerical aperture and increased collection efficiency. In addition to simply collecting more light, the emission pattern of the LH should be peaked away from the sample normal, since, in contrast to the HH case, the electric dipole moment is not oriented wholly in the growth direction[8]. So the larger collection angle is even more important. This cryostat is typically used for experiments creating stress traps for polaritons, and, to this end, it has a modified back cover that allows stress to be applied by a spring-loaded pin, driven by an external micrometer, in a similar manner to the original stressor assembly described in Chapter 1. We were able to briefly borrow this cryostat, allowing us to verify this prediction.

Figure 24 shows stressed, ungated spectral images through the trap center with this experimental setup with varying applied bias. The LH IX spectral line appears to be just above the HH IX PL. In addition, it has a steeper energy profile than the HH IX, in accord with the prediction that the LH should shift more with strain than the HH. In order to verify its nature, the bias is varied to display the Stark shift. As the series shows, the Stark shift is very similar to that of the HH IX state. In addition, the shift of the HH IX is always slightly larger than the LH IX, in accord with the prediction that the LH IX should have a smaller dipole moment. However, there are too few data points over too small a range of fields to indicate the magnitude of the difference in the slope of each shift. In addition, the varying dynamic blue shift in these images, as the lifetime(density) varies with bias, causes the total shift (HH DX to HH IX) to differ from the Stark shift prediction. We also observe that the LH/HH splitting in the DX states is always less than the splitting of the IX states (the difference in the splittings is 1.7 meV at zero applied bas). This also supports the theoretical prediction of a larger Stark shift of the LH IX, i.e. in Figure 3. This point is emphasized, here, because this prediction of a smaller Stark shift for the LH IX is directly linked to the

[8]See Chuang, Section 9.5.2[15]

prediction that the LH IX state has a larger oscillator strength[9].

This cold-finger cryostat was unable to maintain the sample at low temperatures. Despite the cold-finger measuring 4 K, the sample temperature is clearly well above this. In addition, the sample-plate contact had a very high resistance, such that only a small fraction of the applied bias was applied across the wells (as can be seen from the magnitude of the applied bias in the figure). So, in practice this cryostat turned out to be unsuitable for the IX experiments in general. However, it did provide the only direct observation of the LH IX photoluminescence when the LH IX is well separated in energy from the HH IX.

4.2.7 Measurements Regarding Indirect Exciton Loss, Lifetime, and Density in the Darkening Regime

Since the darkening could easily be caused by a loss of excitons in this region, we made some measurements to determine if there is some change in the efficiency of our experimental system or if there is a change in the carrier lifetimes when the dark center occurs. Figure 25(a) displays the total collected IX luminescence as a function of excitation power at a stress where the dark center pattern appears with an excitation power of 170 μW. Below this power, it shows a centrally-peaked pattern. For this series, the laser is focused at the trap center, but the IX luminescence is exclusively collected. This is achieved in the same manner as in lifetime measurements, by summing all first-order diffracted light in the IX spectral range, with the spectrometer slit open to collect the entire exciton cloud.

With the measurement of total intensity vs excitation power, we are primarily demonstrating that we are collecting a constant fraction of the excited IXs. The linearity of the total collected counts with excitation power rules out two possible causes of the darkening. First of all, we can rule out that increasing IX density causes some new non-radiative recombination channel or carrier loss mechanism. Second, we can discard the possibility that our IX collection efficiency is changing with increasing density. While this may sound unlikely, it is plausible if LH excitons recombine more often into photons directed at an angle from the sample normal. So, for example, the high density does not excite LH IXs at the center,

[9]To reiterate the point made in Sec. 1.3, the LH penetrates more into the barrier, causing both a smaller dipole moment of the LH IX and an increased electron-hole overlap.

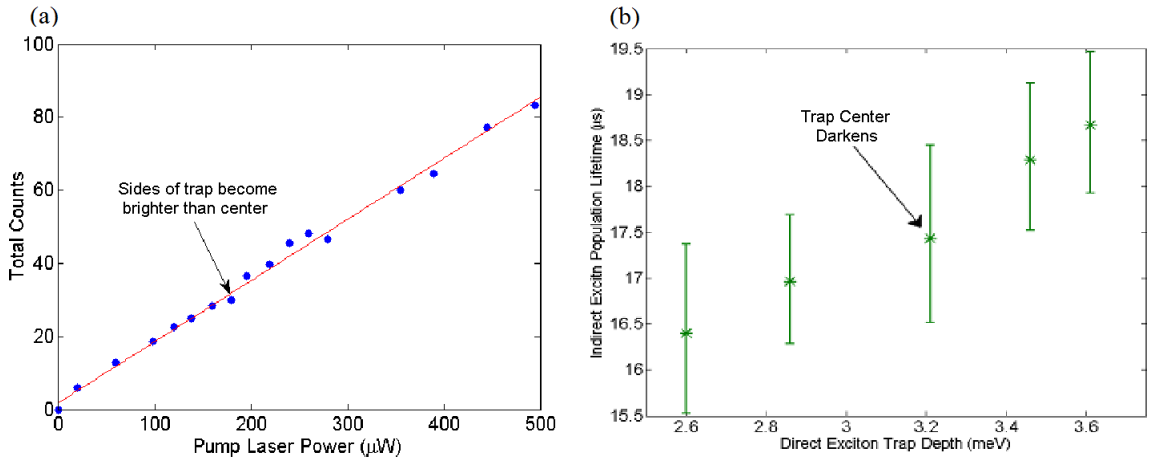

Figure 25: Variation of total intensity and lifetime with onset of darkening. (a) Total collected IX luminescence as excitation power increases. A dip in the trap-center PL is first observable at P = 170 μW. No significant deviation from the expected linear growth is observed, despite the patterning onset. (b) IX lifetime with increasing stress. The lifetimes are the decay constants resulting from single-exponential decay fits. The stress is indicated by the DX trap depth at each stress. The trap depth is indicated here consistent with that published previously [69], however these trap depths measure the energy of the trap bottom with respect to the DX trap energy at a distance of about 400 μm from the center, indicative of the depth of the region with a steep trapping potential. The total DX shift from its unstressed energy is actually larger than this; the largest total shift is 7 meV in this series. For both images, the total IX intensity is measured by summing all first-order diffracted light in the IX spectral range, with the spectrometer slit open to collect the entire exciton cloud.

while the experiment simply misses their luminescence.

Figure 25(b) displays the measured lifetime of the total IX PL, the decay constants from single-exponential fits, with increasing strain on the sample, as indicated by the increasing trap depth of the DX line on the horizontal axis. Contrary to what one might expect if the darkening were related to a shortening of the lifetime, the fitted IX lifetime grows slowly with increasing applied stress. A dip in the intensity profile at the trap center occurs in the third point in this series. This data was published previously [69], where I argued that the increase in this lifetime ruled out the possibility that some new loss mechanism emerges with strain to deplete the the trap center luminescence. Due to the long lifetime of this decay, only about 1 lifetime of the decay was observed in this series. The error bars indicate the 95% confidence interval to the fitted parameter, and they are relatively large. While the trend of increasing lifetime maintains intact even at the edges of the confidence interval, we could do a good deal better than this analysis by observing more of the decay.

Under similar conditions, this experiment was repeated with significantly longer experiment durations, allowing more of the decay to be observed. Figure 26(a) shows the decays for varying trap depth out to 90 μs after the end of excitation. The data are labeled by the corresponding DX trap depth at each applied force, as this can be directly measured. Here, this trap depth is measured by the total shift of the DX line from its unstressed energy, in contrast to the DX trap depths published previously and displayed in Figure 25(b), where the depth of each DX trap is measured as the relative energy between the trap center and a point 400 μm from the center. This accounts for the much larger energies reported in Figure 26(a). At early times, the decay rates are very similar for the various trap depths. However, the rates begin to diverge at a delay of 25 μs, where the higher stresses show a much slower decay beyond this time. Fits to the late-time decays for the lowest and highest stress cases are displayed. For the lowest strain, this decay rate also fits the early-time behavior well. However, the decay rate of the highly-strained case deviates strongly from its early-time decay. Figure 26(b) plots the fitted lifetimes for the first 25 μs of the decays (early lifetime) and for times after 30 μs (late lifetime). Under these lines, the insets show the time-integrated spatial profile of the IX PL for most of these traps. First of all, it is confirmed that the early and late decay of the lowest-stress case are consistent with a single

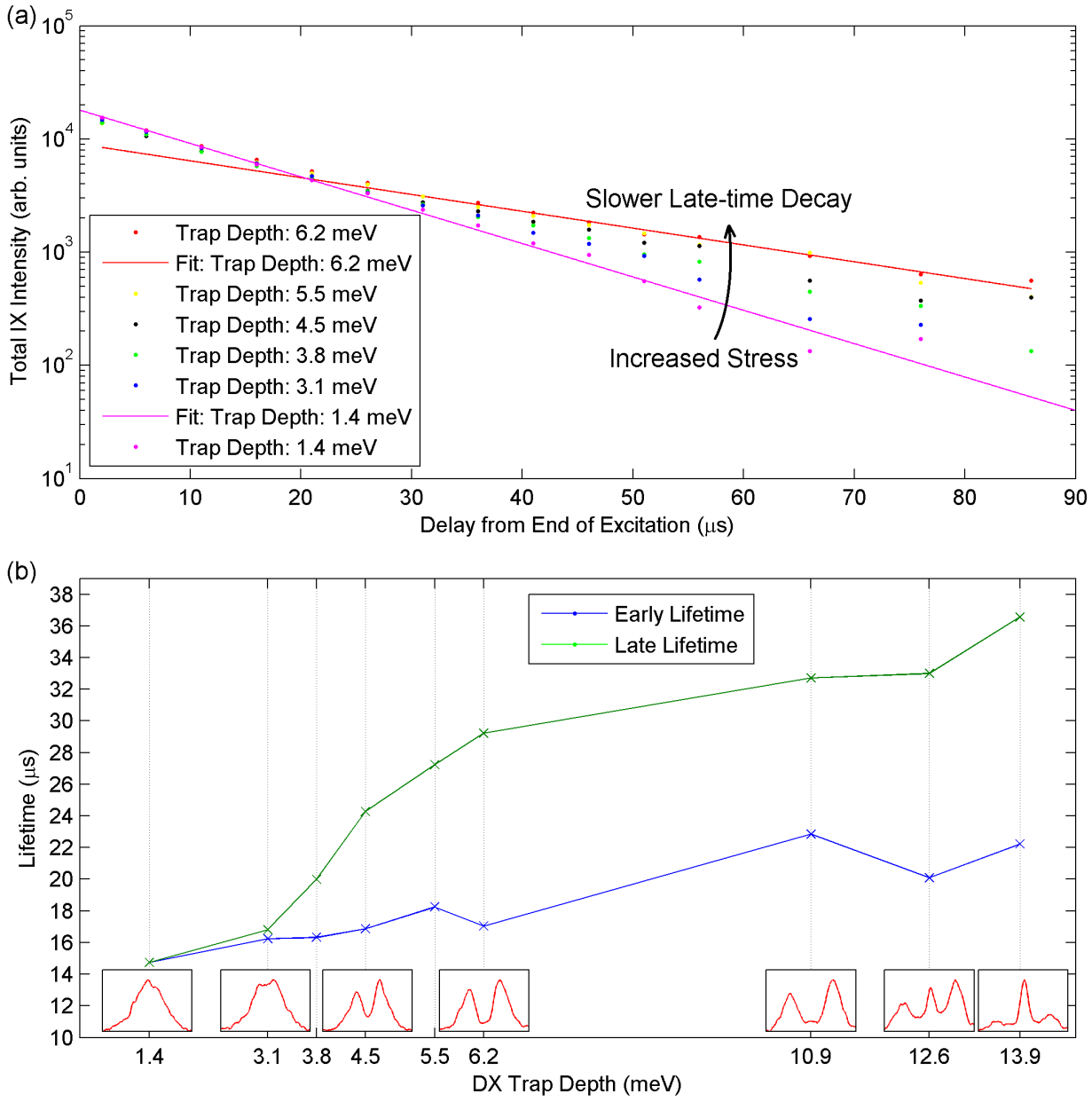

Figure 26: Fitting IX PL decay at early and late times separately with increasing strain. (a) The total IX PL intensity decay is plotted on a log scale, with varying trap depth. The lines are labeled by the DX trap depth, measured by the total shift of the DX PL peak from the unstressed DX energy. Shortly after the excitation ends, the decay rate is very similar for all trap depths. After about 25 μs, the decay rates of the highly-strained systems decrease dramatically, showing longer lifetimes with increasing force. Two single-exponential fits are shown for the late-time decays at the highest and lowest strains, where only points after 25 μs are fitted. (b) Single-exponential lifetimes vs DX trap depth at early and late times. The decay constants were fitted for each decay for delays 0 - 25 μs (Early Lifetime) and, delays 30-90 μs (Late Lifetime). The insets show the time-integrated spatial profile of the intensity for most strains.

exponential lifetime. In this case, it is about 15 μs. The second lowest strain shows only a slight widening of the spatial profile and a slight increase of the lifetime at late times. Increasing the stress begins to darken the trap center, while the late lifetime becomes increasingly longer, reaching up to 36 μs in the highest stress measured in this series. The highest three stresses show the re-brightening of the trap center. Interestingly, the trend of increasing lifetime continues throughout this transition, both in the early and late-time decays. So, there is no evidence that the high-stress brightening of the central PL results in an increased radiative rate, and, therefore, it reflects only a relative brightening of this region with respect to the rest of the trap region.

Revisiting the intention of this measurement, to determine whether it is possible that a new decay channel is introduced, the data indicate that this does not occur. It seems, rather, that the dominant decay channel becomes less effective as the stress is increased.

We can employ an indirect measurement of the density to show that the density actually remains largest at the center of the trap. It has been experimentally determined that there is a monotonic dependence of the IX spectral linewidth on the local IX density, due to IX-IX scattering [80]. If we take any spectral image of the IX PL with a darkened center and extract the FWHM across the trap, we can infer a density trend from the variation of the width. Figure 27(a) displays the image used for linewidth extraction taken at a temperature of 2 K. The camera is gated 3.5 μs after the end of the excitation for 400 ns (short to remove any artificial broadening from decaying blue-shifts). Figure 27(b) displays the total intensity and FWHM of the IX spectral peaks at each position. Despite the considerable noise in this measurement, the trend clearly indicates that the FWHM is largest at the trap center, where the intensity is dimmest. This is consistent with the IX density remaining largest in the center, despite its dimness. It is also consistent with any other mechanism that would cause increased IX scattering at the trap center that does not rely exclusively on strain, e.g. the accumulation of defects etc., because the linewidth is observed to decrease with varying intensity[10]. If there were a very large population of excitation-induced free carriers or phonons in this region, it would also cause a broadening of the IX linewidth. However,

[10]Looking at several linewidth profiles at varying times in this decay shows that the trend of FWHM at the trap center remains intact throughout the decay, but the magnitude decreases with total N.

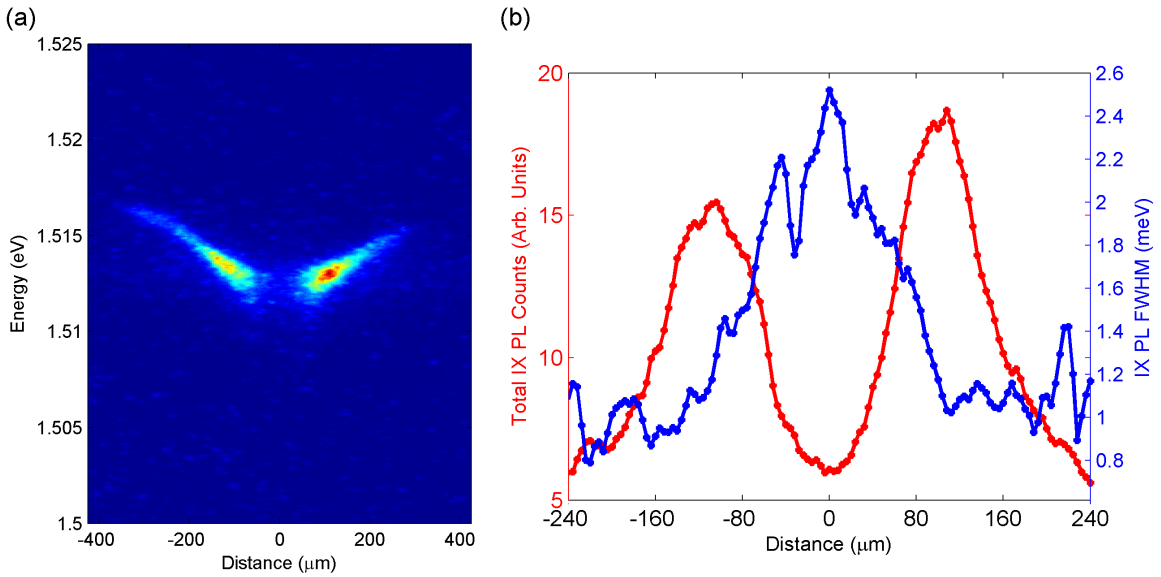

Figure 27: Spectral linewidth vs position with darkened center. (a) Image of the IX PL used for extraction of the linewidth. T = 2.0 K, Pavg=2 mW, Bias=1.0 V, augmenting built-in field. (b) FWHM and Intensity vs Position. The spectrally-integrated IX intensity is plotted in red (left axis), and the FWHM of the IX spectral peak is plotted in blue (right axis), displaying the discrepancy between the two quanitities..

one might also expect the DX line to be similarly broadened, which does not occur, and the sole broadening of the IX line suggests it is due to IX scattering, which is only strong for other IXs.

4.2.8 LH IX Luminescence at Trap Center at Very High Stress

Increasing the stress applied to the sample far beyond the point of initial darkening[11], we observe a wholly new luminescence pattern from the trapped population. The first evident change is in the IX spectra at high temperature. Instead of the "hole" in the IX PL simply closing with increasing temperature, as in the case at lower stress (see the high temperature spectrum in Figure 23), at this high stress, a higher energy state becomes thermally excited at the trap center. Figure 28(a) displays a high-temperature spectral image of the IX PL at this high stress. The excited state is clearly at a higher energy than the rest of population, and it occurs at the center of the still-darkened IX PL. This image is gated to show a relatively short time slice (2 μs long) after 2 μs have elapsed since the end of excitation, so it roughly represents the PL intensity at thermal equilbrium (though the total intensity decays by about 30% during the exposure interval).

The remaining images in Figure 28 display the characteristics of this luminescence as the temperature is increased up to this point. Figure 28(b) shows cross-sections of the spectrally-integrated IX PL. The LH IX state is thermally-activated, only appearing in the PL at increased temperature. The intensities are not normalized, so we can observe that the sides are dimming as the center grows brighter. Figure 28(c) and (d) display cross-sections of the peak energy and linewidth, respectively, resulting from fitting the IX spectral peaks. The peak energies show that the trap center luminescence begins to predominantly come from a state at higher energy. Unfortunately, the dimness of the lower energy luminescence along with the complex lineshape at high temperature prevents picking out two distinct spectral peaks at a particular temperature. However, the LH IX decay clearly begins to dominate the trap-center luminescence at T$\geq$5 K, as the spectral peak shifts abruptly upward at

[11]The two regimes can be easily distinguished. If we trust the relative force from the calibrated springs, in samples with 14 nm wells, this change occurs with about 40% more force applied to the sample than the darkening transition.

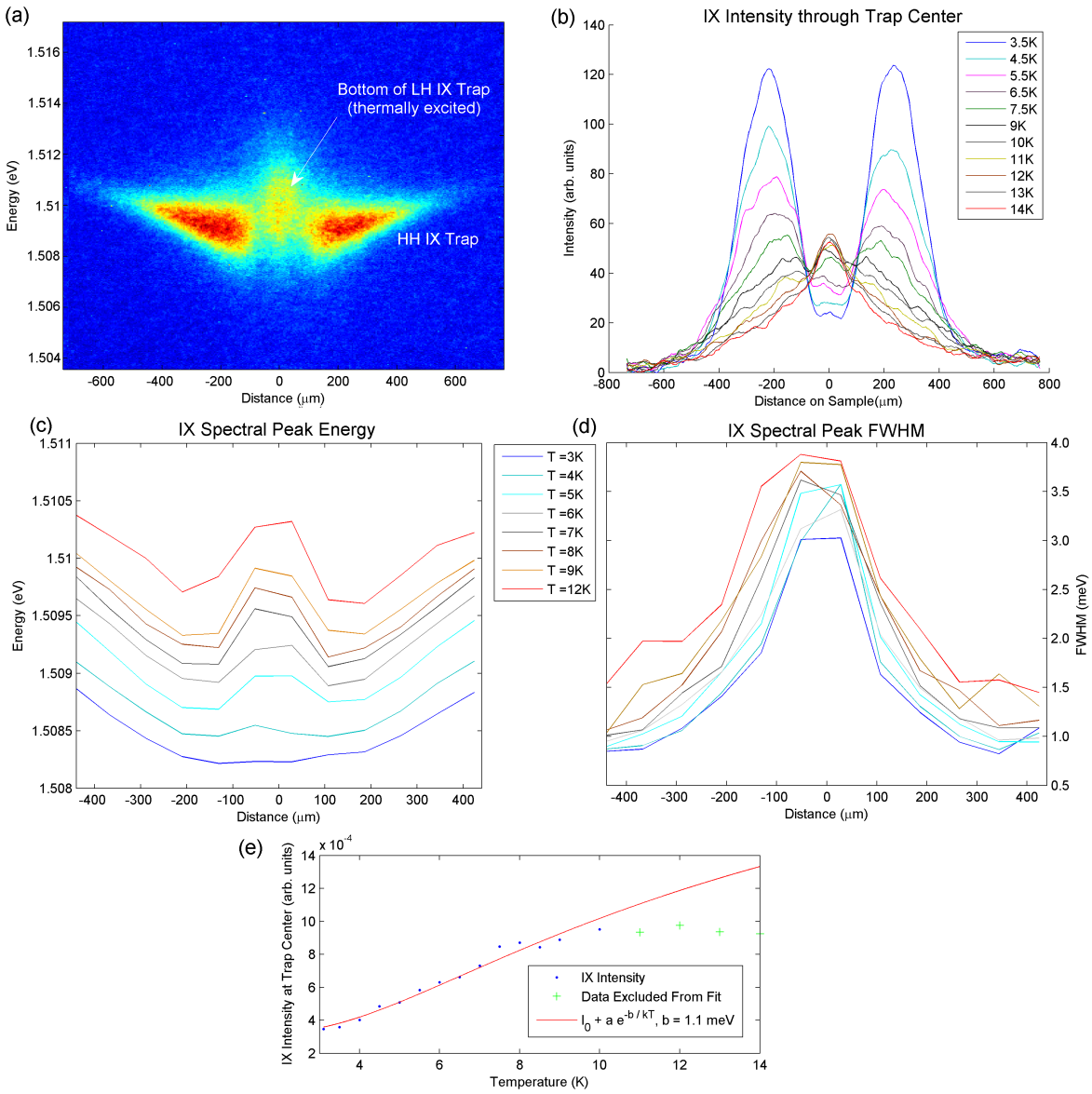

Figure 28: Thermal activation of LH IX with increasing temperature at a stress just prior to IX LH/HH crossing. (a) A spectral image of the IX PL at T=14 K. The camera is gated to collect luminescence beginning 2 μs after the end of the excitation pulse for 2 μs. (b) Cross-sections of total IX PL intensity through the trap center at varying sample temperature. At this stress, the LH IX state is thermally-activated, only appearing in the PL at increased temperature. (c) Cross-sections of the IX peak energy through the trap center at varying temperature. At T$\geq$5 K, the LH IX decay dominates the trap-center luminescence. (d) For cross-sections of the IX spectra through the trap center, the FWHM is plotted vs position for varying sample temperature. The spectral linewidth is always largest at the trap center, consistent with this position having the highest exciton density (largest scattering rate). (e) The total IX intensity at the trap center is plotted vs temperature and fitted to a Maxwell-Boltzmann occupation of the state. The state splitting parameter is fitted to be 1.1 $\pm$ 0.2 meV. The higher temperature data is excluded as it cannot match this model, which neglects that the number of excitons is approximately fixed.

this temperature. The spectral linewidths display that this newly-appearing luminescence has retained the large linewidth of the trap center luminescence. For all temperatures, the linewidth is greatest at the center of the trap by a large margin, suggesting that the scattering rate remains highest in this region. In addition, the linewidth increases at all locations with increasing temperature. Figure 28(e) attempts to fit the thermal activation of this LH IX PL to a Maxwell-Boltzmann occupation. The data points plot the measured intensity at the trap center vs temperature. The free parameters of the fit are the energy splitting, the radiative rate of the LH IX state, and the low-temperature intensity of the HH IX state. As shown here and in Figure 28(b), the trap center luminescence saturates in intensity at high temperature, as there is a fixed number of particles available. Since this is not included in the model and since this plot is included only to approximately verify that this behavior is consistent with thermal activation with an appropriate energy scale, the high temperature data showing this saturation is excluded from the fit. The fitted energy splitting is 1.1± 0.2 meV. As seen in Figure 28(c), this is consistent with the energy splitting between the upper and lower states at the trap center.

All of this behavior is consistent with LH IX approaching the HH IX state at high strain, as predicted by the larger shift of the LH energy with strain and as observed briefly in our microscope cryostat setup. At this strain, the LH IX seems to be positioned just above the HH IX state. At higher strain, we expect that the two states should cross, and the LH IX should become the lowest energy state at the trap center. Figure 29 demonstrates that this is indeed the case. In Figure 29(a), a spectral image of the IX PL at 3.5 K under increased stress shows that the LH IX has becomes the lowest energy state, no longer requiring thermal excitation. Figure 29(b) plots the spectra at the trap center for varying sample temperatures, where the luminescence only dims as the temperature is increased. Thus, this brightening seems to fit with the LH IX approaching and then penetrating through the HH IX state at the trap center with increasing strain.

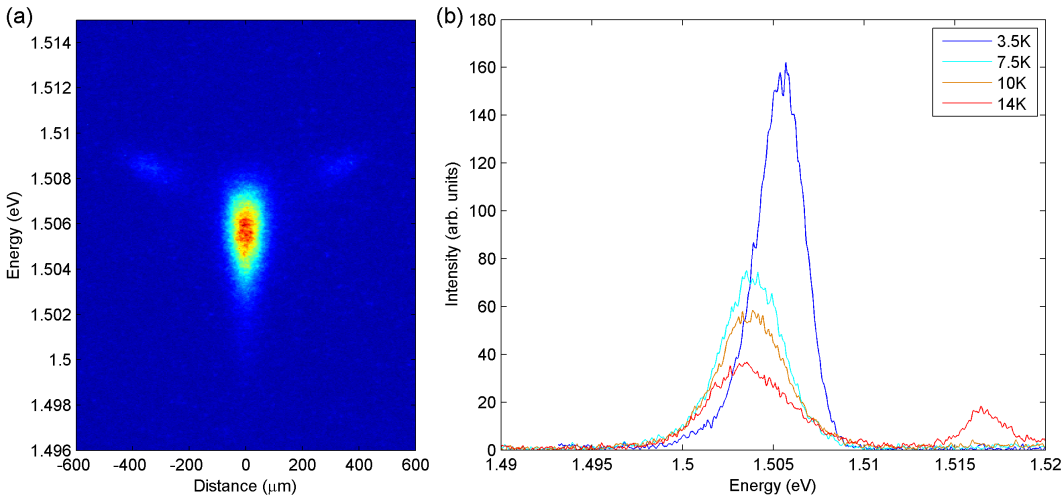

Figure 29: Appearance of LH IX luminescence at the trap center at low temperature with increased stress. The stress is increased beyond that in Figure 28. (a) Spectral image through the trap center at T=3.5 K. The LH IX luminescence has become the lowest energy state and no longer needs to be thermally excited. (b) Spectra of IX PL at the trap center at varying temperature. In contrast to the lower stress case, the luminescence only dims with increasing temperature. At 14 K, we see that the DX state is being thermally excited from population of IXs.

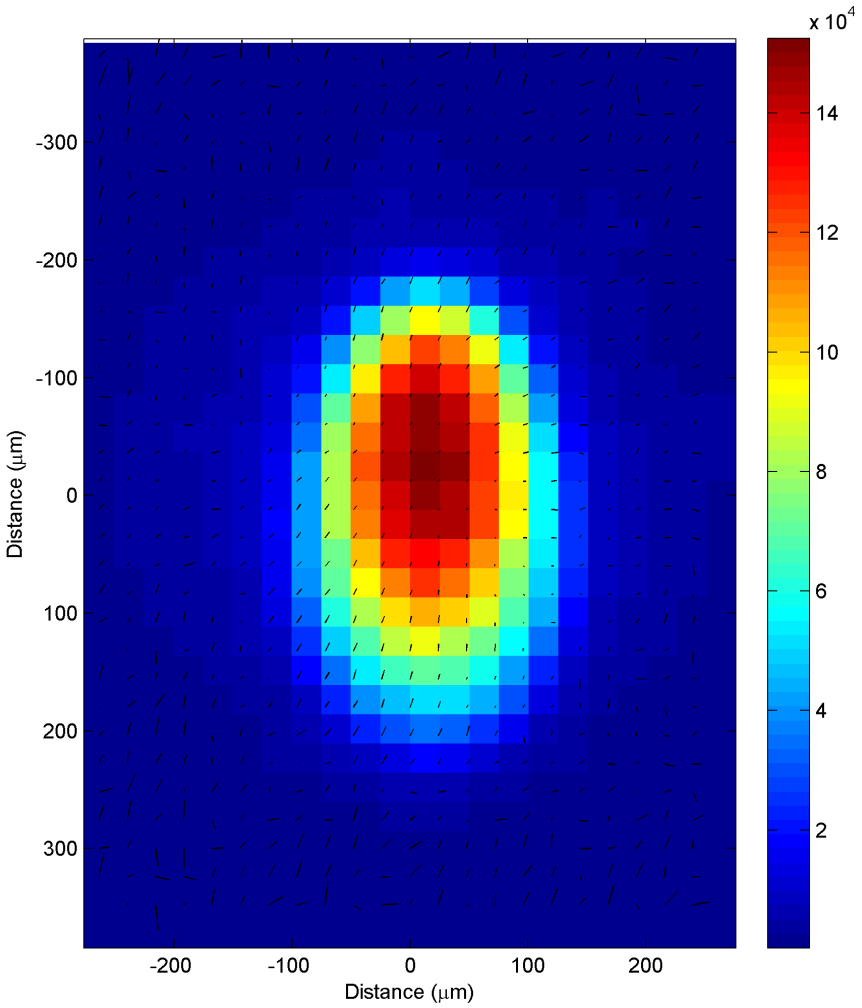

Figure 30: Linear polarization map at low stress. The background image shows the polarization-corrected intensity of the IX PL. The foreground vector plot indicates the fitted linear polarization orientation with the line orientation and the linear polarization degree with the line length. The linear polarization is very small at the trap center, increasing slightly away from the trap center. The fitted linear polarization in regions with no IX intensity should be ignored. The sample has 12 nm-wide wells and is held at T=2 K.

4.2.9 Linear Polarization of IX PL

Guided by previous studies showing a linear polarization of Bose-condensed exciton polaritons [37, 27, 9], the linear polarization of IX luminescence was measured as a function of position on the sample at varying stress, as described in Section 3.2.3. As the force applied to the sample is increased, we observe a pattern of increasing degree of linear polarization that varies spatially over the sample.

A polarization map of the IX luminescence in the low stress case (the regime of previous experimental works) is displayed in Figure 30. The intensity map plots the polarization-corrected intensity, a measurement of the total emitted light instead of simply the light collected through the linear polarizer, as described in Section 3.2.3, Eq (3.3). This is overlaid with lines representing the linear polarization angle with the line orientation and degree with the length of the line. The important feature from this plot is that at low stress, we observe only a small degree of linear polarization overall, especially at the trap center, where it is less than 5%. Also, the linear polarization increases in degree moving outward from the center. The fitted polarization in the regions of low intensity may be ignored. The excitation is confined to such a small area that we can't say much more about the overall spatial variation of the linear polarization. At higher stress, though, when the dark center is present, the intensity profile is much larger, and we can observe more of the pattern.

Figure 31 displays two fits of the same linear polarization data at higher stress. Figure 31(a) displays the result of directly fitting the full set of intensity data. Some of this stressed polarization data was reported previously [78] at the start of our investigation into this phenomenon, using all of the collected data set, as displayed in this image. However, the fits to these data considered several bad data points, and, therefore, the reported polarization maps were significantly skewed. In fact, as discussed in the next Chapter, the polarization maps provided by this fitting are quite inconsistent with our model for how this linear polarization is produced. Specifically, it showed a large asymmetry in polarization degree between positions away from the trap center along the [110] and [1$\bar{1}$0] directions. The white boxes in these images indicate particularly notable regions for this comparison. The linear polarization degree should be approximately equal in the two boxed regions in an

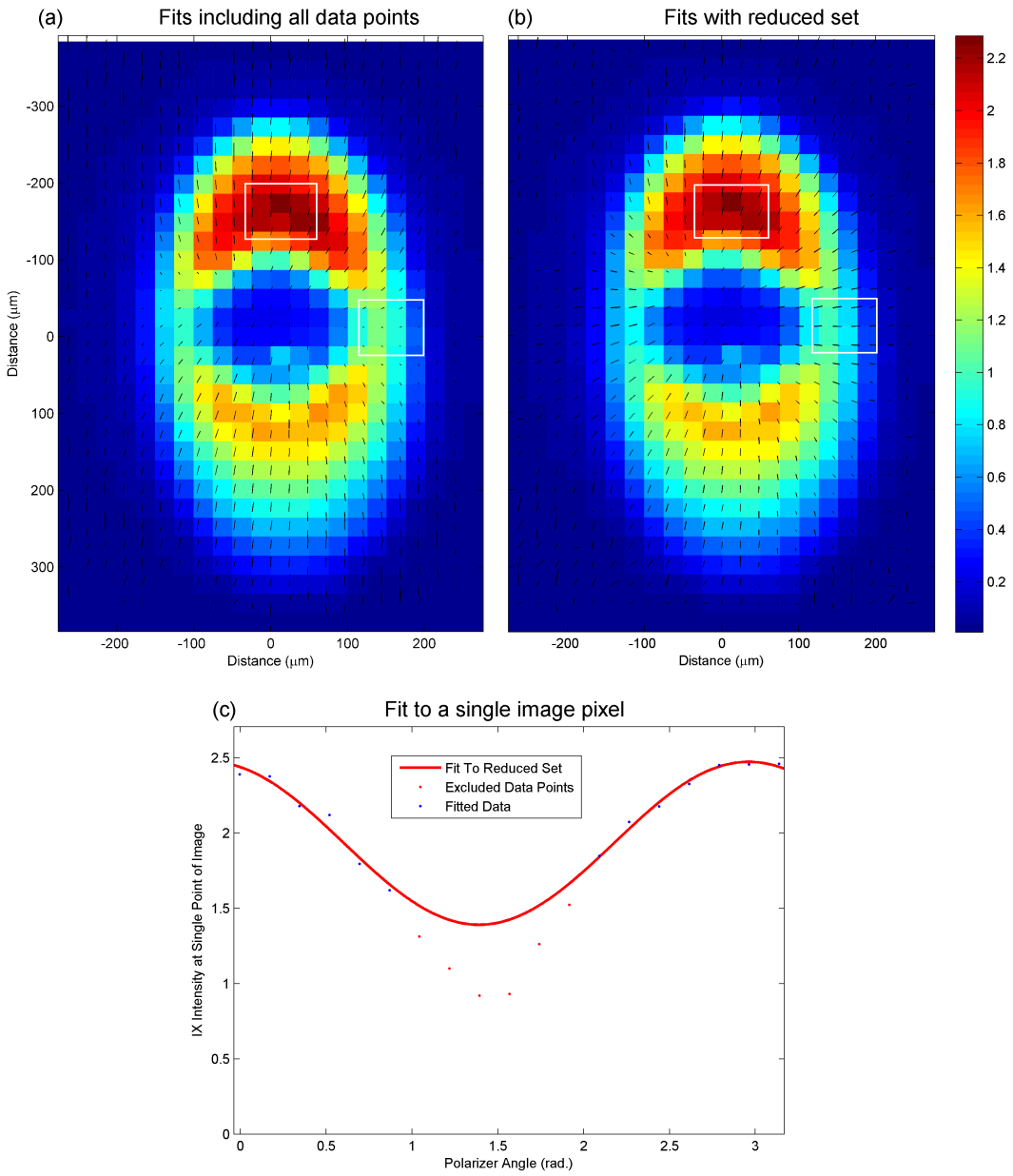

Figure 31: Uncorrected and corrected high-stress linear polarization maps. Two fits to the high stress linear polarization data were performed. (a) Previously published data including all of the data points in the set. (b) Revised fits excluding several neighboring polarization alignments that deviate strongly from the fit in a systematic way over the entire image. As explained in the text, the exclusion reduces the fit errors appreciably. In the previously published data, the degree of polarization is dramatically smaller at a position 150 μm away from the center in the horizontal directions than in the vertical direction. These regions are highlighted by the white boxes. This large asymmetry between the [110] and [1$\bar{1}$0] directions vanishes without these offending data points. (c) An example fit for a single pixel of the image. The excluded points are shown in red. The data sets for every other pixel of the image shows decreased intenity at these particular polarization orientations, even when directly contrasting with the overall trend of the remaining points.

image (as long as the strain from the trap is the only cause of LH/HH mixing, as explained in Section 5.1.2). Upon visually inspecting the individual per-pixel fits, the data seemed to follow a $\cos^2(\alpha)$ dependence very closely, apart from the intensity data from several adjacent polarizer orientations that were consistently low in every pixel of the image set. I believe there was some defect or smudge on the linear polarizer (it need only be about 1 mm in diameter to cause this behavior), which was being rotated through the image at these analyzer positions. Re-analyzing the data without these data points provides fits that much more closely reflect the data, and the result of these fits are displayed in Figure 31(b). However, since these data were re-analyzed specifically because they did not match our predictions, it is important that we provide a more quantitative justification for removing this data. If we collect the sum squared error (σ^2) and the mean counts per pixel from each pixel fitting, $\bar{n}_c$, we define a normalized error per data point in the following way:

$$E = \frac{1}{\bar{n}_c}\sqrt{\frac{\sigma^2}{n_i}}, \tag{4.1}$$

where n_i is the number of images in the set analyzed. This error represents the mean rms error per data point (a single pixel in a single image), so that it does not scale with the total number of data points, and it is normalized by the intensity at each point so that points with low intensity (i.e. the trap center when it is darkened) are given an appreciable weight. A minimum mean intensity is required to be included in the error calculation, so that the background regions around the trap are not included. With no excluded polarizer orientations, the average of E over the image is 0.222 (roughly a 22% error in predicting each data point), and by removing the strongly deviating data points the mean of E is reduced to 0.017. So, according to this metric, the fits are more than ten times more accurate without these data points, and we are quite justified in removing them. An example of the fit for a single pixel is shown in Figure 31(c). The excluded points are displayed in red. Each image pixel displayed a diminished intensity for these particular polarizer orientations, regardless of the trend of the remaining data points.

Actually, using either analysis, the first important conclusion can be drawn from the intensity data. Since the plotted intensity data is the total emitted intensity, corrected for the measured polarization, it is certain that the darkening effect is not simply an artifact

of linear polarization bias of the instruments. For example, it is not the case that the luminescence at the trap center is simply out of alignment with our instrument's polarization bias. In the corrected fits, there is approximately equal linear polarization degree along the weak and strong confinement directions. In comparison to the lower stress polarization map, the degree of linear polarization is much larger on the trap periphery. In addition, from the larger illuminated area, we can observe the overall trend of the polarization orientation, which is nearly radial, though tending to curve slightly toward the weak confinement axis.

This analysis was continued to even higher stress, though with a different sample[12] In Figure 32, a polarization and intensity map are displayed for the high stress regime where the trap center brightens again. The intensity profile here is abnormal in a couple of ways. First of all, the intensity is skewed all to the upper portion of the trap, simply due to the pump being located at a position well above the trap[13]. Second, the dark region surrounding the bright center is clover-shaped, rather than circular. This seemed to occur consistently in a single sample tested[14], and it is unclear the exact cause of this distinction. It seems that there is some difference in this sample that partially cancels the piezoelectric shift and causes more symmetric IX occupation (the bright region is more symmetric between the [110] and $[1\bar{1}0]$ directions, not showing the typical elliptical distribution favoring the [110] direction). If the dark region is due to ϵ_{xy} strain, as we propose in the next chapter, then this 4-fold rotation symmetric profile is natural, arising from the 4-fold rotation symmetry of the magnitude of ϵ_{xy} – it is typically not seen because the IX occupation is usually only

[12]This sample change was simply due to the fact that some time elapsed between the initial polarization analysis and when I felt confident that we could safely reach this higher stress regime. When I finally did push to higher stress, I was using samples with 14-nm wide wells, rather than the 12-nm wide wells, as they seemed to show the darkening effect at lower stress.

[13]This was to be certain to avoid contaminating the polarization with residual substrate luminescence from the pump. This was likely an overly cautious decision, as the temporal gating typically provides this filtering.

[14]"Single sample" here refers to a single cleaved piece of the wafer. Other cleaved pieces from this same wafer did not display this effect, so it is not due to the change in well width. This sample was actually cleaved from very near the edge of the wafer. While it is unclear the exact nature of the abnormality in this sample, it is very likely caused by its proximity to the wafer edge. We also observe higher energy DX energies in this sample in comparison to the wafer center, suggesting that the well-width is smaller on the wafer edge (a common growth defect) and hinting at the possibility of further abnormalities.

along the [110] direction due to the weak confinement in this direction[15]. It is unfortunate for direct comparison of the linear polarization to the lower stress results that the linear polarization measurements at this very high stress were exclusively done in this abnormal sample. However, there are certainly still conclusions we can draw from this data.

A very large number of positions were fitted in order to highlight the overall trends. Furthermore, there are a few points displaying very bad fits, and these are made clear by the presence of so many nearby points with an obvious trend. So we know which data to disregard. However, the presence of so many points is not advantageous for comparing actual magnitudes of the polarization, and, for this reason, this plot is reproduced in Section 5.1.2, with far fewer points and larger lines for a comparison with our theoretical prediction. An anisotropy in the degree of polarization is evident in this plot. In contrast to the lower stress case in Figure 31, where this was first observed and was found to be erroneous, in this case, there is no obvious correction to remove this effect. The anisotropy here seems to be real. Apart from the degree of polarization, the trend of semi-radial polarization direction seems to remain intact from the lower stress data in the more ordinary sample. Upon investigating this sample further, the low stress polarization is actually abnormal as well. Figure 33(a), the linear polarization map of this sample at low stress (before there is any darkening) is displayed. Figure 33(b) maps the degree of linear polarization at each point. In contrast to the low stress case in more ordinary samples, this sample displays a linear polarization at the trap center, even low stress. This polarization is about 15% at the trap center. The low intensity exterior region showing randomly oriented, 100% linear polarization is simply an artifact of the fit starting points, and this data can be safely ignored. I have included it to demonstrate that the background does not appear polarized (which tends to be the case when there are bad images in the set or improper background subtraction, as in the uncorrected fit of Figure 31).

[15]This is also the mixing profile that one would expect at near flat-band conditions. The total Stark shift (now due exclusively to piezoelectric fields) would be the same along the [110] and [1$\bar{1}$0] directions, and the equilibrium occupation would be isotropic. This is a rather strange situation, though, where the piezoelectric fields would cause differently-oriented IXs in the [110] and [1$\bar{1}$0] directions, and the IXs would have essentially the short DX lifetime along the [100] and [010] directions. So the intensity profiles would look dramatically different. For this and several other reasons, this is decidedly not the case in this experiment.

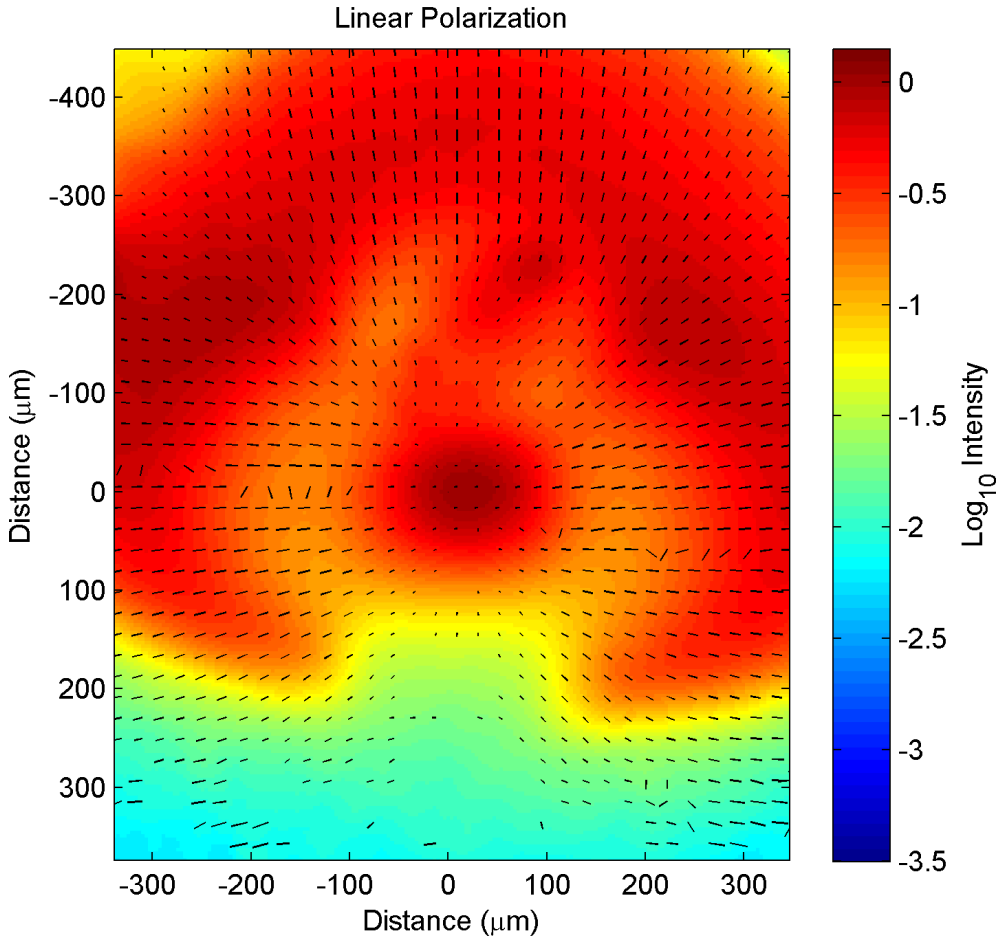

Figure 32: Linear polarization map at very high stress in a wafer-edge sample. At this stress, the trap center is bright again, as shown by the background image of the polarization-corrected intensity. This sample shows a four-lobed, clover-shaped darkening patten in contrast to the two-lobed patten seen in other samples. The uneven luminescence intensity between the upper and lower parts of the trap is simply due to the excitation laser being positioned well above the trap center. The (slightly) stronger confinement axis is aligned to the vertical direction in this image, rotated 90 degrees from the previous images. The trap-center luminescence is still mostly unpolarized, and, for the most part, the polarization degree increases in moving outward from the center. However, this is not true in moving along the vertical direction away from the trap center, where there is a decrease in polarization degree before a further increase.

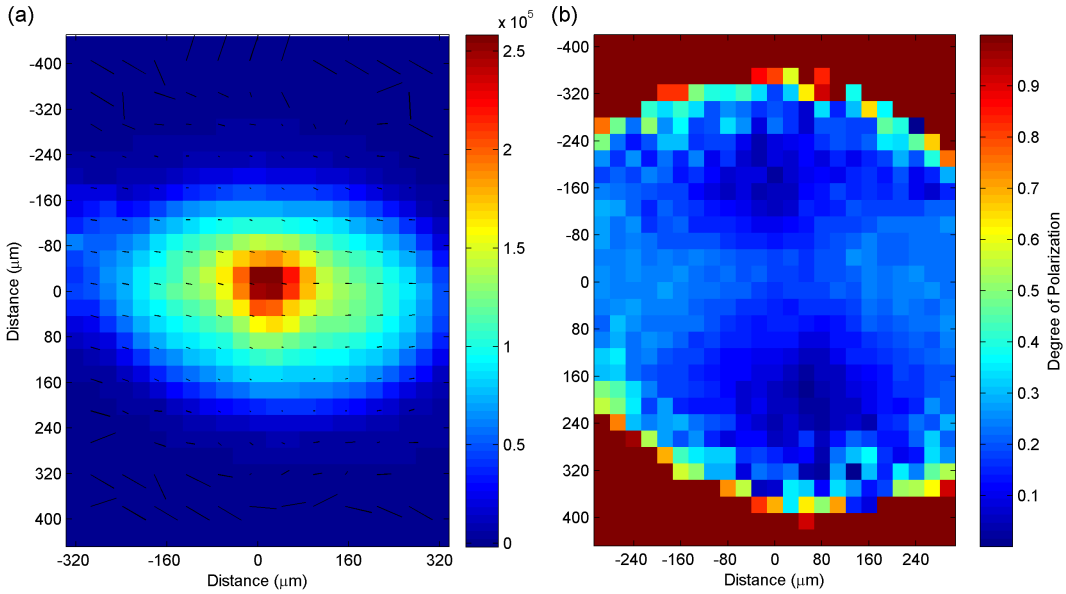

Figure 33: Low-stress linear polarization map from wafer-edge sample, showing additional mixing at the trap center. (a) A vector plot of the linear polarization is superimposed on the polarization-corrected intensity image. (b) A map of the degree of linear polarization. This sample shows a greater linear polarization at the trap center, and an asymmetry in the linear polarization degree between the [110] and [1$\bar{1}$0] directions.

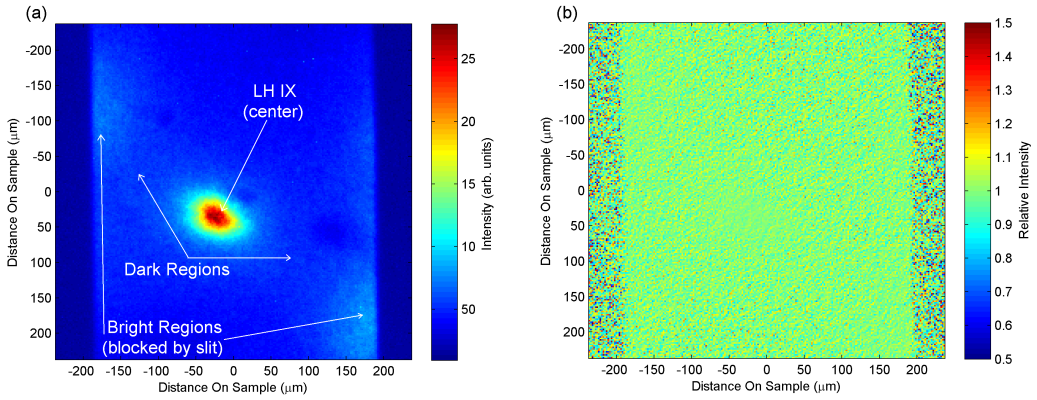

Figure 34: Interference measurement of deep-prap LH IX PL. (a) Intensity image from a single arm of the interferometer, with the other arm blocked. (b) The ratio of the interfered image intensity (from both interferometer arms), I_{M1+M2}, to the sum of the images from the two arms individually $I_{M1} + I_{M2}$. The deviation of this relative intensity from 1 represents the amplitude of the interference fringing. This image shows essentially no deviation from 1, demonstrating that we have no measurable coherence from the IX state with this spatial displacement of the two images.

4.2.10 Coherence Measurement of Deep-Trap LH IX Luminescence

As explained in Section 3.2.2, a Michelson interferometer was installed in the optical collection setup in order to determine the degree of spatial coherence of the PL in the darkened region. The purpose of this experiment is to test whether the small amount of light coming from the dim regions has long-range spatial coherence to indicate whether this light is coming from a BEC phase. This test is somewhat of a shot in the dark, as the expected BEC should occur in dark states. It is performed with the hope that there is some slight oscillator strength of this dark condensate due to a slight mixing with bright states. The interferometer arms were slightly misaligned in order to overlap neighboring positions on the sample. In this way, fringes in the observed luminescence pattern will signal long-range spatial coherence and that the spatial variation of the phase is consistent over the sample. For example, if the phase of the population is constant over the entire sample, the PL will show fringes with regular spacing determined by the difference in momentum orientation of the optical

beams incident on the detector. If, instead, there is some gradient in the phase, $\frac{\Delta\Phi}{\Delta x}$, perhaps due to an overall momentum of a coherent population, this will simply modify the fringe spacing uniformly over the sample. Vortices are typically also observable by this procedure, by noticing a phase rotation on top of the overall constant fringe spacing [37]. The phase need not be coherent over the excited sample region to see a constant fringe pattern over the entire region – it need only be coherent between points separated by the displacement of the two images and for the relative phase across this displacement to vary in a uniform way over the sample. So, if there is spatial coherence up to the image displacement, a large scale pattern should emerge in the image.

Figure 34 shows the results of this image interference in a sample under very high stress, with the two images displaced by 12 μm, as measured on the sample (not in the image). As explained in Section 3.2.2, this is close to the smallest image separation at which we should be able to discern a full fringe pattern on the image, and, as such, gives the lower end of the measurable coherence length with this detection scheme and experimental setup. The image displacement was measured by determining the fringe spacing of a HeNe reference beam passing through the same interferometer[16]. Figure 34(a) shows the image from a single interferometer arm, with the other arm blocked. The sample is stressed to the point of showing the LH luminescence at the trap center. The image magnification is very large, so that the darkened region around the trap center only barely fits between the interferometer slits, and the surrounding bright region is mostly cut out of the image.

The interfered image, adding the displaced image from the other arm, actually looks almost exactly the same as this, with each twin feature almost precisely overlapping, and showing no obvious fringing. For this reason, instead of showing this redundant image, Figure 34(b) shows the ratio of the interfered image from both interferometer arms (I_{M1+M2}) to the sum of the individual images from each of the interferometer arms ($I_{M1} + I_{M2}$), plotting $\frac{I_{M1+M2}}{I_{M1}+I_{M2}}$. This will isolate any interference effects – directly measuring destructive or constructive interference in any deviations in this ratio from 1. However, as shown, the ratio remains fixed at 1 in the data, with the only obvious variations across the image being

[16]This is the same beam used for stabilization of the interferometer arm length. Temporarily removing the long-pass filter, which typically prevents this beam from detection, allowed this measurement.

an increase in the signal/noise ratio at the trap center, where it only more accurately shows that this ratio is 1. From this, we can draw the conclusion that the spatial coherence length is lower than 12 μm. Perhaps, this is not surprising, as there is quite a large separation between the classical coherence length of 100 nm to 12 μm. However, these figures aren't wholly out of the question. A recent experiment claiming to demonstrate a BEC of IXs [23], measures coherence lengths of about 5 μm at particular regions of their sample, extending up to 10 μm at one point.

In any case, from this experiment we have gained an upper limit on the coherence length of the IX PL at high stress of 12 mum, and, therefore, we have excluded the possibility of a semi-bright BEC with a large degree of spatial coherence.

4.3 USING AN IN-PLANE MAGNETIC FIELD TO "BRIGHTEN" DARK EXCITONS

Up to this point, it is unclear if there is any unique role for dark excitons in the intensity patterning. For example, one might consider a separation of the two species if the dark-bright and dark-dark interaction strengths were, for some reason, drastically different. As discussed later in Section 5.3, this would be the mechanism for a BEC-driven phase separation, where the difference in the exchange interaction between the condensed dark states and uncondensed bright states provides differing interaction strengths. The difficulty with evaluating the role of the dark states is that we have no probe of their population or energy spectra by photoluminescence studies since the radiative transition is forbidden by angular momentum conservation. As explained in Section 2.2, there is reason to believe that an in-plane field will cause the dark states to be mixed slightly with bright states, so that the oscillator is traded partially from the bright states to the dark states. If this mixing occurs and the phase separation picture is correct, the mixing should lead to a significant brightening of the trap center where a large population of dark excitons supposedly reside.

First, the behavior of the IX system under the applied magnetic field is observed without applied stress. Initially, the spectra of exciton states under varying magnetic field strength in

this experimental setup showed extremely erratic behaviour. Figure 35(a) shows the spectra of DX, BiDX, and IX states under varying magnetic field with 0 V applied bias. The IX state is shown to red shift extremely strongly (by almost 4 meV) in changing the field from 0 T to 0.71 T. Subsequently doubling this magnetic field to 1.42 T then yields a strong blue shift, nearly back to the original position. This particular behavior is actually not unprecendented. Negoita et al. [51] showed that IXs in a growth-direction magnetic field show a strong red shift before the more traditional diamagnetic blue-shift. In that case, this was due to a magnetoresistive change in the layered structure. Here, however, the shift displayed here is not consistent. It is neither smooth with magnetic field nor reproducible between experiments, suggesting the magnetic field may be altering the experimental setup in a chaotic manner. The large amplitude of this error suggests an inconsistent electric field, since the IX states are so strongly shifted by the electric field. This is most likely due to a small structural instability of the sample holder leading to a variation in the quality of the sample-plate contact[17]. The sample-plate contact has previously been problematic, particularly with the application of force to the sample from above. To remedy this problem in the case of applied force, indium foil was placed on the (upper) substrate side of the sample, which significantly reduced the force-dependence Stark shift. However, the experiments presented here have already included indium foil on the substrate side. So, to continue these experiments, indium foil was carefully placed on both sides of the sample[18]. This dramatically decreased the amplitude of the random IX energy shifts, but did not remove them completely. Thus, it is necessary to attempt to compensate the electric field in the wells.

The most accurate measurement of the electric field in the wells is actually the IX peak

[17]There is no conflict between the facts that we have applied no bias to the sample and we are observing a shift that seems to depend on the quality of the contact to the sample. The optical excitation injects carriers into the structure, which will flatten the built-in field if they are not drained off by the sample contacts. In this case, the contacts are simply shorted together, so that in the case of good conduction the IXs should always feel the built-in field. For poor conduction, the electric field will be lower and the IXs will be blue-shifted due to the smaller Stark shift.

[18]As explained in Section 3.1.3, this is much more likely to cause the thin sample to break, as it requires the sample to be pushed into a piece of indium foil with a hole cut in the center. Mechanically cutting out the center of the foil tends to leave a nonuniform thickness to the film, making it likely that the sample will break when pressed into it. If this step is necessary in the future, a more sophisticated method of removing this material is recommended, such as laser cutting the hole.

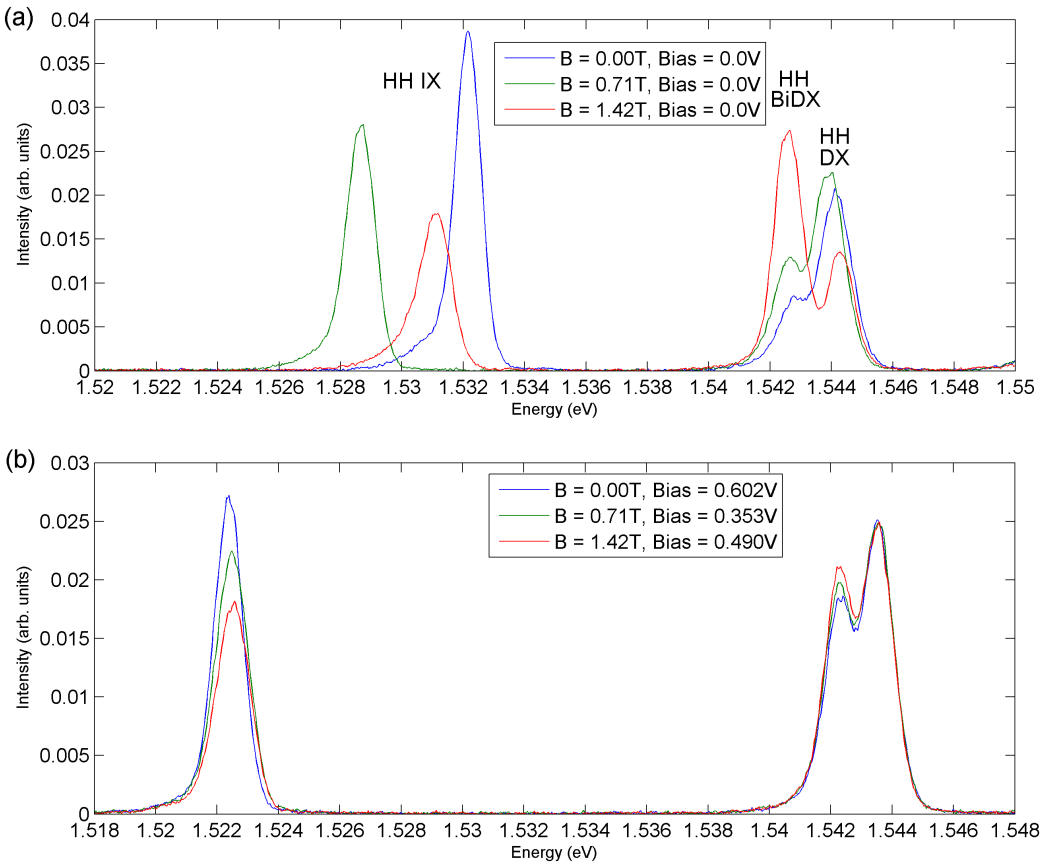

Figure 35: Spectra of exciton states under varying in-plane magnetic field strengths with no applied force. T=2.0K. (a) Turning on the field leads to an erratic shift of the spectral line. The chaotic behavior of the IX line is attributed to a chaotic dependence of the sample-plate contacts on the magnetic field. (b) The variation of the electric field with magnetic field is approximately compensated by fixing the IX spectral position. At constant electric field, the IX intensity is seen to drop and the BiDX component grows.

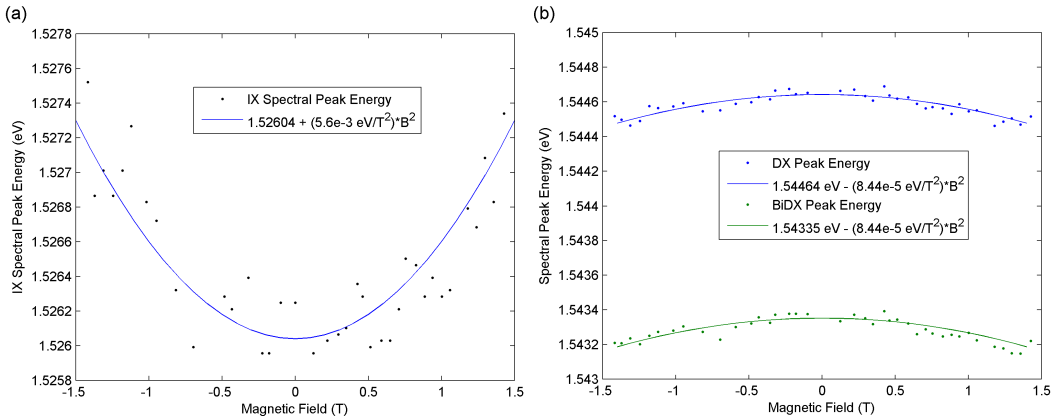

Figure 36: Spectral peak energies vs applied in-plane magnetic field. The in-plane magnetic field was applied without applying stress to the sample, with a thin layer of indium foil on both sides of the sample. The applied bias was 0.0 V. T=2.0 K.(a) The IX spectral peak energy shows a symmetric, quadratic blue shift with applied field. A quadratic fit to this shift gives a quadratic coefficient of +0.00056 eV/T^2. (b) The DX and BiDX spectral peaks both show a very slight quadratic red shift, with coefficient -8.4E-5 eV/T^2.

energy, as it is so sensitive to this field. Therefore, to compensate the chaotic shift of the electric field, the IX energy will be set to be approximately constant when the magnetic field is changed by adjusting the applied bias across the sample. An example of this adjustment is shown in Figure 35(b). A variable applied bias is applied to adjust the IX positions to be approximately constant. Two effects of the magnetic field are immediately apparent. The IX intensity is falling with increasing field, and the BiDX component is increasing. These spectra are collected from only a small portion of the sample, directly under the excitation. The images show that actually the IX states are becoming more spread out in the case of increased magnetic field, causing this localized sample to appear dimmed. This spreading is most indicative of a lifetime increase of the IX states with this in-plane magnetic field. The growth of the BiDX component is typically indicative of increased DX density. Since this state is an intermediate state in the energy cascade from excitation to IX states, it could also be indicative of slightly suppressed tunneling into IX states or a decrease in the lifetime of the BiDX state.

Equating the IX spectral peak energies certainly ignores the diamagnetic shift of the IXs, which is expected to be small. However, we can attempt to make a measurement of the diamagnetic shift despite the chaotic shifts. In a sample with indium on both sides, the shift of the exciton states with magnetic field was measured. Figure 36 shows the spectral peak energies with varying magnitude of the in-plane field, with 0 V applied bias in 12 nm wide wells. Figure 36(a) shows the IX energy shift. Though there is still significant scatter of the peak energy, there are sufficient data points to see that there is a roughly quadratic, symmetric shift of the IX peak energy[19]. Fitting this data to a quadratic shift, gives an IX energy dependence of $E_{IX} = 1.526\text{eV}+(0.00056\text{eV/T}^2)B^2$, predicting a total shift of 1.1 meV for the highest field of 1.4 T. This quadratic coefficient is much larger than the 0.00013 eV/T^2 predicted by the dispersion shift[20]. So, while the prediction of an increased lifetime from the in-plane field seems to be valid from the observed increased spreading of the exciton population, the measured shift is far larger than that analysis predicts. Figure 36(b) shows the DX and BiDX energy shifts, which both show a very slight quadratic red shift with increasing field strength. This DX red shift is unexpected. We will not address the potential causes of this shift because it is on the same order as the error, and it is far from the intention of this work. It is included here for completeness and context for the IX shift.

There is another scheme that one might use to approximately compensate the electric field in the wells. That is, since the change with varying field seems to be due to contact quality, the measured current through the sample could be adjusted to be constant. This approach is not without merit. Performing this current adjustment in a sample with indium foil on only one side (consequently having much larger variations in the field), the quadratic shift of the IX state was again measured. With a constant current (to the degree to which we are set up to measure this current, $\pm 5\%$), the IX peak energy was measured to have a quadratic coefficient of (0.0006 eV/T^2), essentially the same result. The scatter in this data is similar to that of the data with foil on both sides. So, using this method, one is

[19] In addition, we can see that the double-foil has decreased the scatter of IX peak energies from several meV to about 0.3 meV.

[20] This shift is described at the beginning of Section 2.2. Here the in-plane hole mass of 0.12m_0 and electron mass of 0.067m_0 have been used. In addition, 16nm is used as the value for the electron hole separation, which assumes that the electric field has not polarized the wavefunctions at all. Polarizing the wavefunctions due to the applied field will slightly increase this shift, but not enough to reach the observed shift.

able to compensate for the lack of indium on the optical side. However, the rather poor resolution of our electrical current measurements still leaves the method of equating the IX energies to be more precise. This is additionally corroborated by the measurements of Negoita et al., where, in the case of a magnetoresistance change in the sample, a significant magnetoresistive shift of the IX state was observed with no measured change in the current through the sample [51].

With this established, the case of interest was then investigated by creating a strain trap in the sample in addition to the in-plane field. Primarily, the behavior under test is whether the darkened center will brighten under the influence of this symmetry-breaking field. Figure 37(a) shows the result of applying force to the sample to cause the darkening and, subsequently, turning on the in-plane magnetic field. At each magnetic field, the applied bias is adjusted to fix the position of the IX spectral peak at that of the B=0 T case. Since the magnetic field changes the linear polarization of the luminescence at each point by mixing angular momentum states (see Section 2.2), it is necessary to collect a series of images with a rotating linear polarizer before the spectrometer in order to measure a single 'polarization-corrected' intensity map. This map plots the total emitted light from each point, rather that just the polarized or unpolarized components, as detailed in Section 3.2.3. A cross-section through this intensity map is plotted in Figure 37(a). The darkened region grows with increasing magnetic field, and, as expected in the 'brightening' model, there is a bump in the intensity at the trap center at the highest magnetic field. Unfortunately, these two features are also signatures of increasing force applied to the sample. Indeed, inspection of the DX energy at the trap center shows that the DX energy is significantly lower at high field, consistent with an increasing force on the sample with increasing field. Again, the slight instability of the sample holder seems to cause an unexpected dependence on the applied field. It appears, since the image of the sample is observed to move slightly with applied magnetic field, that the coils are moving the entire sample holder slightly and causing an increased force.

The change in force with magnetic field can also be approximately compensated. The best measure of the applied force is the DX peak energy at the trap center. By adjusting the applied force to hold a constant DX peak energy, the strain should be very close to

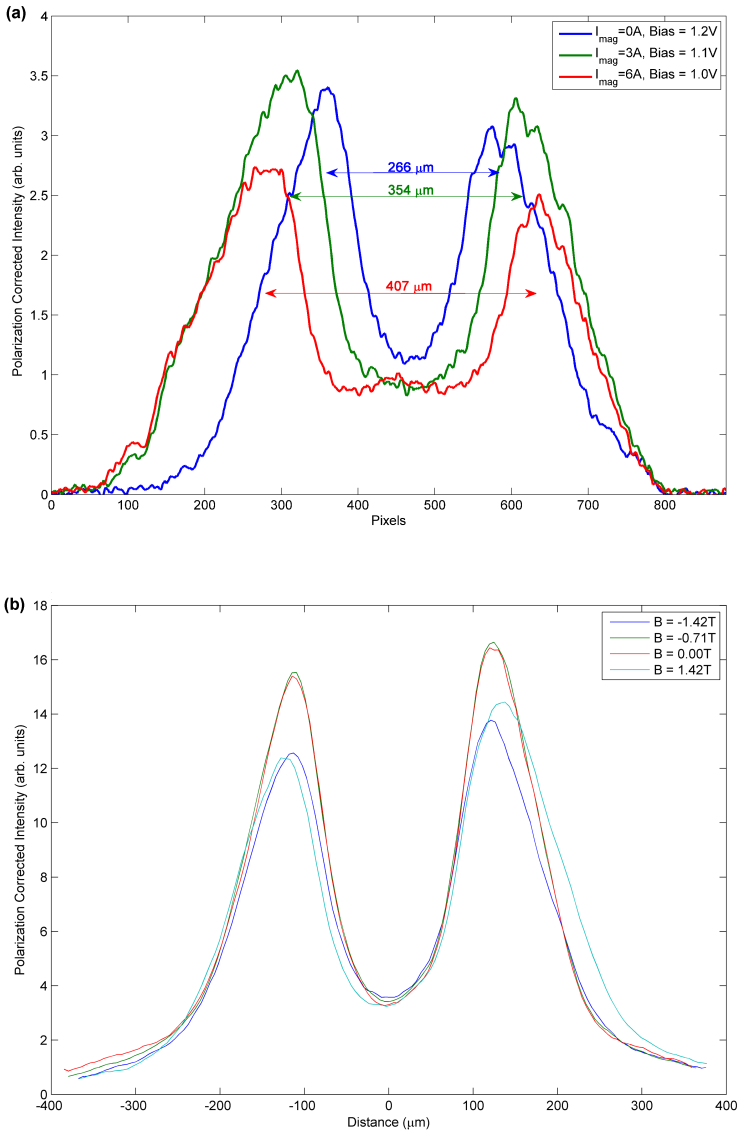

Figure 37: Effect of in-plane magnetic field on the darkened-center intensity pattern with (a) compensated applied bias and (b) compensated bias and compensated stress, in 12 nm wells at T=2.0 K. In both cases, stress and optical excitation are applied to the sample to produce the darkened center pattern. The in-plane field is then turned on. In (a), the bias is adjusted to fix the IX spectral peak energy at that of the B=0 T case, to compensate for electric field modifications due to the magnetic field. The size of the darkened region is observed to increase in size with increasing field. While the horizontal axis is labeled in camera pixels, the correct peak separations in μm on the sample are labeled on the plot. Also, at the highest field, the center has a slight bump in intensity. While seemingly consistent with the hypothesis of dark excitons brightening, both of these changes are actually due to the magnetic field increasing the stress on the sample. In (b), in addition to compensating the bias, the applied force was also adjusted to fix the DX spectral peak position at the trap center, correcting for the variation of applied force with magnetic field. The collected data at +0.71 T was discarded due to inaccurate alignment of the peak energies.

constant with varying field. Figure 37(b) shows the result of repeating the analysis from Figure 37(a), but additionally fixing the applied force. The plot shows cross-sections for B = -1.42 T, -0.71 T, 0.0 T, +1.42 T. The data for B = +0.71 T was discarded, as the DX energy was observed to differ by 0.2 meV, causing a signicantly different profile. The remaining data show only a trend that the highest magnetic field cases seem to be slightly dimmer on the periphery, with absolutely no change between the 0.0 T and 0.71 T cases. The center luminescence remains nearly constant with magnetic field. This does amount to the center becoming relatively brighter compared with the sides. However, this is not the smoking gun that was anticipated from this experiment, proving clearly that there is a large population of dark excitons at the trap center not typically represented in the PL. Since the paucity of magnetic field data points in these plots is partially to blame for the ambiguity, one might naturally suggest that these profiles should be sampled for many more magnetic fields. The reason so few are sampled is the time required to collect each one, apart from having to discard some due to mismatching the bias and stress. Since each intensity map requires an entire series of images to be taken to correct for the polarization changes, each magnetic field profile requires about an hour to collect, without accounting for the time needed to adjust the stress and bias for each magnetic field. So, only a few magnetic fields were used for the comparison.

In summary, it appears as if there is no measurable effect from the in-plane field that will prove or rule out the presence of dark excitons at the trap center. There is no extremely bright peak appearing with the onset of the magnetic field that would immediately signal a dark BEC. Lacking that or other extremely conspicuous signs, this pursuit is left with only a few small effects and, perhaps, very indirect evidence. With the ambiguities caused by battling instabilities of the apparatus, the credibility of these small effects are certainly called into question. So, overall, this effort has only ruled out the very exceptional case, i.e. that there was a huge density at the trap center simply waiting for a symmetry-breaking nudge to appear.

5.0 ANALYSIS AND DISCUSSION

With increased strain, several things occur in roughly the same strain regime: the asymmetry of the trap, a darkening of the PL (or relative darkening), and a spatially-varying linear polarization of the luminescence. It is reasonable to suppose that the simultaneous appearance of these effects is not a coincidence. The discussion of the experimental results will begin by proposing a mechanism by which we can qualitatively explain all of these effects with the valence-band mixing effect of off-diagonal strain, ϵ_{xy}, and its increasing importance as the LH/HH splitting shrinks with applied force. The individual experimental results will be analyzed and discussed in the context of this model, highlighting correspondences and discrepancies. These results could also be discussed first in the light of excitonic BEC, as the onset parameters are compatible with those expected of BEC. However, the strain-induced state-mixing model provides more concrete predictions and a better starting point for discussion of the various phenomena associated with the IX darkening.

So, first, the valence-band mixing model will be discussed in depth, showing that while there are many compelling congruencies between the predictions of this model and the darkening phenomenon, this model falls short of accounting for this behavior. Following this, the intensity patterning will be discussed separately in regard to the presence of an electron-hole liquid. The theoretical basis for an interwell EHL state is reviewed, and the ability of the applied stress to promote state degeneracy is examined. It is found that the LH/HH state mixing produced by the strain suppresses degeneracy to the extent that the intensity patterns are unlikely to be caused by an EHL. In light of the short-comings of the previous mechanisms, the phenomenon is examined in the context of a BEC, despite having few direct experimental metrics to determine a BEC's presence.

5.1 VALENCE-BAND MIXING MECHANISM

The Pikus-Bir Hamiltonian, Eq. 2.2, shows that the LH and HH valence-band will be mixed by off-diagonal and shear strains. The R term,

$$R_\epsilon = \frac{\sqrt{3}b}{2}(\epsilon_{xx} - \epsilon_{yy}) - id\epsilon_{xy}, \tag{5.1}$$

in Eq. 2.2, mixes LH and HH states with opposite total angular momentum. When combined with electron states, this corresponds to mixing states of equal magnitudes of the total exciton angular momentum ($|+1\rangle$ mixes with $|-1\rangle$, $|+2\rangle$ with $|-2\rangle$). So the bright/dark states remain distinct with this strain[1], but, as demonstrated in Section 2.3.1, there will be a linear polarization of the luminescence due to the mixing. Now, coupling this spatially-varying, valence-band mixing with the prediction that the LH and HH will have very different oscillator strengths for recombination, there arises a natural explanation for patterning of the intensity profile. Since the LH IX should have a much faster recombination (roughly a factor of 10), the areas with some LH component in the lowest energy state should be brighter.

Following this logic, since the lowest energy state is typically the HH IX due to the difference in confinement energy, the bright areas should be regions where there exist ϵ_{xy} or $(\epsilon_{xx} - \epsilon_{yy})$ strains to mix the higher energy LH IX state into the ground state. These strains arise from the applied force, but only away from the center of the trap, as shown in Fig 6(d).

So, to summarize the mechanism, at high stress the LH IX state and HH IX state approach each other in energy. When the HH IX remains the lowest state, the brighter LH IX state becomes partially mixed into the ground state only away from trap center. So, the radiative rate on the periphery of the trap is elevated, causing the center to be relatively darker. Much of the experimentally observed behavior can be qualitatively explained by this mechanism, though there are difficulties in reconciling even a few of the qualitative predictions with experiments. Conforming the simulations to the quantitative experimental

[1]The S term that would mix these states due to strain relies on z-component strains, such as ϵ_{xz}. These are several orders of magnitude smaller than the other strains in our system due to the proximity of the quantum wells to the free-floating bottom surface.

data provides a very bleak outlook for this success of this mechanism in explaining the intensity patterning.

In the following sections, the compatibility of this model's predictions with the experimental data will be examined. The discussion begins by scrutinizing the qualitative predictions of the model in light of the general behavior of the experimental data. These are the results that are largely published in our previous article on this subject [69], which cited this mechanism as the most likely explanation for the intensity patterning. In Section 5.1.1, the density and stress dependence are explained well by simulations of the mixing due to the applied strain, yet with some important simulation parameters largely undetermined by experimental data. The results of these simulations are presented here in order to show that the effect is possible, in principle, and in order to contextualize the previously published account. Section 5.1.2 shows that the predicted linear polarization pattern is consistent with the experimentally observed pattern, but the intensity pattern is contradictory to that expected from the polarization. Next, Section 5.1.3 explores the temperature dependence of this effect, highlighting that no means seem to exist in the mixing picture to explain the disappearance of the intensity patterning with elevated temperature in the lowest stress cases. Section 5.1.4 examines the variation of the lifetime with strain, showing that the mixing model cannot account for the lengthening of the lifetime with increasing strain. Finally, in Section 5.1.5, the spatial profiles of the emission energies are fitted in an attempt to constrain the parameters of the simulations and determine whether the parameters required to produce the pattern are able to be reconciled with other experimental measurements. The parameters gleaned from the fitted energy profiles are largely inconsistent with the mixing picture – the predicted mixing fractions are not large enough to produce the observed patterns. The results and parameters of the previously published simulations are then put into context to demonstrate where the inaccuracies lie. Section 5.1.6 goes on to add that, though the experimentally constrained simulations have shown the mixing theory to be flawed, they provide a good prediction for the darkening of the DX state, as observed in Section 4.2.3.

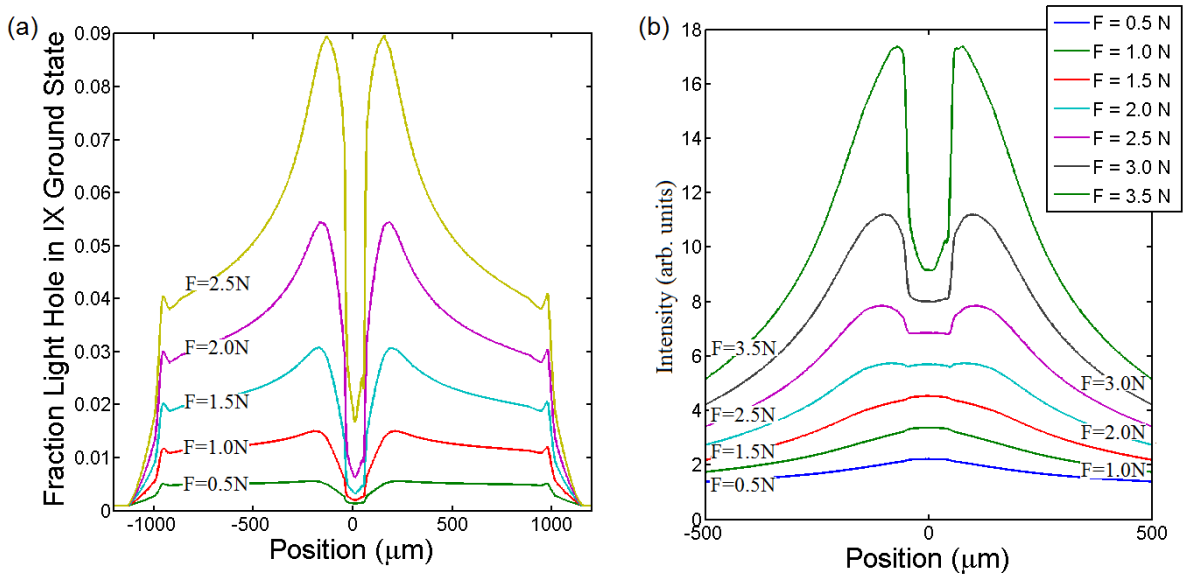

Figure 38: Predicted LH fraction in the IX ground state and resulting intensity profile with varying stress, using LH/HH mixing theory (with experimentally unconstrained parameters). (a) For each force, the predicted LH fraction in the IX ground state is plotted vs position, demonstrating a marked increase in this fraction exclusively on the trap perimeter. (b) Using a Maxwell-Boltzmann occupation of the trap for each force (at fixed total number of IXs), the LH fraction from (a) is used to predict the resulting intensity profile.

5.1.1 Simulations Showing Patterning With Increasing Force and Density

Figures 38(a-b) show the results of a simulation of this mixing for increasing applied force, demonstrating that this pattern of a darkened center emerges naturally from this analysis. Figures 38(a) predicts the LH fraction in the lowest energy IX state, f_{LH}, as a function of applied force to a 125 μm-thick wafer. The eigenstates are determined in the same way as described in Section 2.1, diagonalizing the Hamiltonian at each location independently, and, thus, the LH fraction of the lowest energy state is determined by the magnitude of the LH/HH mixing term (from the simulated strain) and the energy separation between the states. Close to trap center, where the LH/HH splitting is small, the mixing increases when moving away from the center because the off-diagonal strain increases. However, that off-diagonal strain plateaus away from the center. So, continuing to move away from the center continues to increase the LH/HH splitting, while no longer significantly increasing the magnitude of the mixing term, and the mixed fraction begins to fall. So, the expected non-monotonic behavior is already evident in the mixing fraction.

However, Figure 38(b) goes further to show the effect of this mixing on the predicted intensity profile. The radiative rate of the lowest energy state at any point, $K(\vec{r})$, is given by the radiative rates of the LH and HH states, τ_{LH}^{-1} and τ_{HH}^{-1}, and the mixing fraction, f_{LH}, by:

$$K(\vec{r}) = f_{LH}\tau_{LH}^{-1} + (1 - f_{LH})\tau_{HH}^{-1}. \tag{5.2}$$

Here we continue to assume that $\tau_{LH}^{-1} = 10\tau_{HH}^{-1}$. The IX density profile is estimated by assuming a non-degenerate, equilibrium population in the trapping potential, $V(\vec{r})$, for each applied force. So, the density at each point, $n(\vec{r})$, is given by the Maxwell-Boltzmann distribution,

$$n(\vec{r}) = n_0 e^{-\frac{V(\vec{r})+\gamma n(\vec{r})}{k_B T}}. \tag{5.3}$$

The constant n_0 is varied for each applied force so that the total number of particles remains the same for each applied force. Multiplying these densities and radiative rates yields the relative intensity from each point, as shown in the figure. Moving away from the center, the density is falling relatively slowly compared to the rise of the mixing fraction, so the sudden increase in the radiative rate in the first 100 μm away from center causes a sharp increase

in the intensity. With large applied force, it is possible to achieve a high contrast between the trap center and the brightened sides.

These simulations were previously published in [69], in order to demonstrate the possibility of this behavior. However, this simulation only attempts to qualitatively explain the data, not attempting to quantitatively reconcile the simulation parameters with any experimental data. In particular, there is nothing linking the magnitudes of the simulated forces to those in the actual experiments, apart from the upper bound on the experimental applied force given by the measured spring compression. The simulation includes a very small offset to the LH/HH mixing term, which causes a small amount of mixing[2] at trap center, in order to account for a degree of mixing at trap center evident in the linear polarization data.

This simulation also shows how the pattern can arise through this mechanism by only increasing the density once the mixing profile has been established by a sufficient applied force. Figure 39 plots the result of performing the same procedure used to generate the intensity profiles in Figure 38(b), but for a fixed, large applied force and a varying density of particles in the trap. The intensity profiles are normalized by their maximum value simply for convenience. The highest power plot has a nearly constant density profile in the central region, showing from the intensity contrast that the radiative rate at the center is roughly half that at the brightest point. Lowering the excitation power shrinks the size of the exciton cloud, until the population is confined to a region that only very slightly overlaps with the region of mixed character. These intensity profiles are similar to those seen in the experiment, particularly Figure 22, where it is clear that when this pattern appears with increasing density there is no actual darkening in the center. Instead, the sides seem to brighten as the density profile grows. Similarly, note that in the experimental plots the size of the intensity profile when it is singly peaked at trap center is such that nearly no light is coming from the regions that become brightest at later times (when the density is larger). So, the experimental data is consistent with this picture of a population that is expanding into regions of significant mixing.

In Section 4.2.2, it was briefly mentioned that the IX darkening occurs at higher applied force for thinner quantum wells. This is in complete accord with any explanation for the

[2]The magnitude of this offset corresponds to the mixing caused by an ϵ_{xy} of 0.005%.

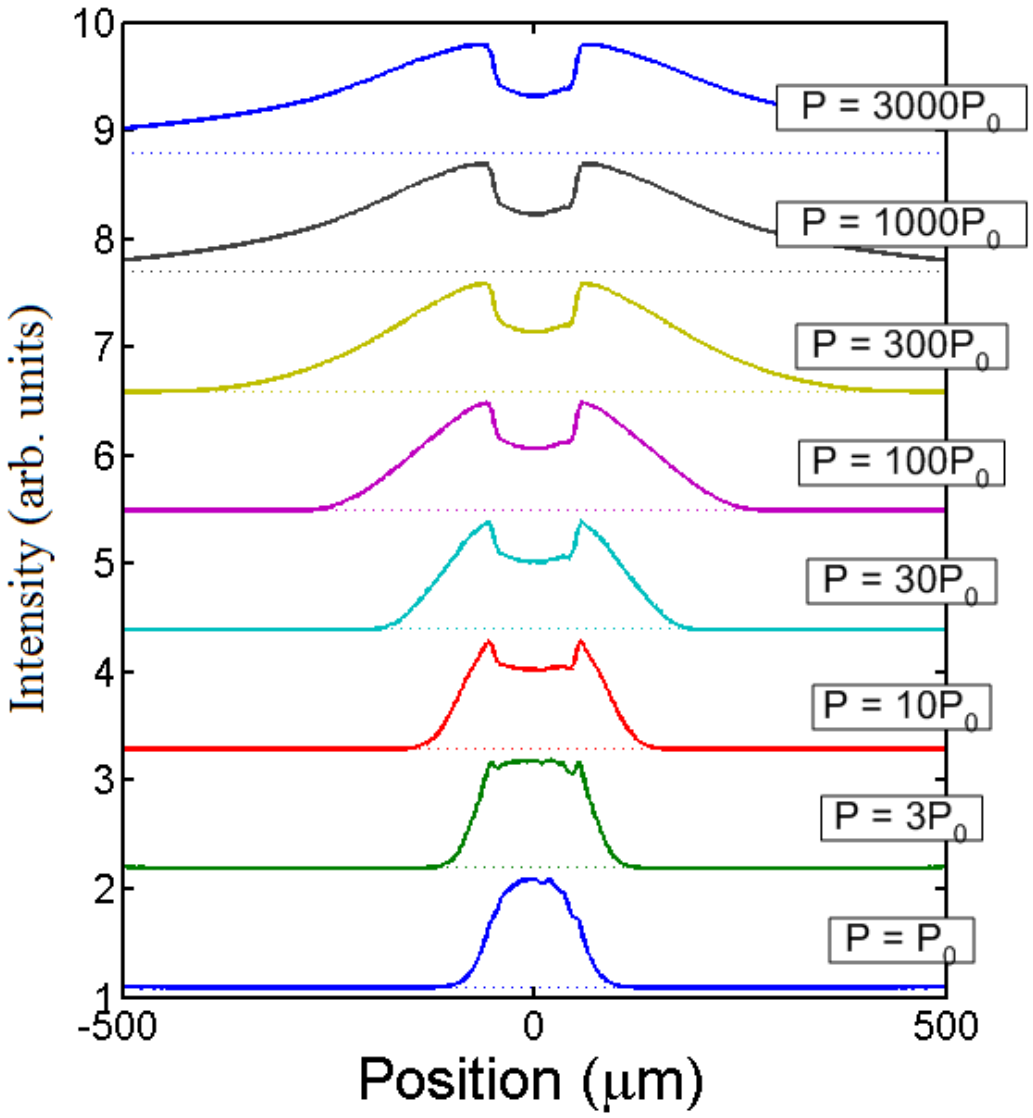

Figure 39: Simulated density dependence of LH/HH mixing model of intensity patterning (with experimentally unconstrained parameters). In a particular simulated trap profile, the IX density profile is estimated by a Maxwell-Boltzmann distribution. For each profile, the chemical potential is varied so that the total number of particles is consistent with the labeled relative change in excitation power. As the number of IXs increases, the distribution becomes much larger, spreading into the region of significant LH/HH mixing. The enhanced radiative rate in this region causes a non-monotonic intensity profile moving away from trap center. The force to produce this trap is unconstrained by any experiment.

mixing that requires close proximity of the valence-band states. For thinner wells, the confinement energy difference between the LH and HH states is larger. Thus, more force is required to bring the states together.

In addition, one prominent spatial feature supporting the LH/HH mixing origin is the shape of the dark region in contrast to the shape of the exciton cloud. Looking at the series of spatial images in Figure 20, it is clear that the hole does not share the anisotropic shape of the IX density profile, remaining roughly circular in the midst of a very elliptical population. With the anisotropy provided by a piezoelectrically-induced, spatially-varying Stark-shift, both the LH IX and HH IX should have roughly the same Stark shift at any location (apart from the small difference in their dipole moments), and, therefore, the LH IX trap shape should exhibit roughly the same elliptical shape as that of the HH IX trap. The LH/HH mixing argument relies solely on the difference in the LH and HH IX energies, and the anisotropy of the states does not exist in the energy difference between the states[3]. Thus, the spatially-varying oscillator strength arising from the valence-band state separation should be isotropic. So, this symmetry of the darkened region, in contrast to the predicted IX density profile, supports the mixing argument. In fact, it supports any darkening origin that relies on the energetic separation of the exciton states. For example, it could equally well support an argument relying on changes in degeneracy.

5.1.2 Linear Polarization Analysis

Linear polarization of the luminescence presents compelling evidence of significant mixing of states with differing angular momenta. In Section 4.2.9, the linear polarization at each position in the trap has been presented at low stress, at a stress with a darkened center, and at a higher stress where the center has brightened. In the lowest stress case, where the intensity is centrally peaked, the linear polarization is overall quite small. It is smallest in magnitude at the center and increases slightly moving away from the center. At the

[3]We must presume for this argument that the LH/HH IX repulsion is the same as the HH-HH IX repulsion, so that they have an equal blue-shift at all points. In the mean-field treatment, this is true, but in the model employing a temperature-varying anti-correlation one might expect that this is not necessarily true. For example, the interaction between two heavy hole IXs may be stronger due to increased penetration into the classically-forbidden region of interparticle separation (due to their lower in-plane mass).

stress showing the darkening, the same trend continues but with increased magnitude. The linear polarization remains nearly zero at trap center where the intensity is low, and it is dramatically larger away from the center. A previous report of the spatial pattern of this linear polarization was presented and corrected. There was a dramatic asymmetry between the linear polarization magnitudes along the horizontal and vertical directions in the old measurements. It was shown that the symmetry between the axes is restored if a few demonstrably bad data points are discarded. In the highest stress case, which was performed in a different sample, the linear polarization is again small at trap center, but the spatial variation of the magnitude away from the center lacks the symmetry of the lower stress cases. In addition, the intensity pattern shows a more symmetric, 4-lobed, clover-shaped pattern, rather than the 2-lobed, elliptical shape.

All of these polarization patterns are reproducible by valence-band mixing simulations, but the highest strain data from a different sample requires an additional mixing offset to account for the asymmetry of the polarization magnitudes along the [110] and [1$\bar{1}$0] directions. To predict the linear polarization, the components of the ground state are first determined from the eigenstates of the Pikus-Bir Hamiltonian at a given applied force, in the same way as in Figure 38(a) where the LH fraction was plotted except that the complex amplitude is retained rather than simply the LH and HH magnitudes. From the complex magnitudes, the linear polarization angle and magnitude are predicted for each point, as described in Section 2.3.1.

Figure 40 shows a comparison between the highest stress experimental data and a simulation of the linear polarization due to a high stress. The highest stress case is chosen to illustrate modeling of the most complex case. Simulating the lower stress cases, simply requires removing the mixing offset used here and decreasing the magnitude of the strains, producing a similar pattern as seen here but without the asymmetry in polarization magnitude. The upper half of the figure reproduces the upper half of the highest stress experimental data from Figure 32 but with more widely spaced points where the polarization is evaluated and increased line length to represent the linear polarization magnitude. The lower half of this figure shows the result of the simulation. The spatial variation of the linear polarization matches well with the experimental data. The direction of the linear polarization is

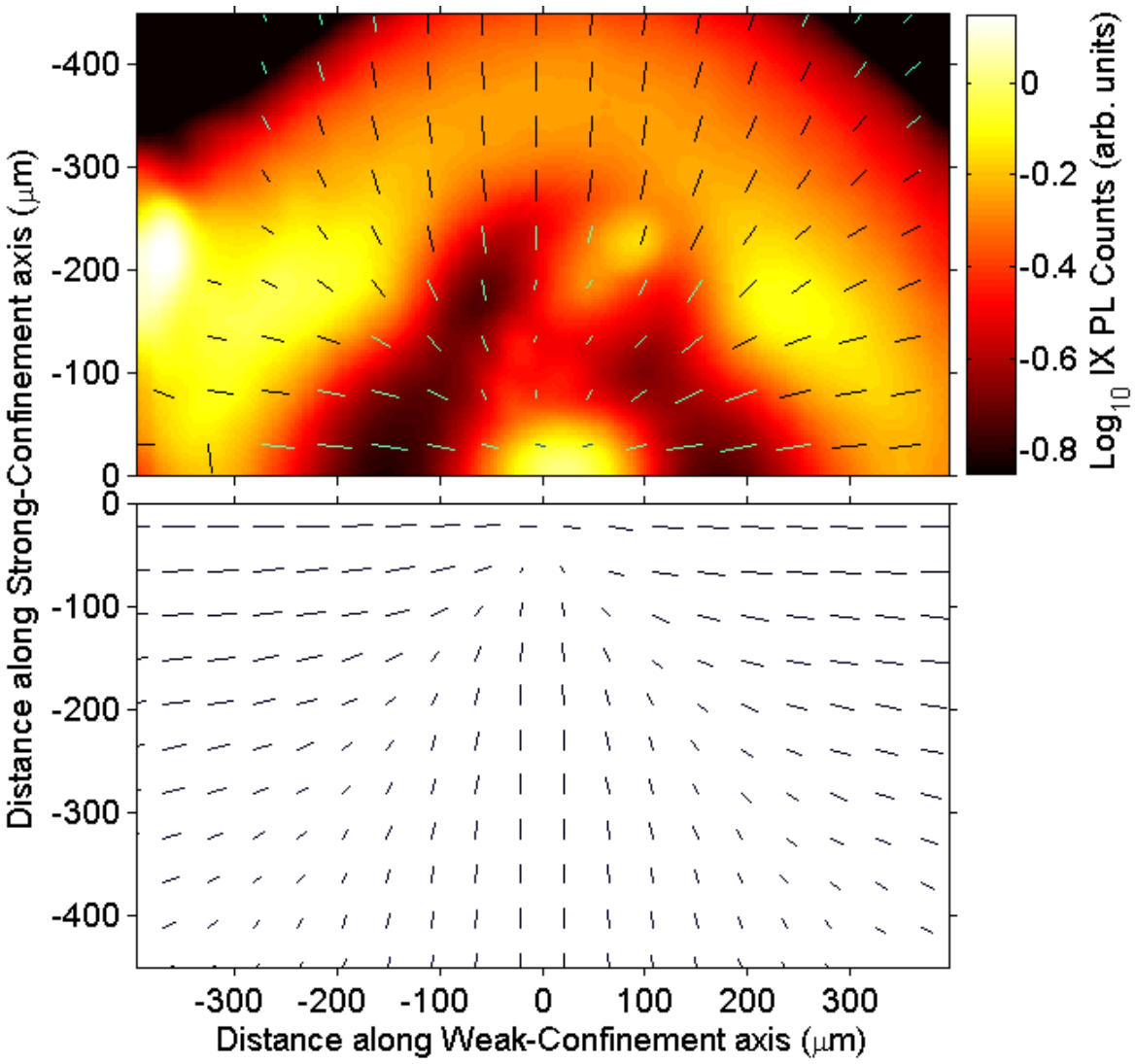

Figure 40: Comparison between experimental/simulated linear polarization maps. The upper plot reproduces the highest stress experimental measurement of the linear polarization from Figure 32, with fewer points and longer lines to indicate the linear polarization degree and magnitude. The lower plot shows the simulated linear polarization map due to mixing of the LH/HH state. A mixing offset was included in the simulation to account for the asymmetry between the [110] and [1$\bar{1}$0] directions and the non-monotonic linear polarization degree moving away from trap center in the vertical direction.

nearly radial, tending slightly more toward the [110] and [1$\bar{1}$0] directions, in both cases. The asymmetry in the linear polarization magnitude in this experimental data is most apparent in the darkened region, where the linear polarization is small in the vertical direction and very large in the horizontal direction. With no mixing offset, this asymmetry would not appear, so a mixing offset was introduced to reproduce the asymmetry. This is in accord with the low stress data from this unique sample, shown in Figure 33, where a significant degree of linear polarization was observed at very low stress at trap center. With the offset, the simulation matches the trend of the asymmetry, with the mixing enhanced along the horizontal direction and diminished along the vertical, with some degree of mixing at trap center due to the mixing offset.

So, from the linear polarization direction and magnitude alone, one might conclude that this supports the state-mixing model. Indeed, the linear polarization demands that the mixing is taking place, and the accord between the simulation and experiment establishes some confidence that we are treating the state mixing appropriately due to the strain. However, the relationship of the measured intensity profile and the measured magnitude of the linear polarization in this high stress case is directly contradictory to the model of mixing-induced darkening presented thus far. That model suggests that the brightest regions should be those with large degrees of valence-band mixing. This is fully consistent for the lower stress data, as the central dark regions have only a tiny degree of linear polarization. In the high stress data, the mixing offset causes the linear polarization pattern to shift so that the largest degree of linear polarization actually occurs in the darkened region on the horizontal axis (peaking at 70% linearly polarized). In some sense, then, the abnormality of the sample used in the highest stress case is quite fortunate, despite hampering direct comparison to the more normal lower stress data. It provides a case where the linear polarization due to the mixing changes greatly, but without the corresponding change one would suspect from this mixing change. This gives reason to doubt a causal relationship between the mixing and intensity patterning.

Coincidentally, the correction to previous data that was presented in Section 4.2.9, Figure 31, removes exactly the asymmetry from the linear polarization pattern of the lower stress data (in the more common sample) that is being emphasized in the high stress data as

vitally important. In the corrected case, there was a significant error in the data collection (seemingly, a bad region of the polarizing film sweeping through the data), observable as bad data points altering the polarization fits. This caused the linear polarization data to be skewed toward vertical polarizations overall, due to the low intensity area of the film sweeping through when the film was aligned to transmit horizontal polarizations. In the high stress case, which was performed with a different polarizing film, there is no evidence to support that the data was systematically skewed by experimental error, and the fits show no obvious trends of consistently bad data points, as in the corrected case. Thus, there is no apparent reason to doubt the measured polarizations in the high stress case, and the discrepancy between the intensity patterning and the measured polarization remains intact.

Overall, then, the linear polarization data suggests that state mixing does indeed occur, and the spatial pattern of strain-induced mixing is well represented by that produced from the Pikus-Bir Hamiltonian due to these strain traps. However, from the highest stress data, one must conclude that either the intensity pattern is not directly caused by this mixing, or there is some fault in the linear polarization measurements in the high stress data. That is, of course, additionally assuming that the mechanism for producing the intensity patterning is the same in both samples, so that the conclusion from the high stress case applies in all cases. The many similarities in the symptoms of this effect between the two samples (i.e. the onset parameters, darkening/rebrightening of trap center with strain), despite the few significant differences (i.e. the 4-lobed intensity pattern and the mixing offset), suggest that this assumption is logical.

5.1.3 Temperature Dependence

The natural explanation for the brightening of the trap center with increasing temperature, in the context of the valence-band mixing model, is that the LH IX state at trap center is becoming thermally occupied at elevated temperatures. This would certainly brighten the trap center luminescence. For this reason, three stress regimes were clearly illustrated in the experimental section, each demonstrating different thermal behavior. In the lower stress range, at low temperature the darkened center is present, and, with elevated temperature,

the ground state center brightens without the intervention of any spectrally distinct states. At much higher stress[4], the darkened center still occurs at low temperature, but a higher energy spectral line brightens with increasing temperature, sitting above what looks to be a still-darkened ground state. In the third stress regime, with just a bit larger applied force than when the thermally occupied LH IX state is apparent, the LH IX has become the lowest energy state, and the center is bright at low temperature, surrounded by a darkened region.

The second and third stress regimes showing thermal occupation of the LH IX state are perfectly consistent with the mixing argument. However, the brightening of the trap center luminescence in the lowest stress cases are left completely unexplained by valence-band mixing.

5.1.4 Lifetime Dependence on Strain

The mixing argument makes rather demanding predictions on how the radiative rate should change with the onset of the patterning. As Figure 38 illustrated, the onset of the relative darkening at the center of the trap should be driven by the growth of the faster LH recombination channel within the ground state. This necessitates that the population lifetime should decrease with increasing applied force. Furthermore, the lifetime should decrease dramatically at the stress where the LH IX becomes the lowest energy state.

Section 4.2.7 presented fits to the intensity decay of the IX luminescence, fitting the late and early decays separately. This treatment significantly clarifies the relationship between the decays and the darkening. In particular, Figure 26 demonstrates that the discrepancy between the late and early decay rates emerges precisely when the trap center begins to dim; the decay at late times becomes much slower as the darkening occurs. In addition, the early-time decay rate does not vary much with increasing stress, only increasingly slowly with increasing force, consistent with our previously reported results examining the decay only over a few lifetimes. Neither of the early nor late lifetimes are consistent with that required by the LH/HH mixing argument. In the case presented in Figure 26, the transition

[4]In the simulation of Section 5.1.5, the force required to predict the DX trap shape when the darkening first appears is 1.05N. The force required to predict the DX trap shape when the LH/HH IX are observed to cross is 1.9N, marking the transition to the third stress regime, where the LH IX becomes the lowest energy state and the center is bright at low temperature.

to the slower decay occurs after approximately 25 μs, after losing 75% of the total excitons. With this smaller population and the correspondingly lower interaction energy, the density will be much more concentrated at the center of the trap. Thus, it is natural to associate this change in the decay rate with a slower decay rate at trap center. Examining these results, the most natural interpretation is that, above some strain, the strain begins to cause the trap-center decay rate to become much slower. In the presented case, the late-time decay lifetime becomes about twice as long as the early-time decay and more than twice as long as the decays at low stress. The cause of this extreme change in the late-time decay rate is, as yet, unexplained.

The magnitude of this change in the lifetime cannot be explained by the piezoelectric effect and the concomitant decrease of the electron-hole overlap. Typically, over the field ranges in our experiments, a change of 25-50% in the electric field (depending on the value of the field) is required to effect a doubling of the lifetime. We can also make a prediction from the simulations presented in Section 1.3. The splitting between the zero stress DX and IX in this experiment was 33 meV, and, if we attribute this all to the Stark Shift[5], this sets the electric field at about 19 kV/cm, according to Figure 3(a). From the data presented in Figure 3(b), a 2-fold increase in the lifetime would require a change in the Stark shift of 9 meV, which is not possible from the piezoelectric polarization in the current range of applied forces. Furthermore, we are discussing the decay rate at trap center, where the piezoelectric effect is smallest.

Nearly as compelling as the increasing lifetime trend itself is the fact that this trend continues through the LH/HH IX crossing. This suggests that either the prediction of a fast LH IX decay rate is incorrect or that the relative exciton e-h overlap is not the primary factor determining the decay rate. This casts further doubt on the valence-band mixing explanation of the darkening.

[5]There is an additional source of this splitting, which is the dfference in the binding energy between the DX and IX. Since the DX binding energy is larger by several meV, the Stark shift predicted by Figure 3 is actually a bit larger than the total splitting. However, since a larger Stark shift corresponds to a region where the oscillator strength is less susceptible to the electric field, this would only strengthen the argument that the magnitude of the purported lifetime change is unphysical.

5.1.5 Reconciling Simulated Trap Energies with Predicted Mixing Fraction

Section 5.1.1 established that the LH/HH mixing argument can qualitatively explain the darkening with increasing applied force. Now, the parameters of the simulations will be evaluated quantitatively alongside experimental data to assess whether the simulation's predictions can be reconciled with experimental measurements. A series of spectral images of the DX and IX states at varying stress allows the DX trap shape to be predicted using a consistent set of parameters and the character, i.e. LH vs HH, of the IX state to be predicted. This is the same simulation as in Section 5.1.1, but now we also predict the DX and BiDX trap shape and require that the simulation parameters fit these profiles well so that the simulated forces are realistic.

First, for each spectral image, the energy of the DX and BiDX spectral lines are determined as a function of position along the spectrometer slit. It is not possible to determine the position of both lines at all positions, since the intensity emitted from the intrawell states is essentially between these two states. The BiDX state dominates at high density and, therefore, is essentially the only line seen at the center of the trap. Then, the trap shape is simulated for each force using consistent parameters, varying only the force to match the DX and BiDX trap shapes. Just as in the fits of Section 4.2.1, the BiDX energy is predicted by simulating the DX state and subtracting 1.3 meV. Now, the LH fraction in the IX ground state can be predicted for a given spectral image, with some certainty in the result since most of the parameters are fixed by the DX and BiDX trap fitting.

Of particular interest are images showing the cases just below and just above the force where the darkening appears. For the model to be valid, the profiles of the LH fraction in these boundary cases must be such that the contrast between the center/sides increases dramatically between these forces.

The two spectral images marking the boundary of the darkening onset in this stress series are displayed in Figure 41 as the backdrop to the analysis results. Figure 41(a) shows the lower stress case, where the intensity profile is singly-peaked at trap center. Figure 41(b) displays the sample under slightly higher stress, where the peak intensity is observed 85 μm from the center, with an intensity 1.5$\times$ that of the center. The spectrally-integrated

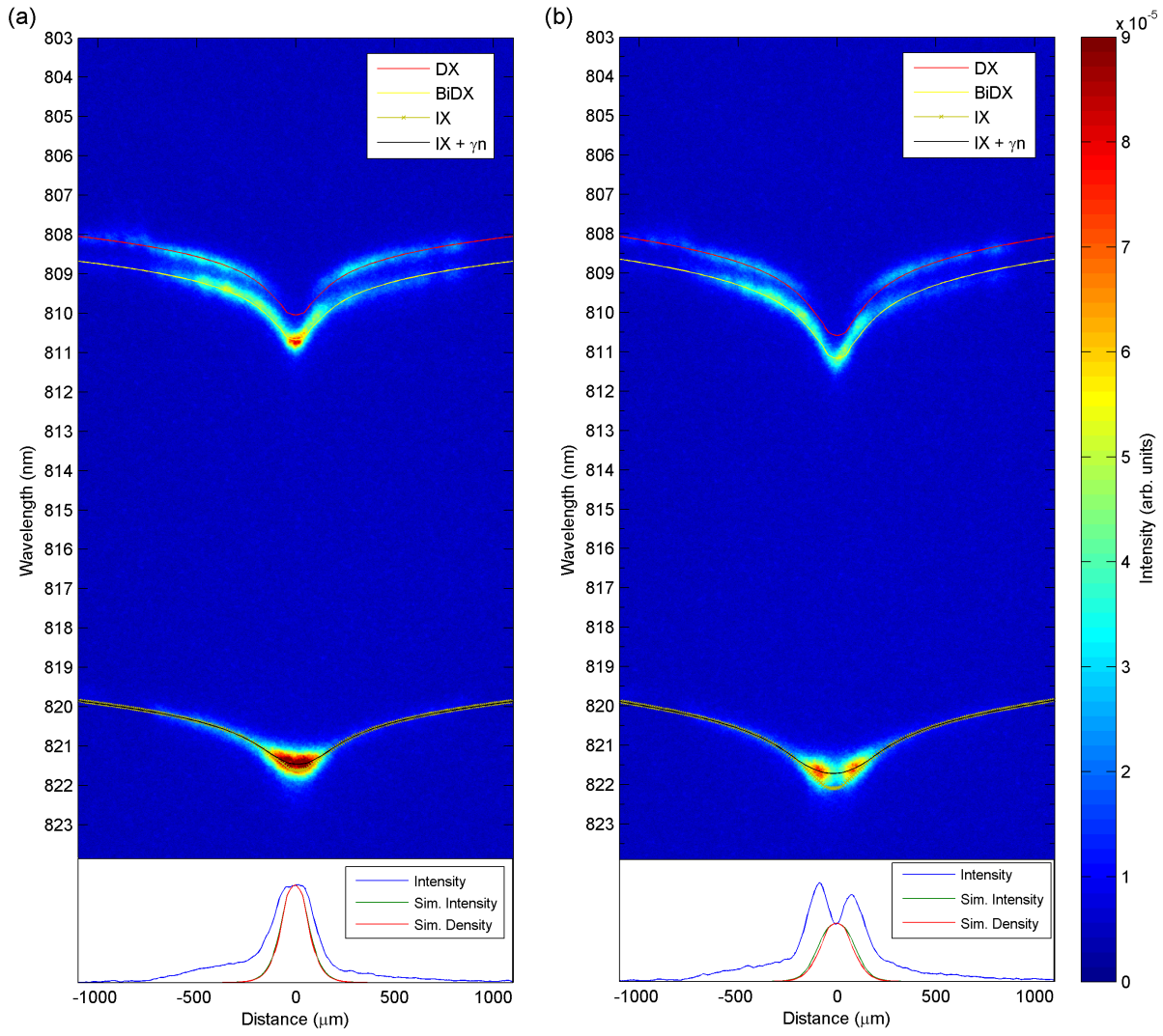

Figure 41: Comparison of experimental spectral images to simulated energies and intensites from LH/HH mixing theory. The two spectral images in the background of the plots occur at the stress boundary of this effect, with plot (a) occuring at a slightly lower stress to the darkening onset and the plot (b) just above this transition. For each case, the DX and BiDX trap energy profiles have been fitted to determine the force applied to the sample. The red and yellow lines indicate the fitted DX and BiDX states, respectively. The force determined from the DX fit is used to predict the IX trap shape, plotted in tan on each image. The IX-IX repulsion causes the discrepancy between the predicted IX trap shape and the measured IX spectrum. This density-driven blue shift is used to estimate the IX density profile, and the estimated density is plotted in red on the lower axis. From this density profile and the simulated LH fraction profile, the intensity profile is estimated and plotted in green on the lower plot. The measured spectrally-integrated IX intensity is also shown on the lower plot for comparison.

IX intensity is displayed below each image. The DX and BiDX states are fitted to an applied force with the following fixed parameters: ϵ_{xy} offset = 0.0, Piezoelectric constant = 5.0, and the resulting energy plots are overlaid on each image. The IX state is then predicted from this force, with $\Delta E^{IX}_{LH/HH}$ of 7.3 meV, allowing only an overall shift of the entire line to account for the IX Stark shift. This predicted line differs from the actual IX energy at trap center due to the density-driven blue shift, as is clear from the image. In a mean-field treatment of the interaction, this blue shift is linear with density and, therefore, allows estimation of the relative density profile from the observed shift[6]. Again, assuming a Maxwell-Boltzmann occupation for the equilibrium density, the relative density profile can be iteratively determined to achieve an IX density blue-shift that matches the difference between the measured and predicted IX energy at trap center. The Maxwell-Boltzmann distribution achieving this blue shift at 3.5 K is displayed in the lower plot, and this blue shift is added to the predicted IX energy and overlaid on the image to display the correspondence with the actual spectral line. From the IX simulation, the LH fraction is determined and the radiative rate profile predicted as a function of position in the trap. This radiative rate profile is multiplied by the predicted density profile to simulate the intensity profile, and this is also plotted in the lower axis. These intensity profiles should roughly reflect the observed intensity profile, if the mixing mechanism is to work.

As seen in the plotted simulation, this parameter set does not provide the necessary mixing to cause a darkened center. The radiative rate profiles are not directly plotted here, but the ratio of the peak rate to center rate is 1.12:1 in the low stress case and 1.25:1 in the high stress case. Here, it is clear that this is insufficient to cause a non-monotonic intensity moving away from trap center, as the predicted intensity profiles almost exactly overlap the estimated density profiles. Since the estimated density profile is rather small, this ratio actually needs to be about 2.6:1 to produce the observed intensity ratio between the trap sides/center in the higher stress case. This requires that the ground state on the side is composed of almost 20% LH IX, with a wholly unmixed center (with no strain offset). A much larger density profile would alleviate some of the difficulty of producing this intensity

[6]We estimate the "relative" density profile here, giving no indication of the absolute densities. This allows us to avoid the issue of the actual value of γ, the mean-field shift per density.

profile; if the density were roughly constant, the ratio would need to be just over 1.5:1. However, it is difficult to see how an equilibrium density profile could be much broader with roughly the same final shape of the spectral line. On the other hand, a larger profile could be due to a non-equilibrium occupation. These images are pumped with a slightly defocused laser so that the entire DX trap shape is illuminated. Since the IX lifetime is very long, it is assumed that roughly an equilibrium population is reached, but the fact that some of the light is radiating before reaching the center is obvious from the shape of the real intensity profile in the lower axes in Figure 41, where there are tails of the intensity profiles out to the far exterior of the trap. Allowing for the possibility of a much flatter, nonequilibrium distribution, one might consider that a rate ratio more similar to 1.5:1 might suffice to create the pattern. However, the mixing from this set of parameters remains insufficient to achieve this profile.

A natural next step is varying the less constrained parameters, $\Delta E^{IX}_{LH/HH}$, and the mixing offset, since they offer very little modification to the DX energy (of course, the IX splitting offers no change to the DX energy). Since the primary question at hand is whether a certain force is able to provide a large enough mixing term or push the states close enough together to achieve sufficient mixing, these terms are at the heart of this prediction. However, reevaluating these terms actually leads to intensity patterns that less accurately match those observed.

First, consider altering $\Delta E^{IX}_{LH/HH}$. In the previous analysis, this is set to be the same as $\Delta E^{DX}_{LH/HH}$. From the singular experiment where the IX LH spectrum was able to be observed, in Section 4.2.6, it was noted that the splitting of the IX states was 1.7 meV larger than the DX LH/HH splitting at zero electrical bias, and we expect this separation to become slightly larger with increasing electric field, in accord with the slight difference in dipole moments of the states. So, a natural starting point for modifying the IX predictions would be to set $\Delta E^{IX}_{LH/HH}$ to 9 meV. However, this makes the situation worse. Now the states are farther apart at the same applied force, so the mixing is reduced.

Despite this problem, there is additional evidence that the splitting is larger than the 7.3 meV splitting of the DX state. Moving to images of higher applied force, a 7.3 meV splitting predicts that the LH IX state should cross the HH IX state at a force (more precisely, at a

DX trap depth) much lower than where the center is actually observed to brighten. Believing it to be the case that the high-stress brightened center is due to the LH IX crossing, one must assume that $\Delta E^{IX}_{LH/HH}$ is actually larger than 7.3 meV. If the DX trap is plotted and fitted for the spectral image corresponding to first observation of high-stress brightening, it is seen that at this applied force the bare LH state will shift downward by 10.7 meV more than the bare HH state[7], so this suggests that $\Delta E^{IX}_{LH/HH}$ is closer to 10.7 meV. In any case, the splitting is much larger than that required to observe significant mixing in the experimentally observed boundary case. In fact, $\Delta E^{IX}_{LH/HH}$ would need to be about 6.3 meV to achieve the more forgiving 1.5:1 rate ratio.

Modifying the mixing offset from zero also makes the situation worse. While it increases the mixing overall, the trap center now becomes a mixture of LH and HH, which tends to reduce the contrast between the trap sides and center. For example, introducing a 0.05% ϵ_{xy} offset modifies the 1.25:1 ratio, observed for the high stress case with $\Delta E^{IX}_{LH/HH}$ of 7.3 meV, to a 1.17:1 ratio. So far, some evidence has been seen that there does exist some offset mixing, e.g. in Section 4.2.1, where the DX and IX energies were fitted in 2D[8]. So, the likelihood that LH/HH mixing is producing the pattern is further reduced.

The parameters of this simulation can be compared with that presented in our previous publication to see what has gone wrong with the qualitative analysis. First, observe that the forces quoted in the previous publication are much larger than the forces used in the current analysis. There, the LH/HH crossing is observed at a force of about 4N. In all of the fitted data for the entire stress series, the forces are found to be always less than 2.5N. The force required to fit the DX trap when the the IX LH/HH crossing is observed is only 1.9N. The discrepancy is essentially due to the fact that the previous simulation was not constrained by fits to DX data. So a value for $\Delta E^{IX}_{LH/HH}$ was chosen, also unconstrained by experimental data, and the appropriate force was applied in the simulation to cause the states to approach and cause valence-band mixing. In the previous case, the assumed $\Delta E^{IX}_{LH/HH}$ was much larger than that used here, closer to 20 meV. With this large splitting,

[7] In the Pikus-Bir Hamiltonian, if one ignores the mixing terms, this is essentially determining (P-Q)-(P+Q) = -2Q = 10.7 meV

[8] In addition, the linear polarization data in some cases also necessitates some mixing offset, as seen farther on in Section 5.1.2.

the forces required to push the states closer together are much larger. Thus, when the states approached, the off-diagonal strain mixing the states was much larger, and the mixing between the states was greater. One might argue that, since no real upper bound has been placed on the $\Delta E^{IX}_{LH/HH}$ in the data presented, one might simply increase the splitting in the current simulation to 20 meV. The problem remains that this analysis constrains the applied forces by examining the shape of the DX trap for a particular IX intensity profile. The force required to overcome such a large LH/HH IX splitting would produce an extremely large shift of the DX states, which is not observed. With the forces so constrained, increasing this splitting in the simulation would serve only to decrease the amount of mixing observed at a particular force, as observed above. Thus, we are able to explain the discrepancy with the previously published account but unable to modify the parameters of this simulation to achieve the same results.

5.1.6 DX Darkening

Despite the problems offered so far with the mixing argument, one axiom of that argument, namely that there is a large contrast in the brightness of LH and HH states, offers an explanation for the fact that the DX ground state also darkens with increasing force, as seen in Section 4.2.4. The darkening seems to be consistent with the LH DX state crossing the HH DX state to become the ground state at trap center, since the LH DX state should have a lower recombination rate. The three spectral images chosen to demonstrate this effect in Figure 21 are part of the same series of increasing stress to which DX trap shapes were fitted in Section 5.1.5. The same fitting procedure may be applied to these images to determine the fraction of LH states in the lowest DX state at the point when the DX state darkens.

Figure 42 shows a spectral image of the DX and BiDX luminescence, the higher energy portion of the highest stress case image of Figure 21, where the DX state darkens. The simulated DX energies are plotted atop the spectral image. Below the image, the LH DX fraction in the lowest DX state is plotted as a function of position. The sharp spike up to 1 at trap center shows that, at this applied force, the LH DX state has just passed the HH DX state exactly at trap center. This establishes that the DX darkening occurs at precisely

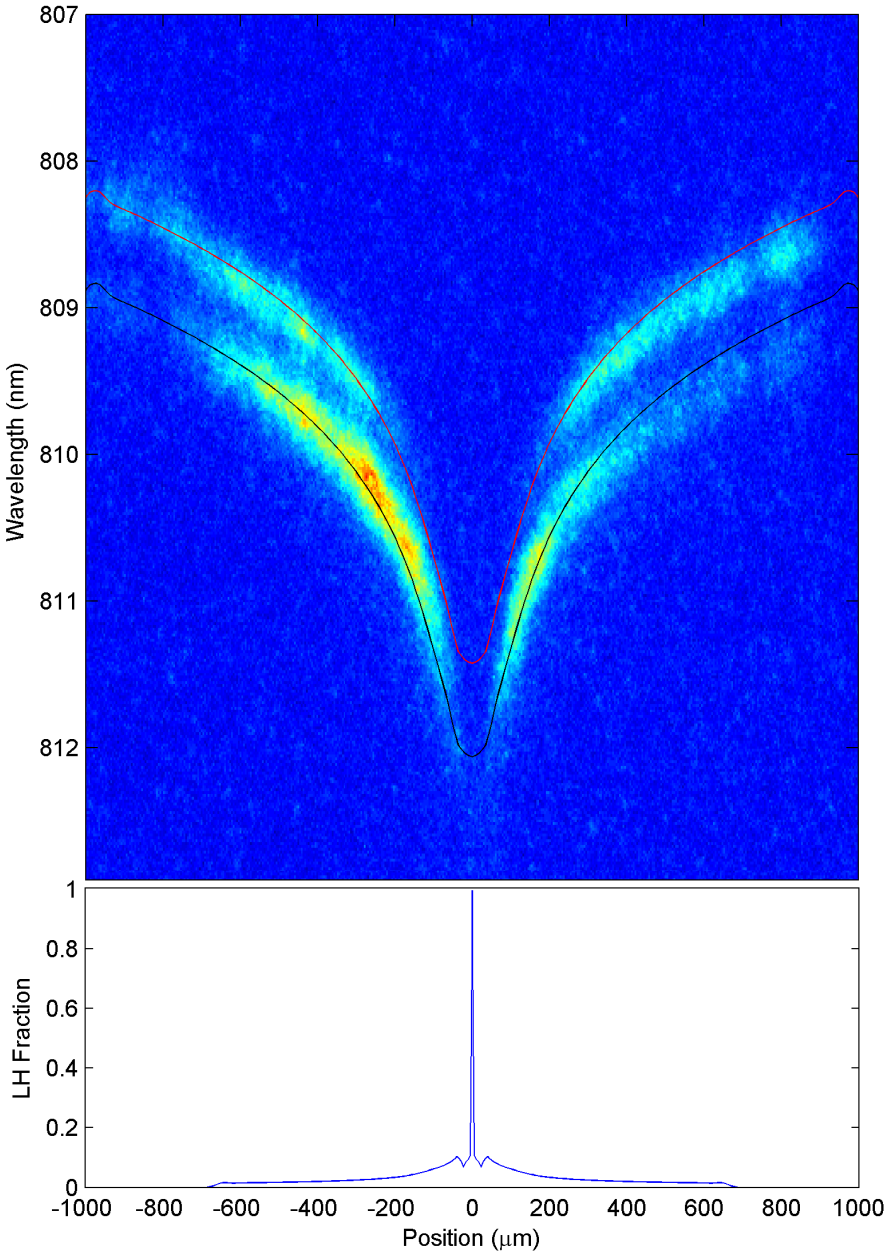

Figure 42: Spectral image of DX darkening and predicted DX LH fraction. The highest stress spectral image from Figure 21 is reproduced, and the DX and BiDX trap shapes are fitted using the experimentally established $\Delta E^{DX}_{LH/HH}$ of 7.3 meV in this sample. The resulting LH fraction in the DX ground state is plotted below the image, demonstrating that at this stress the DX LH/HH are predicted to cross.

the point at which the states cross, validating the prediction that this darkening is caused by the dimmer LH DX state.

5.1.7 Conclusion of Valence Band Mixing Analysis

We have examined a variety of aspects of this system, looking for correspondence between the state-mixing darkening mechanism and experimental measurements, and there has been mixed results. The arguments in favor of this mechanism are compelling, but all are qualitative. To review, those are:

- A-1 With a particular range of simulation parameters, this mechanism is able to predict this intensity pattern emerging with both stress and density.
- A-2 The isotropic shape of the darkened region is consistent with the isotropic nature of the LH/HH splitting (and not the energies of the individual states).
- A-3 The onset of darkening appears at reduced stress for wider wells, consistent with the reduction of the LH/HH splitting with reduced confinement.
- A-4 The measured linear polarization pattern matches well with that predicted from valence-band mixing due to strain.

On the other hand, there are serious problems with this mechanism. These are:

- B-1 There is no apparent explanation for the temperature dependence of this patterning in this model
- B-2 Constraining the strain simulations with the observed trap shapes, at the stress where the darkening occurs, the predicted IX LH/HH mixing is insufficient to produce the observed darkening.
- B-3 Mapping the linear polarization at very high stress showed a case where the linear polarization is maximized in the darkened region. If the mixing fraction determines the intensity, the linear polarization should always occur when the intensity is high.
- B-4 The effect of strain on the IX lifetime is entirely inconsistent with the emergence of a new faster recombination channel.

The lack of a predicted temperature dependence has been evident from the start of this investigation. The only obvious prediction of a temperature dependence is the thermal activation of the LH IX state, a behavior that has been carefully examined and shown to occur only at the highest stresses. However, the lack of ideas to fit this requirement could only reflect a creative failure on our part, and does not rule out a subtle temperature dependence that has been overlooked[9]. On the other hand, the last three of these items are in direct

[9] A suitable explanation for the temperature dependence must not only explain how the pattern could disappear with increasing temperature but also why this transition temperature increases for increasing density, as demonstrated previously [78].

contradiction to the brightening mechanism. To salvage this mechanism, one must discredit the simulations in Item B-2; provide an additional mechanism to explain the 'special case' of Item B-3, where the linear polarization magnitude was decoupled from the brightness in a particular sample; and explain how the predominant factor determining the emission profile seems to only influence the total emission rate in a contradictory manner.

So, after a thorough evaluation of the experimental evidence, it seems that there are two effects of the stress occuring simultaneously. The stain-induced valence-band mixing is certainly occuring, as required by the measured linear polarization. In addition, there is some other mechanism causing the darkening at trap center. While this analysis was unable to fully explain the behavior, the knowledge of the single-particle spectrum gained from this analysis of strain-induced valence-band mixing will certainly be an important part of future studies in the system.

5.2 IONIZATION AND ELECTRON-HOLE LIQUIDS

The previous sections have focused on darkening due to the varying oscillator strengths of particular excitonic states. The heavy-hole IX state has a lower radiative rate because of its intrinsically lower electron-hole overlap. For a similar reason, an ionized population of electrons and holes will also have a diminished overall recombination rate due to the reduction of electron-hole spatial correlation. So, ionization should also be considered as a possible mechanism for darkening, if there exists a means to explain the experimentally-observed temperature, density, and strain dependences. Considering ionization also has the benefit of explaining the increased overall lifetime that eluded explanation with a mixing argument.

Typically, ionization of excitonic populations occurs at elevated temperatures and/or density. At high temperature, carriers are easily able to overcome the exciton binding energy. At high density, the Coulomb attraction between electrons and holes becomes screened, and the binding energy is reduced. Furthermore, the thermal ionization of a small fraction of a population increases the screening and reduces the ionization barrier for the remaining excitons. Thus, the cascading effect of a small amount of thermal ionization can cause

full ionization of the population to occur at temperatures well below what one might expect strictly from the temperature and low-density binding energy [71]. This transition is referred to as the Mott transition, or ionization catastrophe. This, however, remains an effect that occurs at increasing temperature. In the case at hand, the darkening of the trap-center PL occurs at reduced temperature, transitioning in the range of 2 to 10 Kelvin, in the range of these experiments. On the other hand, there is precendence for low-temperature ionization of excitons in the context of electron-hole liquid (EHL) formation, and, notably, there is also an important role of strain in this phenomenon.

Electron-hole liquids form at high carrier density and low temperature, typically in the presence of high state degeneracy, in a very similar manner to the liquefaction of atomic gases. As is always the case, the gas/liquid transition is governed by a competition of potential and kinetic energy[10]. In most gases (with the exception of the IX gas considered here), there is an attractive interaction between molecules, favoring increased density. However, increasing the density will increase the Fermi level of the fermionic constituents of the system. The result of this competition is typically a minimum total energy for some density, favoring a liquid state with a fixed density. If this energy minimum is deep enough, so that the energy savings per particle is greater than zero-point fluctuations, there will be a gas to liquid transition at some finite temperature. So, the depth of this energy minimum is an extremely important parameter in determining the liquid stability and transition temperature, and this quantity is strongly modified by the degeneracy of the occupied states.

Increasing the state degeneracy causes the Fermi level to rise more slowly with density, reducing the kinetic energy cost of increasing the density. This increases the depth of the energy minimum and shifts the minimum to occur at a higher density. This effect was demonstrated clearly in the case of bulk Ge under [111] strain by Simon, Sterenka, and Wolfe [68]. In unstrained Ge, there is a 4-fold degenerate conduction-band (the $\langle 111 \rangle$ valleys) and two-fold degenerate valence-band (LH/HH at zone center). EHL is stable in this system at a density of $2{\times}10^{17}$ cm^{-3}. With the application of a moderate strain in the [111] direction, the degeneracy of the conduction-band is reduced, as the splitting between the lowest valley

[10] An overview of EHL and their relation to atomic gases is presented by Keldysh [28]. The main, relevant points of that discussion are summarized here.

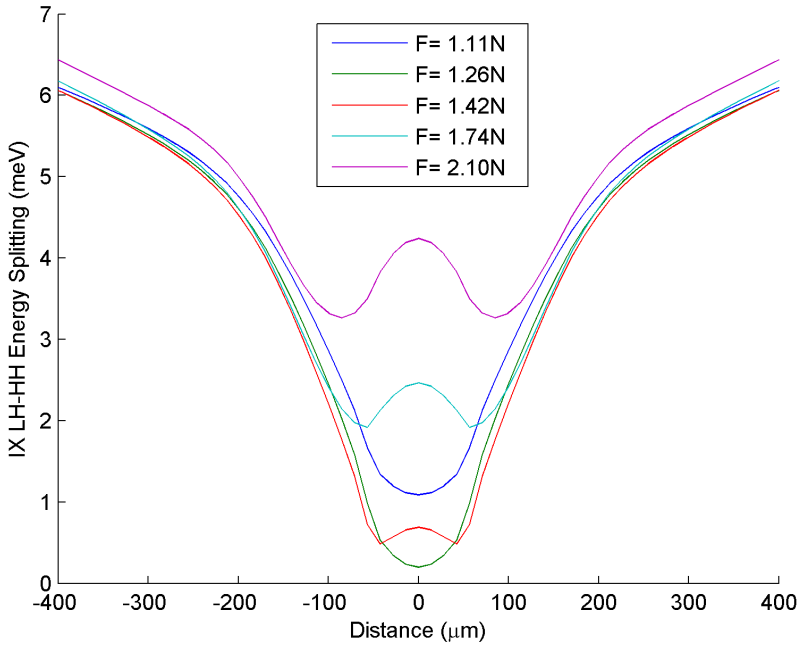

Figure 43: Simulated LH/HH IX splitting vs position for increasing applied force. The lowest force (blue) shows a splitting that is smallest at trap center. Increasing the force shrinks this splitting at trap center until the lines cross. The splitting does not reach 0 at any position away from the center because there is a non-zero mixing at these points. No mixing offset was employed in this simulation. In the highest stress case (purple), the off-diagonal strain is large enough to cause over 3 meV of splitting where the lines would cross (at just under 100 μm from the center).

and the upper valleys becomes greater than the electron Fermi level[11]. With further increased strain, the valence-band loses its degeneracy as well. The liquid is still stable in each of these cases, but the liquid density reduces by a factor of three as the conduction-band degeneracy is lifted and a total factor of about 20 when all of the degeneracy (apart from spin) has been removed.

The parallel to the effect of strain in our system is then easily drawn in comparison to this case. In contrast to the experiments in bulk Ge, the degeneracy is low in the case of unstressed quantum wells. With increasing applied force, the LH and HH state separation is reduced. Since increased degeneracy has a dramatic stabilizing effect on the EHL state and, in the case at hand, the valence-band degeneracy is being increased, EHL formation perhaps offers an explanation for the observed transition. One could easily imagine a scenario applicable to this experiment. Specifically, the center darkens as the splitting in the center becomes small compared to the either the Fermi level or k_BT. At increasing force, the states cross at trap center, so that the degeneracy is highest now at the sides. This would correspond to the center brightening as the sides become the darkened region, consistent with our highest stress results. The liquid would become unstable at higher temperature and transition back to a gas of bound excitons, which has a roughly uniform recombination rate across the trap.

However, first it is important to address the important discrepancy between the typical EHL description and the IX case: the repulsive IX-IX interaction. If we consider a molecular liquid with repulsive interactions, the previous discussion of potential vs kinetic energy makes little sense as both are positive energies. As mentioned in Section 1.4.2, in our CQW system, there is no IX-IX separation at which the interaction potential is negative. Therefore, it is difficult to imagine a situation in which a liquid of interwell excitons could form. In contrast, one could consider the traditional metallic (ionized) EHL case, composed of loosely-correlated electrons and holes instead of excitons or biexcitons. A few theorists have numerically investigated the possibility of EHL in coupled wells. First, Lozovik and Berman [41] have investigated the case of excitonic liquids in the case of smaller well separations (so that there is some attractive component), finding that an excitonic liquid is possible for well separations

[11]The Fermi level is the relevant energy scale to determine degeneracy in this case, as it determines whether multiple states will be occupied and contributing to a reduction of the Fermi level at some density. However, if k_BT is large compared to the Fermi level, then k_BT is the appropriate energy scale.

d<1.9a_B^*, where a_B^* is the 2D bohr radius. However, for d>1.1a_B^*, the minimum in the total energy vs density is only a local minimum, making the state only metastable. The 2D Bohr radius is half the 3D Bohr radius: a_B^*=5.7 nm. In accord with the previous assessment that the well-separation in our case is too large to support attractive interactions, the 18 nm well-center separation (the e-h separation will be slightly larger than this due to the Stark effect polarization) puts this IX system well out of the range of a stable or meta-stable excitonic liquid. Babichenko and Polishchuk [8] have numerically investigated the stability of the ionized interwell case. Assuming the number of degenerate bands ν to be large and expanding the interactions in the small parameter $1/\nu$, they show that the energy of the ionized system decreases with increasing density and that this energy is always lower than that of an excitonic population. This suggests that the metallic EHL is possible in this system if the number of degenerate states is large, though they do not suggest how large this degeneracy must be to achieve stability.

In addition, there has very recently been an experimental claim of a liquid phase in an interwell system very similar to ours but without applied strain [75]. This experiment has a similar structure, but confining the IXs on a 100×100 μm^2 mesa. Increasing the excitation power, a darker region is observed to emerge on the sample, with well-defined but varying boundaries. On the time-scale of seconds after the excitation is turned on, this 'droplet' forms and varies its shape. The lifetime in the 'liquid' region is measured to be 70 ns, which is twice that of the 'gas' region. All of this seems fairly compelling, but there are many issues with the experimental interpretation. First of all, the authors claim that the gas phase that occurs at a lower excitation power is actually an ionized interwell population (they are starting above the Mott transition described above), and the liquid phase is described as excitonic. If we accept that the population is ionized in the low-density regime, there is no reason to believe that the e-h attraction will not be screened at even higher density. In addition, the decreased radiative rate of this liquid state certainly suggests that the population is ionized rather than excitonic. The excitonic radiative rate enhancement, from the increased electron-hole correlation, is $\frac{1}{n\pi a_B^2} \sim 4$ at a density of 4×10^{10} cm^{-2}, which is their estimated density of the liquid state. This suggests that the population may indeed be ionized in the liquid state. Unfortunately, from the additional details of the experiment,

there is also reason to doubt the fact that they were even looking at an interwell population. The authors start the paper by showing a plot of the IX peak PL energy vs excitation power, demonstrating a strong blue shift of the IX line with increasing power and that this blue shift saturates when the IX line is shifted up to the DX energy. This shows that you can completely remove the Stark shift with increasing power. However, this saturation occurs at an excitation power of 20 μW, and only at a power ten times larger than this do they observe the liquefaction transition. At powers above this saturation power, the lowest energy states are actually best described as intrawell (DX) states[12]. So, at the excitation power where the liquefaction occurs, it is likely that they are actually seeing an intrawell EHL. Despite my interpretation of these experimental results, the existence of this study at least demonstrates that the experimental CQW community considers this a possible scenario, which is reason enough to examine this as the mechanism for our PL darkening.

From the experimental evidence presented, the strain seems to be one of the most important factors influencing the darkening onset. From the EHL perspective, the strain has the effect of increasing the degeneracy of the valence-band states, as the LH and HH are pushed closer together with increasing strain. This establishes a criteria for fitting our system to the EHL model. If the IX state darkens when the LH and HH state are close together, within the hole Fermi level or k_BT, then perhaps the EHL description is appropriate. If we consider the upper range of densities in these experiments, these correspond to a blue shift of approximately 5 meV[13]. The two theoretical predictions for the blue shift for a given density, the mean field approximation and the estimate considering IX-IX anticorrelation, represent approximately the upper and lower limit on this interaction strength. From Section 1.4, the mean field estimate is $\gamma = 2.6 \times 10^{-10}$ meV cm^2, and with correlations $\gamma = 2.0 \times 10^{-11}$

[12]In their case, they are using unequal well-widths, 12 nm and 18 nm. So with no Stark shift, the lowest energy state is a DX state (or intrawell free e-h if the Coulomb attraction is fully screened at this density) predominantly within the wider well. There are scenarios where one could expect interwell excitons to dominate without an applied electric field. One such is demonstrated by Kukushkin, Rossokhaty, and Schmult [34], where a wide barrier is present between two asymmetric wells. The narrow well is then resonantly excited. The barrier prevents fast tunneling to the energetically favorable wide QW, but the low electron mass allows it to more easily overcome this barrier. In this way, the electrons may preferentially occupy the wide well with the holes stuck in the narrow well. This is decidedly not the case in this experiment, though. They are exciting higher in energy than both the narrow and wide wells, beginning with neutrality in each, and the 3 nm $Al_0.28Ga_0.72As$ barrier between the wells is insufficient to forbid hole tunneling within the carrier lifetime.

[13]Larger blue shifts are certainly achievable, but not typical in our experiments.

meV cm^2. So a 5 meV shift corresponds to a density from 2×10^{10} to 2.5×10^{11} cm^{-2}. If we consider the density of states of a flat 2D potential, since the harmonic trap is essentially flattened at high density, with a hole degeneracy of 2 and using the HH in-plane mass ($0.12m_0$), the low density estimate corresponds to a hole Fermi level of 0.4 meV, and the high density estimate corresponds to a hole Fermi level of 5 meV. The large Fermi energy associated with the high density estimate (corresponding to the lower 'correlation-corrected' estimate) actually suggests that a good deal of the IX blue shift is due to the electron and hole Fermi levels and that one cannot actually use this theoretical blue shift to directly calculate the density without considering the Fermi energy shifts. This actually suggests a basis for the very rough experimental measurements aligning more closely to the mean-field shift – the IX-IX Coulomb energy may be smaller than the mean-field estimate but there are Fermi level shifts that also contribute a non-negligible blue shift[14]. For the purpose of a density estimate then, we will use the mean-field approximation and determine a hole Fermi level of 0.4 meV. This is still larger than k_BT in many of our experiments, which at 2 K is 0.17 meV. Thus, the hole Fermi level will serve as the approximate energy range to determine degeneracy.

Now, using the strain simulations from Section 5.1.5, the splitting between the LH and HH states can be determined as a function of position for varying applied force. Figure 43 shows the simulated LH/HH splitting at positions through trap center. There is no mixing offset employed in this simulation, so the states will cross at the exact center of the trap. Before the states cross, the splitting is smallest at trap center (in the lowest two forces shown, in blue and green). We can see that, of course, there is no problem with the trap center splitting being small. At increasing force, the center will cross and then the region

[14]This highlights the point that the Fermi level shift and correlation-corrected blue shift are actually similar in magnitude, and they are both linear in the density. If one wanted to calculate the total blue shift at some density one might simply take the sum of the Fermi levels of electron and holes and the IX-IX blue-shift:

$$\begin{aligned}\Delta E &= \left(\frac{\pi\hbar^2}{m_e} + \frac{\pi\hbar^2}{m^t_{HH}} + \left(2.0 \times 10^{-11}\ \text{meV cm}^2\right)\right) n \\ &= \left(\left(3.6 \times 10^{-11}\ \text{meV cm}^2\right) + \left(1.99 \times 10^{-11}\ \text{meV cm}^2\right) + \left(2.0 \times 10^{-11}\ \text{meV cm}^2\right)\right) n,\end{aligned} \tag{5.4}$$

where m^t_{HH} is the in-plane mass of the heavy hole, $0.12m_0$. A total blue shift of 5 meV then corresponds to a hole Fermi level of 1.1 meV and an IX-IX repulsion blue shift of 1.2 meV, with a density of 6×10^{10} cm^{-2}.

of crossing will move outward from the center. However, at positions away from the center there is substantial mixing due to the strain, so that the splitting is never zero. If using 0.4 meV as the degeneracy criteria, the case in red, where the lines have just crossed at trap center, shows the maximum force at which some part of the trap shows this splitting. Above this force, the crossing occurs with enough LH/HH mixing to split the states more than this degeneracy criteria. The point of smallest splitting on the red curve occurs at about 50 μm from the center. This is essentially the largest that the dark region can grow with the current criteria. This is in stark contrast to the experiments. While the darkened region is sometimes this small, it can be seen to extend out to about 200 μm from the center, particularly when the center has brightened and the dark region occurs on the periphery, see the image in the background of Figure 40, for example. This could be remedied by allowing a larger valence-band Fermi level, of course. Permitting the Fermi level to be several meV could allow the dark region to extend this far from trap center.

There are additional problems with fitting this degeneracy model to the strain simulations. As demonstrated in the discussion of LH/HH mixing, our simulations show that the darkening at trap center occurs when the LH and HH are still well separated in energy. In the mixing model, this may have been accounted for by a large degree of mixing even at this lower stress (though it turned out not to have been). In this case, there is no getting around the fact that the states must be very close in energy to call them degenerate. In addition, Section 4.2.8 firmly establishes that the LH and HH actually cross at the point when the center brightens, by demonstrating the thermal activation of the upper state at a slightly lower stress and the low temperature occupation at a slightly higher stress after they have crossed. This provides a further contradiction to idea that the darkening is driven by degeneracy, as the darkening should first occur approximately at this stress. Of course, this could also be remedied by allowing a very large criteria for degeneracy, so that the center could darken many meV before crossing. The center brightening when the states cross would then have to be caused by a different phenomenon, since the degeneracy would remain high at this point. This could perhaps be resolved by invoking the increased oscillator strength of the LH IX state or the fact that the LH state would support a stable EHL at an increased density due to its larger in-plane mass. However, the allowance of an extremely large valence-band Fermi

level is too speculative to warrant further analysis in this vein.

Therefore, the effect of strain in our system does not seem to match with the degeneracy enhancement suggested by the EHL model. This does not completely rule out the possibility of an interwell EHL causing our darkening. One could alternately consider a transition without (much) added degeneracy, occuring at higher strain simply because the trap is steeper. However, the experimental evidence seems to suggest that the darkening is most sensitive to the LH/HH state separation, rather than the trap depth itself. This is primarily shown by the well-width dependence of the transition – requiring lower strain with increasing well widths (requiring a smaller shift for smaller initial state separation). So, the evidence seems to be pointing away from the presence of an interwell EHL.

5.3 BOSE-EINSTEIN CONDENSATION

The failure of any feasible variants of the previous models to account for the dependence of this darkening on the experimental parameters, allows us to consider the dark BEC state despite having no direct evidence to support it, as this state naturally includes roles for the trap potential, temperature, and density with, qualitatively, the observed dependencies. The dark BEC scenario that would describe this situtation consists of a dark population exclusively occupying the center of the trap and the bright uncondensed population pushed to the sides. This phase separation can occur because the interaction strength between condensed and uncondensed particles should be larger than between condensed particles. This follows from the requirement to symmetrize the boson wavefunctions. This is the same effect stabilizing an interacting condensate from fragmenting into competing populations. For example, for short-range interactions, this condensate-condensate interaction is half that of the condensate-normal interaction [76]. So, if the particles condense into a dark state, that state might preferentially occupy the trap center.

Collaboration with theorists regarding this issue has allowed this simplest case to be dismissed based on the behavior of the intensity profiles with increasing density. Jonathan Keeling pointed out that the local-density approximation (LDA) should be valid in the case

of this slowly-varying trap potential, so that the bright and dark density at any point should always be determined by an effective chemical potential, (μ - V(r)). The population of these states may, of course, be non-monotonic with this parameter; our situation would require that the bright population begin to fall at some point with increasing effective chemical potential. If the bright and dark states have fixed radiative rates, not varying over the trap (e.g. due to a spatially-varying bright/dark mixing), this treatment says that there is a fixed dependence of the intensity on the quantity (μ - V(r)). This allows comparison between experiments with varying total exciton number because as long as the effective chemical potential is the same between two points, at different density and different position, the brightness should be the same. Keeling showed explicitly from our data, with increasing pump power in the same trap, that the intensity fails to fall onto a single curve. One discrepancy between the LDA prediction and our data makes it easy to see why this is the case. Since, I(μ - V(r)) is a constant curve, the requirement of non-monotonic intensity dependence for increasing values of r at a single power means that at a single position, say at trap center, the intensity must be a non-monotonic function of power. The intensity at trap center should rise and then fall with increasing power. As demonstrated in Figure 22, the intensity at trap center does not decrease with increasing density, the rate of increase simply decreases. So, due to this clear argument, it is certain that there is not a dark condensate at trap center with a fixed recombination rate.

This does not rule out a condensate altogether, but it does require that there is at least an important role of single-particle physics in any condensate that we might predict, causing a variation in the condensate brightness as a function of position. While we have concluded this document with this fact, it was the main motivation for seeking a single-particle mechanism for a spatially-varying brightness, a search which concluded with the valence-band mixing argument presented above. While that argument also fails to explain the data on its own, it still allows a condensate with a brightness that varies spatially. One might naturally suggest that the next step would be to predict the brightness of a condensate using the calculated mixing fractions of Section 5.1.5, to determine whether a BEC of bright excitons with mixed valence-band character would produce this darkened center. After all, the coherence length measurement of Section 4.2.10 puts such a weak limit on the coherence

length that it still allows the possibility of a bright condensate with a coherence length of microns. The difficulty that one would run into is that the predicted LH fraction of the ground state was not large enough to cause a thermal population to show non-monotonicity, as shown in Figure 41. In that case, there was very little discrepancy between the density predicted by a Maxwell-Boltzmann occupation of the trap and the intensity profile that population would show. If the population were more tightly focused on the center of the trap due to BEC, this situation would only be exacerbated, as less of the population would be in the regions of significant LH fraction. So the BEC would be brightest at the center of the trap. This seems to again eliminate a purely bright condensate.

There is an alternative mechanism to produce a spatial variation that also violates the assumptions of the LDA analysis above. If the bright/dark splitting were allowed to vary across the trap, the character of the condensed population might also be varied. However, with no method to predict such a variation in the splitting, this possibility would be difficult to positively verify. On the other hand, the in-plane magnetic field experiments suggest that a dark condensate at trap center is unlikely. Those experiments showed that an in-plane magnetic field up to 1.4 T was not sufficient to cause a dramatic change in the brightness of the center of the trap. From this, we can be confident that there is not a large dark population protected from luminescing by a relatively weak symmetry. While this is a rather weak statement, it does rule seem to rule out a dark condensate at trap center, as the exchange splitting between the dark/bright IX states is unlikely to be large enough to survive even this small field.

Despite these difficulties with this explanation, two articles [36, 45] were recently published claiming that these experiments may be explained by the presence of a spinor condensate, composed of a mixture of bright and dark excitons. In these analysis, the bright/dark splitting is assumed to be negligible, which is certainly reasonable considering the small electron-hole overlap, and the condensate wavefunction is determined to be a bright/dark mixture due to spin-orbit coupling (of both Rashba and Dresselhaus type). Both of these analyses predict density profiles that are non-monotonic in the distance from the trap center. These can produce profiles that are dim in the center and bright on the sides, or even density profiles of the 'mexican hat' type (as described in [36]), depending on the param-

eters (interaction strength, spin-orbit coupling coefficients). In addition, there is a linear polarization associated with this mixing. In fact, many of the plots in [36] look strikingly like density profiles that we observe in our system, with only one important difference, the length scale. Overall, both of these analysis demonstrate phenomena that occur on the scale of a 1-2 μm, whereas the intensity patterning in our system occurs on a scale 100$\times$ larger. The condensate wavefunctions described in those works are unlikely to describe a system with a much larger length scale, particularly one with a coherence length much smaller than the size of the system.

Many types of BECs have been ruled out by our experiments, but we have not entirely eliminated the possibility of a BEC. For example, there may remain some additional aspect of the single-particle spectrum that we have overlooked, which provides a position-dependent decay rate. If that were the case, the case of a bright BEC with a non-monotonic intensity dependence could once again be examined. Of course, the first task upon uncovering such a single-particle mechanism for a spatially-varying decay rate would be to investigate whether it can cause the darkening pattern on its own, and, if not, whether a BEC could assist in this, as we have done here for the valence-band mixing due to strain. At this point, the exploration of the role of BEC in this intensity patterning awaits the demonstration of a novel mechanism for a spatially-varying decay rate or an explanation of how the small-scale dark/bright-mixed condensates mentioned above could apply to the current system.

5.4 CONCLUDING REMARKS

Along with refuting the considered mechanisms, we have uncovered several aspects of the darkening phenomenon that are instructive for future exploration, and we have clarified the effect of strain on the single-particle spectrum in this system. Some facts about the darkening are evident from our studies. First of all, there is *some* dark population present, where 'dark' now does not necessarily refer to the specific angular momentum state and merely means that the population is not accurately represented by the intensity profile. The monotonic decrease of the spectral linewidth, indicative of the scattering rate, moving away from the

center of the trap supports this assertion. The slowing of late-time decays also testifies to the presence of a slow decay rate at trap center in the highly-strained case. The question remains whether the slowness of the central decay is a feature of the single-particle spectrum or a many-body effect.

In addition, there is a good deal of indirect evidence that the darkening onset is strongly linked to the LH/HH splitting. The effect of strain to shrink this splitting is one piece of this, but the dependence of the transition on the well-width also suggests this link. In addition, the dark region is circular despite an elliptical IX trap. The IX trap shape is elliptical primarily due to the piezoelectric effect. So the dark region is determined by some consequence of the strain trap that is not affected by the piezoelectric effect, such as the splitting between IX states or, perhaps, even the DX trap.

This work began in the search for a Bose-Einstein condensate. While there is no clear indication that a condensate is present as the darkening occurs, there is also no indication that this effect spoils the system for future condensation studies. For example, the darkening does not mark the growth of a non-radiative decay channel – actually, the system begins to lose excitations more slowly. The extremely high stress system of LH IXs, which show much higher confinement, is the most likely case under which to expect this transition. While there are a number of experimental systems employed by others to seek a BEC of interwell excitons, strain-traps still offer some benefits over these. Recently, Butov et al. [23] have claimed condensation in an interwell system at 100 mK without a trap. The condensate occurs around defects in the CQW structure, so it is rather uncontrolled. A trapped system would certainly be preferable to this, where the parameters of the system could be systematically controlled. It may be the case that a temperature lower than that achievable with LHe-4 is required for BEC in this system, as there is certainly an upper limit on the transition temperature. For example, according to Zimmermann's dynamical T-matrix approach [86], the BEC transition at 6 K should occur beyond the Mott transition in this system. So, it may be the a BEC transition is impossible at this temperature. This can only be demonstrated by reaching these densities, a prospect that is unlikely in untrapped systems in quasi-equilibrium.

Since the densities for pursuing BEC in the LHe-4 temperature range may be in the range of the Mott transition, it is particularly troubling that the role of free carriers in this

system is quite poorly understand. It would be very helpful to implement a diagnostic tool to determine the presence of free charges, and, specifically, when the system has transitioned from a bound excitonic population to a system of free electrons and holes. Perhaps the most direct method for this characterization would be the addition of a microwave source to the system and measurement of the microwave absorption amplitude and resonant frequency. This has been implemented by Kukushkin, Rossokhaty, and Schmult [34] in an interwell system, showing the system capable of detecting the ionization transition by the variation of the resonant microwave frequency with concentration[15]. This characterization may even provide insight into the darkening behavior, if there is indeed ionization involved.

[15]Specifically, they showed that, using two different sized mesas, the ionized resonance frequency was size dependent, while the excitonic resonance (1S-2S exciton transition) was not. In addition, the plasma resonance shifts linearly with concentration, which would probably be the more detectable aspect in our system. The transition occurs at 5×10^9 cm^{-2} in that system. This low density can be understood in light of the very wide well-separation in their structure, leading to a very small binding energy and a large IX Bohr radius.

BIBLIOGRAPHY

[1] Proceedings of the Thirteenth Physics Summer School: Bose-Einstein Condensation: Atomic Physics to Quantum Fluids. Singapore, 2000. World Scientific.

[2] S. Adachi, T. Miyashita, S. Takeyama, Y. Takagi, a. Tackeuchi, and M. Nakayama. Polarization choices in exciton-biexciton system of GaAs quantum wells. *Physical Review B*, 55(3):1654–1660, January 1997.

[3] A. Alexandrou, J. Kash, E. Mendez, M Zachau, J. Hong, T. Fukuzawa, and Y. Hase. Electric-field effects on exciton lifetimes in symmetric coupled GaAs/Al0.3Ga0.7As double quantum wells. *Physical Review B*, 42(14):9225–9228, November 1990.

[4] M H Anderson, J R Ensher, M R Matthews, C E Wieman, and E a Cornell. Observation of bose-einstein condensation in a dilute atomic vapor. *Science (New York, N.Y.)*, 269(5221):198–201, July 1995.

[5] Lucio Andreani, Alfredo Pasquarello, and Franco Bassani. Hole subbands in strained GaAs-Ga_{1-x}Al_{x}As quantum wells: Exact solution of the effective-mass equation. *Physical Review B*, 36(11):5887–5894, October 1987.

[6] Lucio Claudio Andreani and Alfredo Pasquarello. Accurate theory of excitons in GaAs-Ga(1-x)Al(x)As wells. *Physical Review B*, 42(14):8928–8938, 1990.

[7] .arc, J. Tempel, F. Veit, M. Bayer, A. Rahimi-Iman, A. Löffler, S. Höfling, S. Reitzenstein, L. Worschech, and A. Forchel. From polariton condensates to highly photonic quantum degenerate states of bosonic matter. *Proceedings of the National Academy of Sciences of the United States of America*, 108(5):1804–9, February 2011.

[8] V. S. Babichenko and I. Ya. Polishchuk. Coulomb correlations and electron-hole liquid in double quantum wells. *JETP Letters*, 97(11):628–633, August 2013.

[9] R Balili, V Hartwell, D Snoke, L Pfeiffer, and K West. Bose-Einstein condensation of microcavity polaritons in a trap. *Science (New York, N.Y.)*, 316(5827):1007–10, May 2007.

[10] R. Balili, B. Nelsen, D. W. Snoke, R. H. Reid, L. Pfeiffer, and K. West. Huge splitting of polariton states in microcavities under stress. *Physical Review B*, 81(12):125311, March 2010.

[11] M Bayer, V B Timofeev, F Faller, T Gutbrod, and A Forchel. Direct and indirect excitons in coupled GaAs/Al_{0.30}Ga_{0.70}As double quantum wells separated by AlAs barriers. 54(12):8799–8808, 1996.

[12] L. Butov, A. Mintsev, Yu. Lozovik, K. Campman, and A. Gossard. From spatially indirect excitons to momentum-space indirect excitons by an in-plane magnetic field. *Physical Review B*, 62(3):1548–1551, July 2000.

[13] S Charbonneau, T Steiner, and MLW Thewalt. Optical investigation of biexcitons and bound excitons in GaAs quantum wells. *Physical Review B*, 38(5):5–8, 1988.

[14] YJ Chen, ES Koteles, BS Elman, and CA Armiento. Effect of electric fields on excitons in a coupled double-quantum-well structure. *Physical Review B*, 36(8):4562–4565, 1987.

[15] Shun Lien Chuang. *Physics of Photonic Devices*. Wiley, 2012.

[16] M. Combescot and D. Snoke. Stability of a Bose-Einstein condensate revisited for composite bosons. *Physical Review B*, 78(14):144303, October 2008.

[17] Monique Combescot, Odile Betbeder-Matibet, and Roland Combescot. Bose-Einstein Condensation in Semiconductors: The Key Role of Dark Excitons. *Physical Review Letters*, 99(17):176403, October 2007.

[18] Monique Combescot and Michael N Leuenberger. General argument supporting BoseEinstein condensate of dark excitons in single and double quantum wells. *Solid State Communications*, 149(13-14):567–571, 2009.

[19] S. Denev, V. Negoita, D. Snoke, B. Laikhtman, K. Eberl, and L. Pfeiffer. Optical detection of magnetic fields using giant magnetoresistance in undoped coupled quantum wells. *Physical Review B*, 66(20):205304, November 2002.

[20] Alberto Franceschetti and Alex Zunger. Quantum-confinement-induced Gamma -X transitions in GaAs/AlGaAs quantum films, wires, and dots. 52(20):664–670, 1995.

[21] Christopher Gies, Brandon van Zyl, S. Morgan, and D. Hutchinson. Finite-temperature theory of the trapped two-dimensional Bose gas. *Physical Review A*, (2):023616, February 2004.

[22] A. Griffin, D.W. Snoke, and S. Stringari, editors. *Bose-Einstein Condensation*. Cambridge University Press, Cambridge.

[23] A A High, J R Leonard, A T Hammack, M M Fogler, L V Butov, A V Kavokin, K L Campman, and A C Gossard. Spontaneous coherence in a cold exciton gas. *Nature*, 483(7391):584–8, March 2012.

[24] PC Hohenberg. Existence of long-range order in one and two dimensions. *Physical Review*, 158(2), 1967.

[25] I Carusotto Imamolu, T Volz, and A. Feshbach blockade: Single-photon nonlinear optics using resonantly enhanced cavity polariton scattering from biexciton states. *EPL (Europhysics Letters)*, 90(3):37001, 2010.

[26] AL Ivanov, PB Littlewood, and H Haug. Bose-Einstein statistics in thermalization and photoluminescence of quantum-well excitons. *Physical Review B*, 59(7):5032–5048, 1999.

[27] J Kasprzak, M Richard, S Kundermann, a Baas, P Jeambrun, J M J Keeling, F M Marchetti, M H Szymaska, R André, J L Staehli, V Savona, P B Littlewood, B Deveaud, and Le Si Dang. Bose-Einstein condensation of exciton polaritons. *Nature*, 443(7110):409–14, September 2006.

[28] LV Keldysh. The electron-hole liquid in semiconductors. *Contemporary Physics*, 1986.

[29] Jan Klaers, Julian Schmitt, Frank Vewinger, and Martin Weitz. Bose-Einstein condensation of photons in an optical microcavity. *Nature*, 468(7323):545–548, November 2010.

[30] DA Kleinman. Binding energy of biexcitons and bound excitons in quantum wells. *Physical Review B*, 28(2), 1983.

[31] C Klingshirn and H Haug. Optical properties of highly excited direct gap semiconductors. *Physics Reports*, 5(5), 1981.

[32] B. Koopmans, P.V. Santos, and M. Cardona. Microscopic Reflection Difference Spectroscopy on Semiconductor Nanostructures. *Physica Status Solidi (a)*, 170(2):307–315, December 1998.

[33] O Krebs and P Voisin. Giant Optical Anisotropy of Semiconductor Heterostructures with No Common Atom and the Quantum-Confined Pockels Effect. *Physical review letters*, 77(9):1829–1832, August 1996.

[34] I V Kukushkin, a V Rossokhaty, S Schmult, and K von Klitzing. Binding energy of indirect excitons in asymmetric double quantum wells. *Semiconductor Science and Technology*, 26(1):014023, January 2011.

[35] SH Kwok, HT Grahn, K Ploog, and R Merlin. Giant electropleochroism in GaAs-(Al, Ga) As heterostructures: the quantum-well pockels effect. *Physical review letters*, 69(6):973–976, 1992.

[36] O. Kyriienko, E. B. Magnusson, and I. a. Shelykh. Spin dynamics of cold exciton condensates. *Physical Review B*, 86(11):115324, September 2012.

[37] K G Lagoudakis, T Ostatnický, a V Kavokin, Y G Rubo, R André, and B Deveaud-Plédran. Observation of half-quantum vortices in an exciton-polariton condensate. *Science (New York, N.Y.)*, 326(5955):974–6, November 2009.

[38] B. Laikhtman and R. Rapaport. Exciton correlations in coupled quantum wells and their luminescence blue shift. *Physical Review B*, 80(19):195313, November 2009.

[39] R. Lee, N. Drummond, and R. Needs. Exciton-exciton interaction and biexciton formation in bilayer systems. *Physical Review B*, 79(12):125308, March 2009.

[40] G Li, D Jiang, H Han, Z Wang, and K Ploog. Type-Itype-II transition of GaAs/AlAs short-period superlattices investigated by photoluminescence spectroscopy under hydrostatic pressure. *Physical Review B*, 1989.

[41] YE Lozovik and OL Berman. Phase transitions in a system of spatially separated electrons and holes. *Journal of Experimental and Theoretical Physics*, (December 1996):1027–1035, 1997.

[42] Otfried Madelung, editor. *Semiconductors. Group IV Elements and III-V Compounds*. Springer-Verlag, 1991.

[43] Rita Magri and Alex Zunger. Anticrossing and coupling of light-hole and heavy-hole states in (001) GaAs/Al(x)Ga(1-x)As heterostructures. *Physical Review B*, 62(15):364–372, 2000.

[44] MZ Maialle, EAA e Silva, and LJ Sham. Exciton spin dynamics in quantum wells. *Physical Review B*, 47(23):776–788, 1993.

[45] M. Matuszewski, T. C. H. Liew, Y. G. Rubo, and a. V. Kavokin. Spin-orbit coupling and the topology of gases of spin-degenerate cold excitons in photoexcited GaAs-AlGaAs quantum wells. *Physical Review B*, 86(11):115321, September 2012.

[46] J. Menendez and a. Pinczuk. Light scattering determinations of band offsets in semiconductor heterostructures. *IEEE Journal of Quantum Electronics*, 24(8):1698–1711, August 1988.

[47] S. A. Moskalenko and D.W. Snoke. *BoseEinstein Condensation of Excitons and Biexcitons and Coherent Nonlinear Optics with Excitons*. Cambridge University Press, Cambridge, 2000.

[48] L. Mouchliadis and A. Ivanov. First-order spatial coherence of excitons in planar nanostructures: A k-filtering effect. *Physical Review B*, 78(3):033306, July 2008.

[49] Leonidas Mouchliadis and Alexei L Ivanov. First-order spatial coherence of indirect excitons in coupled quantum wells. *physica status solidi (c)*, 6(2):524–527, 2009.

[50] BN Murdin, W Heiss, C Langerak, and SC Lee. Direct observation of the LO phonon bottleneck in wide GaAs/Al_ {x} Ga_ {1-x} As quantum wells. *Physical Review B*, 55(8):5171–5176, 1997.

[51] V. Negoita, D.W. Snoke, and K. Eberl. Strong red shift of indirect exciton luminescence in low magnetic field. *Solid State Communications*, 113(8):437–441, January 2000.

[52] Viorel Negoita. Potential traps for excitons in two- and three-dimensional systems. *Dissertation, Univ. of Pittsburgh*, 2001.

[53] P. Nozieres. Some Comments on Bose-Einstein Condensation. In A. Griffin, D.W. Snoke, and S. Stringari, editors, *Bose-Einstein Condensation*, chapter 2. Cambridge University Press, Cambridge, 1996.

[54] Jl Osborne, Aj Shields, M Pepper, Fm Bolton, and Da Ritchie. Photoluminescence due to positively charged excitons in undoped GaAs/AlxGa1-xAs quantum wells. *Physical review. B, Condensed matter*, 53(19):13002–13010, May 1996.

[55] V. Palankovski. *Simulation of Heterojunction Bipolar Transistors*. PhD thesis, Institut für Mikroelektronik, 2000.

[56] R.K. Pathria. *Statistical Mechanics*. Butterworth-Heinemann, Oxford, 2nd edition, 1996.

[57] DS Petrov, M Holzmann, and GV Shlyapnikov. Bose-Einstein condensation in quasi-2D trapped gases. *Physical review letters*, (March), 2000.

[58] RT Phillips, GC Nixon, and T Fujita. Excitonic trions in undoped GaAs quantum wells. *Solid State Communications*, pages 287–291, 1996.

[59] G Bastard R. Ferreira. Assisted Hole Tunneling in Double Quantum Well Structures. *Surface Science*, 229:165–168, 1990.

[60] H W Liu R. Ferreira C. Delalande, G. Bastard, J.F. Palmier, B. Etienne. Electron, Hole, and Exciton Tunnelling in a Biased Quantum well structure. *Surface Science*, 229:192–194, 1990.

[61] A Ramanthan and P Cladé. Observation of a 2D Bose-gas: from thermal to quasi-condensate to superfluid. *APS Division of ...*, 6:1–5, 2008.

[62] B. K. Ridley. The in-plane effective mass in strained-layer quantum wells. *Journal of Applied Physics*, 68(9):4667, 1990.

[63] H. Sakaki, T. Noda, K. Hirakawa, M. Tanaka, and T. Matsusue. Interface roughness scattering in GaAs/AlAs quantum wells. *Applied Physics Letters*, 51(23):1934, 1987.

[64] G. Samara. Temperature and pressure dependences of the dielectric constants of semiconductors. *Physical Review B*, 27(6):3494–3505, March 1983.

[65] D Sanvitto, F Pulizzi, a J Shields, P C Christianen, S N Holmes, M Y Simmons, D a Ritchie, J C Maan, and M Pepper. Observation of charge transport by negatively charged excitons. *Science (New York, N.Y.)*, 294(5543):837–9, October 2001.

[66] Christoph Schindler and Roland Zimmermann. Analysis of the exciton-exciton interaction in semiconductor quantum wells. *Physical Review B*, 78(4):045313, July 2008.

[67] LG Shantharama and AR Adams. The kp interaction in InP and GaAs from the band-gap dependence of the effective mass. *Journal of Physics C: ...*, 4429, 1984.

[68] AH Simon, FM Steranka, and JP Wolfe. Electron-hole liquid in germanium under high¡ 111¿ stress. *Physical Review B*, 40(6), 1989.

[69] N. W. Sinclair, J. K. Wuenschell, Z. Vörös, B. Nelsen, D. W. Snoke, M. H. Szymanska, a. Chin, J. Keeling, L. N. Pfeiffer, and K. W. West. Strain-induced darkening of trapped excitons in coupled quantum wells at low temperature. *Physical Review B*, 83(24):245304, June 2011.

[70] David W. Snoke. *Solid State Physics: Essential Physics*. Addison-Wesley, San Francisco, 1st edition, 2008.

[71] DW Snoke and JD Crawford. Hysteresis in the Mott transition between plasma and insulating gas. *Physical Review E*, 1995.

[72] P. Sokol. BEC in Liquid Helium. In A. Griffin, D.W. Snoke, and S. Stringari, editors, *Bose-Einstein Condensation1*, chapter 4. Cambridge University Press, Cambridge, 1996.

[73] Vivek Srinivas, YJ Chen, and CEC Wood. Spin relaxation of two-dimensional electrons in GaAs quantum wells. *Physical Review B*, 47(16):907–910, 1993.

[74] Frank Stern. Transverse Hall effect in the electric quantum limit. *Physical Review Letters*, 21(December):1687–1690, 1968.

[75] Michael Stern, Vladimir Umansky, and Israel Bar-Joseph. Exciton liquid in coupled quantum wells. *Science (New York, N.Y.)*, 343(6166):55–7, January 2014.

[76] L. Pitaevskii Stringari and S. *Bose-Einstein Condensation*. Oxford University Press, Oxford, 2003.

[77] S. Utsunomiya, L. Tian, G. Roumpos, C. W. Lai, N. Kumada, T. Fujisawa, M. Kuwata-Gonokami, a. Löffler, S. Höfling, a. Forchel, and Y. Yamamoto. Observation of Bogoliubov excitations in exciton-polariton condensates. *Nature Physics*, 4(9):700–705, August 2008.

[78] Z. Voros. Dissertation: Interaction of Excitons in Two-Dimensional Potentials. *U. Pitt Dissertation*, 2008.

[79] Z Vörös, V Hartwell, D W Snoke, L Pfeiffer, and K West. Considerations on equilibration of two-dimensional excitons in coupled quantum well structures. *Journal of physics. Condensed matter : an Institute of Physics journal*, 19(29):295216, July 2007.

[80] Z. Vörös, D. Snoke, L. Pfeiffer, and K. West. Direct Measurement of Exciton-Exciton Interaction Energy. *Physical Review Letters*, 103(1):016403, July 2009.

[81] Z. Vörös, D. W. Snoke, L. Pfeiffer, and K. West. Equilibration of two-dimensional excitons in an in-plane harmonic potential. *Physica Status Solidi (C)*, 3(7):2461–2464, August 2006.

[82] C.T. Foxon V.V. Krivolapchuk, D.A. Mazurenko, E.S. Moskalenko, N.K. Poletaev, A.L Zhmodikov, T.S. Cheng. Anomalous influence of magnetic field on the indirect exciton in GaAs/AlGaAs double quantum wells. *Physics of the Solid State*, 40(5):737, 1998.

[83] Roland Winkler. *Spin–Orbit Coupling Effects in Two-Dimensional Electron and Hole Systems*, volume 191 of *Springer Tracts in Modern Physics*. Springer Berlin Heidelberg, Berlin, Heidelberg, 2003.

[84] K. Xu, Y. Liu, D. Miller, J. Chin, W. Setiawan, and W. Ketterle. Observation of Strong Quantum Depletion in a Gaseous Bose-Einstein Condensate. *Physical Review Letters*, 96(18):180405, May 2006.

[85] H. Zhu, K. Lai, D.C. Tsui, S.P. Bayrakci, N.P. Ong, M. Manfra, L. Pfeiffer, and K. West. Density and well width dependences of the effective mass of two-dimensional holes in (100) GaAs quantum wells measured using cyclotron resonance at microwave frequencies. *Solid State Communications*, 141(9):510–513, March 2007.

[86] R. Zimmermann. Dynamical T-matrix theory for high-density excitons in coupled quantum wells. *Physica Status Solidi (B)*, 243(10):2358–2362, August 2006.

[87] Roland Zimmermann and Christoph Schindler. Exciton-exciton interaction in coupled quantum wells. *Solid State Communications*, 144(9):395–398, December 2007.